UNIVERSITY OF CALIFORNIA

Santa Barbara

# Terahertz photonic crystals

A Dissertation submitted in partial satisfaction of

the requirements for the degree of Doctor of Philosophy

in Physics

by

Nathan Thomas Jukam

Committee in charge:

Professor Mark S. Sherwin, Chair

Professor S. James Allen

Professor Leon Balents

June 2006

UMI Number: 3218870





ProQuest Information and Learning Company
300 North Zeeb Road
P.O. Box 1346
Ann Arbor, MI 48106-1346

The dissertation of Nathan Thomas Jukam is approved

_____

Professor S. James Allen

_____

Professor Leon Balents

_____

Professor Mark S. Sherwin, Chair

June 2006

Terahertz photonic crystals

# ACKNOWLEDGEMENTS

I would first like to thank my advisor Mark Sherwin for his encouragement, never ending support, and insights. Without him this thesis would not be possible. I would like to thank Ilya Fushman and Jelena Vučković for FDTD photonic crystal calculations and help in the interpretation of data. Without them it would not have been possible to explain the experimental results in Chapter 8. I would also like to thank Cristo Yee, who as collaborated with me on THz photonic crystals for the last year. The future of THz photonic crystals at UCSB is in good hands. I want to thank my committee members Jim Allen, Leon Balents, and Mark Sherwin for approving my thesis.

I want to thank all the prior and present members of the Sherwin group: Dan Allen, Bryan Cole, Sam Carter, Carey Cates, Victoria Ciulin/Birkedal, Yuvaraj Dara, Matt Dotty, Kohl Gill, Sangwoo Kim, Tom King, James Lee, Chris Morris, Nick Moskovic, Brendan Serapaglia, Mark Su, Tristan Rocheleau, Larry Wang, Jon Williams, and Cristo Yee. I also want to thank Jim Allen and his current and former group members Greg Dyer, Shigeki Kobayashi, Xomalin Peralta, Naser Qureshi, Jeff Scott, Edzar Ulrich, Jing Xu, and Koichi Yammaguchi. I would like to acknowledge the interaction of visitors from other universities: Mathew Halsell, James Heyman, Martin Koch, and Hartmut Roskos.

I want to thank the cleanroom staff (Jack Whaley, Brian Thibeault, Bob Hill, etc) and the machine shop staff (Mike Wrocklage, Jeff Evans, etc) for their support.

David Wood deserves thanks for maintaining the mask writer. I want to thank Dave Enyeart and Jerry Ramian for running and maintaining UCSB's FEL lab.

Lastly, I would like to thank my parents and family members for putting me in a position to be able to receive this degree.

Vita of Nathan Thomas Jukam

June 2006

EDUCATION

Bachelors of Science in Physics, Trinity University, San Antonio, TX, May 1998.
Doctor of Philosophy in Physics, University of California, Santa Barbara, June 2006 (expected)

PROFESSIONAL EMPLOYMENT

Summer 1998: Summer Internship, Materials Science Division, Argonne National Laboratory
Winter-Spring 1999: Teaching Assistant, Department of Physics, University of California, Santa Barbara
1999-2006: Graduate Student Researcher, Department of Physics, University of California, Santa Barbara

PUBLICATIONS

Nathan Jukam, Ilya Fushman, Cristo Yee, Jelena Vučković, and Mark S. Sherwin "Patterned femtosecond laser excitation of terahertz leaky modes in GaAs Photonic Crystals." (to be submitted to Applied Physics Letters)

Nathan Jukam, and Mark S. Sherwin "Two-dimensional terahertz photonic crystals fabricated by deep reactive ion etching in Si." Applied Physics Letters, vol.83, no.1, 7 July 2003, pp.21-3.

PRESENTATIONS

"Patterned Femtosecond Laser Excitation of Terahertz Radiation in GaAs Photonic Crystals," presented at the Annual Conference on Lasers and Electro-Optics (CLEO) May 2006

"THz GaAs photonic crystals," presented a the Annual American Physical Society (APS) March Meeting 2005

"2-D THz photonic crystals fabricated by Deep Reactive Ion Etching in Si," presented at the Annual American Physical Society (APS) March Meeting 2003

"Silicon Whispering Gallery Resonators for Terahertz Frequencies," presented at the Annual American Physical Society (APS) March Meeting 2001

FIELDS OF STUDY

Major Field: Experimental physics

Studies in photonic crystals

Studies in terahertz time-domain spectroscopy

Studies in ultrafast femtosecond optics

ABSTRACT

Terahertz photonic crystals

by

Nathan Thomas Jukam

Terahertz (THz) photonic crystals are fabricated from high resistivity Si using deep reactive ion etching. THz radiation is coupled into the edge of the photonic crystals. Fourier Transform spectroscopy is used to measure the transmission spectra of the photonic crystals. For TE polarizations bandgaps are observed in the spectra which are consistent with two-dimensional calculations of the band diagrams.

THz GaAs photonic crystal slabs are fabricated using inductively couple plasma (ICP) reactive ion etching. A femtosecond laser beam generates THz radiation inside the photonic crystals. Spatial patterning of the laser beam is used to directly couple into the photonic crystal modes. Emitted THz radiation diffracted out of the slab is measured in the time domain using free space electro-optic sampling. Only the dipole modes are found to radiate strongly in the forward direction which is consistent with finite-difference time domain (FDTD) based calculations of the far-fields.

TABLE OF CONTENTS

# 1 Introduction

There is a technology gap in the electromagnetic spectrum for THz frequencies extending from .3-10 THz (wavelengths of 1000$\mu$m -30$\mu$m). Generating and detecting THz electromagnetic radiation at THz frequencies is much more difficult than generating and detecting other portions of the electromagnetic spectrum.

The THz frequency range divides the 'electronic' and 'photonic' portions of the electromagnetic spectrum. Here, the term 'photonic' is used to denote the mid infrared, near infrared and optical spectral regions. The term 'electronic' is used to denote denotes the portion of the electromagnetic spectrum that with a wavelength below 1mm, and includes millimeter waves, microwaves, radio waves, and audio frequencies. The THz frequency range is a transition region between electronics and photonics.

Many physical transitions occur in the THz frequency range. A photon with a frequency of 5 THz has the same energy as the value the thermal parameter kT at room temperature. Above the THz frequency range, the wavelength of light will be smaller than most macroscopic objects. Below the THz frequency range the, wavelength of electromagnetic radiation will generally be larger then macroscopic objects. For metals and semiconductors the scattering rate is near THz frequencies. This causes restive elements to have an imaginary component in their conductivity

comparable the real part of their conductivity. Because of these transitions at THz frequencies, the methods by which electromagnetic energy are handled above and below the THz frequency range is quite different.

## *Lasers and quantum detectors at 'photonic' frequencies*

Photonic frequencies can be generated and detected using semiconductor lasers and photodetectors whose principle of operation is based on quantum transitions. Optical photon energies are much greater then the room temperature value of kT (~25meV). At thermal equilibrium a particle in a quantum state a transition at "photonic" frequencies will be in the ground and state and have a negligible probability of being in the excited state.

The absence of an excited state population allows quantum detectors to operate at optical frequencies. Absorbed photons promote particles from the ground to the excited state. The number of particles in the excited state is proportional to the number of photons. (One example of quantum detector is the photodiode. The conduction (valence) band is the excited (ground state). )

At optical frequencies solid state lasers are efficient sources of coherent light. The interaction of the emitters in a solid state laser with the rest of the atoms in the crystal, introduces fast thermal relaxation via phonons. At room the thermal parameter kT lies in the THz range. However 'optical' frequencies have photon energies above kT. They will interact less with thermal radiation. At lower frequencies laser becomes more difficult. At THz frequencies excited state relaxation

is more likely to take place from the emission of a phonon while at optical frequencies excited state radiation is more likely to take place from the emission of a photon. It should be mention that lasing from the rotational levels of gas molecules at THz frequencies is routine. However THz gas lasers are big and inefficient and require a $CO_2$ gas laser for population inversion.

## *Diffraction*

The dimensions of macroscopic objects are much greater then 'photonic' wavelengths. Diffraction can often be neglected and light can be envisioned as rays in the geometrical limit. At photonic frequencies diffraction is only a higher order correction to geometrical objects except when light is brought to a focus, or emerges from a spot comparable to its' wavelength.

## *Electronic generation and detection of radiation*

For electronic frequencies the physical dimensions of electronic circuits are smaller the wavelength of light. Electromagnetic radiation must be coupled into and out of free space with antennas. Lasing and quantum detection become difficult at these frequencies since they energy levels are below kT even for cryogenic temperatures.

Efficient generation of coherent electromagnetic radiation can be achieved using an electronic circuit with gain and feeding the output into a resonator, and then back into the circuit. At electronic frequencies the wavelength of light is greater then the circuit's dimensions. This prevents electromagnetic radiation radiating efficiently

from circuits. To couple electronic electromagnetic radiation into free space antennas must be used which are structures that are greater or of the order of the wavelength of light. Free space radiation is coupled into an antenna and into an electronic circuit.

As electronic frequencies approach THz frequencies, resistive losses become excessive and transistors do not work. Electrons do not respond to applied AC voltages instantaneously - charging effects (RC times) slow down electrical signals. This causes a phase lag between currents and voltages that leads to loss, and becomes prohibitive at THz frequencies.

## *THz Technology*

Historically thermal detectors and emitters (with the exception of $CO_2$ pumped gas lasers) have been used in the THz frequency region. Golay cells, pyroelectric detectors, and bolometers all work on the principle that absorbed heat from incident radiation changes the temperature of the detector. The change in temperature can then be measured electronically.

Broadband incoherent THz radiation can be produced from blackbody sources. Thermal radiation from a blackbody source can then be used to perform spectroscopy on samples using Fourier transform Spectroscopy (FTS) - sometimes referred to as Fourier transform Infrared Spectroscopy (FTIR).

Recently several developments have narrowed THz technology gap. Femtosecond lasers have been found to generate THz pulses when incident on semiconductors. The THz electro field of such pulses can be measured using a

femtosecond probe beam with a photoconductive antenna, or an electro-optic crystal. THz Superconducting electron bolometers have been made with low extremely low noise equivalent power. Solid state THz quantum cascade lasers have lased at THz frequency and have been used for THz imaging systems. Schottky diodes operating at THz frequencies have been produced to coherently detect THz radiation by down mixing with a local oscillator. Narrow band THz radiation can also be produced by frequency multiplying the microwaves into the THz wavelengths.

## *Photonic crystals*

A photonic crystal is a periodic variation in the index of refraction whose length scale is on the order of the wavelength of light. If the periodic variation of the index is large, light will be strongly scattered and distort the dispersion or bands (plots of $\omega$ versus $k$) of the medium. This may lead to the formation of bandgaps in the photonic band diagram, where no modes exist for frequencies in the bandgap.

Light with a frequency in a band gap is forbidden to propagate inside it. Incident light having a frequency in a bandgap will be reflected from the photonic crystal. A photonic crystal is a perfect mirror for frequencies in a band gap. By surrounding a region of space on all sides with a photonic crystal a cavity will be created with resonances in the band gap. A single defect in the photonic crystal can create a small photonic cavity with dimensions on the order a wavelength. While point defects will create cavities, line defects will create waveguides. Photonic crystal waveguides can

have sharp bends and thickness on the order of wavelength. Photonic crystals allow the control of light on the scale of its wavelength.

The periodic variation in the index of refraction can be created by etching air holes in a semiconductor using micro and nanofabrication technology. Fabrication technology concerns itself with creating planar array of transistors. It is more amenable to create two dimensional arrays of air holes, then three dimensional arrays. A two dimensional array of air holes is often etched into a thin slab. Light is confined in the 3rd vertical dimension by total internal reflection at the air slab interfaces. Often the slab is made thin on the order of half the wavelength to cut off higher order vertical modes.

By changing the period and size of the air holes the dispersion curves can be controlled. Changing the dimensions of a point defect will alter the mode profiles and resonances of cavities. Photonic crystals enable one to engineer the photonic properties of defect cavities, waveguides, and the materials themselves. In the future, photonic crystals will surely contribute to closing the THz technology gap.

In this thesis THz photonic crystals are studied. Photonic crystals allow one to engineer the optical properties of a material. The dispersion of a material can be controlled which can lead to the super prism effect and slow light propagation. Photonic crystal can be used to create filters and frequency selective mirrors. Cavities and waveguides which can have dimensions on the order of the wavelength can be produced from photonic crystals. The resonant and guided frequencies of these waveguides can be controlled engineering using a photonic crystal. In the

future THz photonic crystal will surely contribute to the closing of the THz technology gap.

## *Materials for photonic crystals*

There a three things to consider when selecting a material to make a photonic crystal out of. The material should have a high index of refraction, it should have negligible loss at the frequencies of interest, and the technology must exist to shape the material on a length scale smaller then the wavelength of interest. Photonic bandgaps increase as the index of refraction increases. A high index of refraction gives one more leeway in designing photonic crystals.

For a frequency of one THz the material that best satisfies these criteria is Si. It has one of the highest indices of refraction 3.42 at THz frequencies. High resistivity float zone Si has perhaps the lowest loss (<.02 $cm^{-1}$ at 1 THz) of any solid material at THz frequencies. Highly developed fabrication technology exists for creating Si micromachines and MEMs devices on micron length scales. This technology can be directly borrowed to create Si photonic crystals

GaAs is another possible material to make THz photonic crystals. It has a higher index of refraction 3.6 then Si. However it has greater loss (.5 $cm^{-1}$ at 1 THz) then Si. Less micro fabrication technology exists to shape GaAs then Si. GaAs is also more fragile then Si. A thin layer of GaAs is more prone to breaking then a thin layer of Si. Nevertheless, GaAs is an excellent material to make photonic crystals out of. It is probably the best semiconductor candidate for making THz photonic crystals besides

Si. GaAs also has the advantage that active THz devices can be made out of it. One can thus imagine inserting active THz devices into photonic crystals that would interact with the photonic crystal modes.

High density polyethylene (HDPE) is another material suitable for the manufacture of THz photonic crystals. It can be easily molded and has a low loss. It is also somewhat flexible. Photonic crystal fibers have been made out of HDPE[1]. However its' index of refraction is 1.52 at THz frequencies[2] which is less then other semiconductors.

## *THz optical properties of Si*

The major loss mechanism at THz frequencies in Si is absorption from free carriers. The free carriers in Si form a dilute plasma. The plasma's frequency response is determined by the parameter $\omega_p$ - referred to as the plasma frequency -

$$\omega_p = \sqrt{\frac{ne^2}{\varepsilon m^*}} \tag{1.1}$$

Here n is the carrier concentration, $\epsilon$ is the dielectric of the material, m* is the reduced mass of the electron, and e is the charge of an electron. For frequencies below $\omega_p$ the plasma will behave as a metal. For frequencies above $\omega_p$ the plasma cannot respond fast enough to the time varying electric field, and will behave as an insulator. For frequencies near $\omega_p$ the plasma will be highly absorbing.

The doping concentration in Si, along with the plasma frequency of Si can be varied over several orders of magnitude. Float zone n-type Si can have resitivities

that approach 20KΩ-cm. An n-type Si wafer with a resistivity of 500 Ω-cm will have carrier concentrations of ~$10^{13}$ $cm^{-3}$.[3] At this level of doping the plasma frequency is less then 5 GHz and THz frequencies will not be absorbed. The absorption coefficient of high resistivity float zone Si has been measured to be less then .025 $cm^{-1}$ from .5 to 2 THz[4]. The Kramers-Kronig relations imply that a material with low absorption has a flat dispersion, and vice-versa. Si has an extremely flat dispersion at THz frequencies. The index is between 3.41745 and 3.41755 from .5 to 3.5 THz[4].

The absorption of THz frequencies in Si increases with increasing frequency. This implies absorption in high resistivity Si is probably caused by multi-phonon processes and residual absorption from the optical phonon line - near 18 THz. If the dominant absorption was caused by free carriers, the absorption would decrease with increasing frequency.

## *THz optical properties of GaAs*

In contrast to Si, GaAs can be compensated when grown. Semi insulating wafers with resitivities greater then $10^7$ Ω-cm can be produced. For semi insulating GaAs wafers absorption from free carrier wafers can be completely neglected. However, as for Si, if GaAs is heavily doped the material will be strongly absorbing.

Like Si, GaAs has a high index of refraction at THz frequencies. At 1 THz the index of GaAs is 3.60, and the absorption coefficient is approximately .5 $cm^{-1}$.[5] As with Si, THz absorption in GaAs is caused by phonons. The absorption of THz frequencies in GaAs is higher then absorption in Si, since the optical phonon line of

GaAs lies between 8 and 9 THz while the optical phonon line in Si is at 18 THz. The absorption in GaAs strongly increases with frequency as the optical phonon line is approached.

THz absorption in GaAs decreases with falling temperature as the phonon population decreases[6]. The absorption coefficient of GaAs at 1.5 THz at a temperature of 60K is less then .05 $cm^{-1}$.[7] The residual THz absorption in Si is caused by phonon processes. If the temperature of Si is decreased, it should become more transparent as the phonon population is diminished.

## *Absorption limited quality factors*

Both absorption coefficients for Si and GaAs may appear small. A material with a loss of .5 $cm^{-1}$ will experience a power loss of 63% when it passes through 2 cm of material. An absorption coefficient .025 $cm^{-1}$ appears to be no better as THz will be highly attenuated after traversing a meter. To get an idea of a material's suitability for making photonic crystals, we can calculate the absorption limited quality factor of a resonator made from the material.

A resonator stores energy. The spectral width of the resonance depends on the rate of energy loss from the resonator, and the frequency of the resonance. The quality factor is a measure of a resonator's rate of energy loss. A resonator with resonance frequency $\omega$, and quality factor $Q$ will lose stored energy $U$, at the rate

$$\frac{dU}{dt} = -\frac{\omega}{Q}U \tag{1.2}$$

For a photonic crystal resonator, energy may be lost from radiation leakage, non-specular scattering from surface roughness, and absorption. The quality factor can be expressed in terms of the three separate loss mechanisms as

$$\frac{1}{Q_{total}} = \frac{1}{Q_{leakage}} + \frac{1}{Q_{roughness}} + \frac{1}{Q_{absorption}} \tag{1.3}$$

The quality factor of a given loss mechanism $Q_{\text{loss}}$ will always be less then the total quality factor $Q_{total}$. Each loss mechanism's quality defines an upper bound on the total quality factor.

For a photonic crystal resonator radiation leakage will occur that is caused by light rays above the critical angle which are not totally internally reflected. The radiation leakage can be minimized by the proper design of the photonic crystal[8].

$Q_{roughness}$ is the energy loss from light scattered out of the photonic crystal by surface roughness. If the length scale of the roughness is much less then the wavelength of light, there will be low scattering loss, and $Q_{roughness}$ will be high.

The value of $Q_{absorption}$ can be found from the absorption coefficient $\alpha$. The absorption coefficient determines the energy loss per unit length as light travels through a material.

$$\frac{dU}{dz} = -\alpha U(z) \tag{1.4}$$

By converting length to time in (1.4) ($t = nz/c$), and substituting the results into equation (1.2), $Q_{absorption}$ can be expressed in terms of the absorption coefficient as

$$Q_{absorptoin} = \frac{\omega n}{\alpha c} \tag{1.5}$$

If the absorption coefficient of Si is .01 $cm^{-1}$ at 1 THz, the upper bound on quality factor imposed by absorption is $7x10^4$. For GaAs with an absorption coefficient of .5$cm^{-1}$ at 1 THz, the maximum quality factor is 1500. These values are for room temperature. As the temperature is decreased, the phonon population will be reduced along with the absorption coefficient. At cryogenic temperatures, the bounds placed on the quality factors of GaAs and Si by absorption will be much higher then at room temperature.

## *Micromachining technology*

To make Si and GaAs photonic crystals features must be made in them whose size and spacing is on the order of the wavelength of light. In Si the wavelength of 1 THz is 88$\mu$m, and in GaAs the wavelength of 1 THz 83$\mu$m.

Cleanroom technology exists to etch air holes into both Si and GaAs on the order of 10's and 100's of microns. Masks for air hole etches can be patterned to resolutions less then a micron with photolithography. Advanced reactive ion etching (RIE) can produce air holes with vertical sidewalls. RIE etches with inductively coupled plasma produced a dense plasma with high etch rates on the order of microns per minute. The ratio of semiconductor to mask material etched (the selectivity) can be very high approaching 200:1 for Si:$SiO_2$. The combination of high selectivity and fast etch rates allow etches with depths over 10$\mu$m and even 100$\mu$m.

There is a great deal of interest in deep vertical etches of Si for MEMs devices. Consequently Si deep reactive ion etching is more advanced for Si then GaAs. Some interest exists for etching deep via holes in GaAs for use with microwave circuits. The etch rates of GaAs are of the same order as the etch rates of Si. However, the sidewalls of GaAs etches are in general rougher, and lack the anisotropy of Si etches.

To cut off higher order dielectric waveguide modes, the thickness of a photonic crystal slab is often required to be on the order of half a wavelength. GaAs and Si wafers are hundreds of microns thick whereas the wavelength of 1 THz in GaAs and Si is on the order of 80$\mu$m. To make photonic crystal slabs out of standard Si and GaAs wafers it necessary to thin the wafers to the required thickness.

Si wafers can also be obtained in more useful forms then GaAs wafers for the creation of thin photonic crystals. Since Si is not as fragile as GaAs, Si wafers as thin as 10$\mu$m can be purchased directly[9]. Si on insulators (SOI) wafers can also be purchased commercially. SOI wafer have a large epilayer of Si up to 10's of microns thick and a buried $SiO_2$ layer a few microns thick under the epilayer. The buried $SiO_2$ layer can serve as an etch stop. A thin layer of Si can be formed by etching through the back side of the wafer to the etch stop layer.

For GaAs wafers an AlGaAs layer can serve as an etch stop if the plasma contains fluorine ions. AlGaAs layers can be grown by molecular beam epitaxy MBE, or metallic organic vapor deposition MOCVD. However, growing an etch stop layer and then growing 20 $\mu$m or 40$\mu$m of GaAs on top of is very prohibitive in time and cost.

## *GaAs and Si as materials for THz photonic crystals*

Both Si and GaAs are excellent materials to make THz photonic crystals. They both have a high index of refraction, relatively low loss, and the technology exists to shape them on THz sub-wavelength length-scales. THz photonic crystal can be used to improve THz technology and help bridge the THz technology gap. THz photonic crystal resonators could be used to make THz resonators for lasers, THz waveguides, THz on chip photonic crystal circuits, THz filters, THz mirrors and many other THz photonic devices.

## *Outline of thesis*

In Chapter 2 a general overview of photonic crystals is given. This chapter is pedagogical. It is meant to give the reader a brief introduction to the subject and the information necessary to understand the motivation and results of other chapters. The first part of the Chapter 2 follows the book by on photonic crystals by Joannopoulos[10], and introduces photonic crystals by examining the wave equation viewed in term of a hermitian operator. The modes of a dielectric slab waveguide are examined as prelude to photonic crystal slabs discussed at the end of the Chapter 2.

The rest of the thesis can be divided into two parts one on Si THz photonic crystals and the other on of GaAs THz photonic crystals. Chapters 3 and 4 cover the work on Si THz photonic crystal while Chapters 5, 6, 7 and 8 cover the work on GaAs photonic crystals. There are more chapters on GaAs photonic crystals since the

measurement and fabrication techniques for GaAs photonic crystal were more involved then those for Si photonic crystals.

In the work on Si photonic crystals, two-dimensional Si photonic crystals were fabricated out of 500 $\mu$m thick Si wafers. THz radiation was coupled into and out of the edges of the wafers. The transmitted spectra were measured using Fourier transform spectroscopy. Chapter 3 describes Fourier transform spectroscopy also known as FTIR. Chapter 4 discusses the fabrication of Si photonic crystals and the transmission experiments performed on the Si photonic crystals.

In the work on GaAs photonic crystals, thin photonic crystal slabs were made out of GaAs wafers. THz radiation was generated inside the photonic crystals using femtosecond laser pulses. Chapter 6 describes the physical mechanisms and the methods of generating THz radiation in GaAs with a femtosecond laser. The emitted THz radiation from the GaAs photonic crystals was measured using free electro-optic sampling. Chapter 5 describes the electro-optic sampling setup used for these measurements. Chapter 7 begins by describing the motivations for making and GaAs THz photonic crystals and then explains how the GaAs photonic crystals were fabricated. Chapter 8 concludes the thesis with a discussion of the experimental results from THz GaAs photonic crystals.

Chapters 3, 5, and 6 are descriptions of the experimental methods and techniques used to characterize the photonic crystals. Chapters 4, 7, and 8 discuss the fabrication and measurement of the photonic crystal samples, and are the original research of this thesis.

# 2 Photonic crystals

An atomic or molecular crystal consists of a periodic arrangement of atoms on a lattice. In the free electron model the atom's outer electrons are envisaged to be ionized. The periodic lattice of positive ions produces a periodic electronic potential for the free electrons. The lattice spacing of atomic crystals is often on the same order as the Debroglie wavelength of the free electrons. Since the wavelength of the free electrons and the period of the lattice are on the same length scale, the electrons strongly in interact with the electronic potential of the positive ions. Diffraction occurs and energy gaps in the band diagrams of the free electrons can occur. To a great extant the physical properties of atomic crystals depends on the band structures. Questions such as; is the crystal an electrical conductor; what is the absorption spectrum; are determined by the band structure.

Analogous to an atomic crystal, a photonic crystal consists of a periodic arrangement of the index of refraction on a lattice. For photons the index of refraction is analogous to the electrostatic potential in atomic crystals. A material with a high index of refraction can alter the trajectory of photons and confine them. While a material with an index of refraction close to unity will have little effect on the trajectory of photons. If the periodic variation of the index of refraction is on the same order as the wavelength of light, diffraction can occur and photonic bandgaps

can form. The dispersion relation can be plotted as a photonic band diagram in the Brillouin zone. For a photonic band diagram frequency versus wave vector is plotted instead of energy versus wave vector.

In this chapter a brief introduction to photonic crystals is given. The first part of the chapter follows the treatment in Joannopoulos[10]. The wave equation is examined as a hermitian eigenvalue problem for magnetic fields. The modes of a dielectric waveguide slab are then discussed as background for photonic crystal slabs. At the end of the chapter, photonic crystal slab modes are discussed in the context of the light-line.

## *Maxwell's equations for harmonic modes*

For harmonic modes with an electric and magnetic field of the form $\mathbf{H}(\mathbf{r})e^{i\omega t}$ and $\mathbf{E}(\mathbf{r})e^{i\omega t}$, Maxwell's equations are

$$\nabla \bullet \varepsilon(r)\mathbf{E} = 0 \tag{2.1}$$

$$\nabla \bullet \mathbf{H} = 0 \tag{2.2}$$

$$\nabla \times \mathbf{E} = \mu_o i\omega \mathbf{H} \tag{2.3}$$

$$\frac{1}{\varepsilon(\mathbf{r})}(\nabla \times \mathbf{H}) = i\omega \mathbf{E} \tag{2.4}$$

where the medium has been assumed to be nonmagnetic with no free charges or currents. It is important to note that the permittivity ($\varepsilon = n^2$) is a function of position for a photonic crystal, and cannot be treated as a constant when manipulating

Maxwell's equations. Taking the curl of both sides of equation (2.4) and substituting equation (2.3) , one finds the wave equation for a medium with spatial variations in the index of refraction.

$$-\nabla\times\left(\frac{1}{n^2(\mathbf{r})}\right)\nabla\times\mathbf{H}=\left(\frac{\omega}{c}\right)^2\mathbf{H} \tag{2.5}$$

The wave equation is an eigenvalue problem with eigenvector $\mathbf{H}(\mathbf{r})$ and eigenvalue $(\omega/c)^2$. The "wave" operator $-\nabla\times\left(1/n^2(\mathbf{r})\right)\nabla$ is a hermitian operator. In equation (2.4) the electric field is determined directly from the magnetic field, frequency and permittivity.

The wave equation (equation (2.5)) is somewhat analogous to the time independent Schrödinger's equation. The solutions to the time dependent Schrödinger's equation are of the form $\psi(r,t)=\psi(r)e^{i\frac{E}{\hbar}t}$ where $\psi(r)$ is a solution to the time independent Schrödinger's equation. This is analogous to harmonic modes $\mathbf{H}(\mathbf{r})e^{i\omega t}$ of Maxwell's equation. Both equations are eigenvalue problems that have hermitian operators. But the analogy must not be carried too far. Schrödinger's equation is scalar equation while the wave equation (2.5) is a vector equation. The potential term $n^{-2}(\mathbf{r})$ cannot be separated from the curl operators in equation (2.5). In Schrödinger's equation the Hamiltonian is the sum of a Laplace operator and a potential operator. Electrons will interact with each other and a charge density term (proportional to the modulus of the wave function) must often be added to the

potential. Photons however will not interact with one and other except for very high intensities where the regime of linear optics fails.

## *Hermitian operators and inner products*

The inner product between two fields $\mathbf{A}$ and $\mathbf{B}$ is

$$\left\langle \mathbf{A}(\mathbf{r}) \middle| \mathbf{B}(\mathbf{r}) \right\rangle \equiv \int \mathbf{A}^{*}(\mathbf{r})\, \mathbf{B}(\mathbf{r})\, d\mathbf{r}^{3} \tag{2.6}$$

A hermitian operator $\mathcal{G}$ is defined such that

$$\left\langle \mathbf{A}(\mathbf{r}) \middle| \mathcal{G}\mathbf{B}(\mathbf{r}) \right\rangle = \left\langle \mathcal{G}\mathbf{A}(\mathbf{r}) \middle| \mathbf{B}(\mathbf{r}) \right\rangle \tag{2.7}$$

The "wave" operator $-\nabla \times \left(1/n^{2}(\mathbf{r})\right) \nabla$ of equation (2.5) can be shown to be hermitian by integrating by parts twice. The integral of (2.6) is taken over all of space. The surface terms of the integration by parts vanish since the fields are assumed to be zero at infinity.

In quantum mechanics many theorems and results are derived from the hermicity of the Hamiltonian. These theorems and results can now be applied to the magnetic field and its wave equation (2.5). They will not necessarily hold for the electric field. However, for a given result one can use equation (2.5) and replace the magnetic field with a term proportional to the curl of the electric field. This will produce a new equation for $\mathbf{E}(\mathbf{r})$ which can be further manipulated to determine if the theorem or results holds for $\mathbf{E}(\mathbf{r})$. Theorems can often by verified or proven false using these methods.

A wave equation for the electric field can be found in a similar manner as the wave equation for the magnetic field. One can take the curl of both sides of (2.3) and then substitute (2.4) to find

$$\left(\nabla\nabla\bullet\varepsilon(r)-\left(\frac{1}{n^2(\mathbf{r})}\right)\nabla^2\right)\mathbf{E}=-\left(\frac{\omega}{c}\right)^2\mathbf{E} \tag{2.8}$$

The electric and magnetic field wave equations (equation (2.8) and equation (2.5)) are redundant. They contain the same information, because for a given magnetic field (electric field) the corresponding electric field (magnetic field) is given by (2.4) ((2.3)). However the operator on the left hand side of (2.8) is not hermitian. It is best to work the magnetic field wave equation (2.4) instead of the electric field wave equation (2.8).

## *Bloch's theorem*

An example of one result that carries over from quantum mechanics to photon crystals is Bloch's Theorem for periodic potentials. It can be proved by using operator manipulation and relies on the result that a hermitian operator and an operator that commutes with it have simultaneous eigenvectors.

Let $T_{\mathbf{R}}$ be the translation operator for defined by $T_{\mathbf{R}}\mathbf{A}(\mathbf{r}) = \mathbf{A}(\mathbf{r}+\mathbf{R})$. An eigenvector of $T_{\mathbf{R}}$ has the eigenvalue $e^{i\mathbf{K}\bullet\mathbf{R}}$. Take $\mathbf{R}= m_1\mathbf{a}_1+m_2\mathbf{a}_2+m_3\mathbf{a}_3$ where the $m_i$ are integers and the $a_i$ are the basis vectors of the lattice. The potential is periodic over the lattice. Therefore the wave operator $-\nabla\times\left(\varepsilon_o/\varepsilon(\mathbf{r})\right)\nabla$ will be invariant when acted on by $T_{\mathbf{R}}$ and

$$\begin{aligned}&\mathbf{T_R}\left(-\nabla\times\left(\varepsilon_0/\varepsilon(\mathbf{r})\right)\nabla\,\mathbf{H}(\mathbf{r})\right)=\left(-\nabla\times\left(\varepsilon_0/\varepsilon(\mathbf{r}+\mathbf{R})\right)\nabla\,\mathbf{H}(\mathbf{r}+\mathbf{R})=\left(-\nabla\times\left(\varepsilon_0/\varepsilon(\mathbf{r})\right)\nabla\,\mathbf{H}(\mathbf{r}+\mathbf{R})\right)\right.\\&\left(-\nabla\times\left(\varepsilon_0/\varepsilon(\mathbf{r})\right)\mathbf{T_R}\,\mathbf{H}(\mathbf{r})=\left(-\nabla\times\left(\varepsilon_0/\varepsilon(\mathbf{r})\right)\nabla\,\mathbf{H}(\mathbf{r}+\mathbf{R})\right.\right.\end{aligned}\tag{2.9}$$

This implies the wave operator and translation operator commute with on and other. The wave operator and translation operator must then have simultaneous eigenvectors. If $\mathbf{H}(\mathbf{r})$ is an eigenvector of the wave equation then it is also an eigenvector of the translation operator $T_{\mathbf{R}}\mathbf{H}(\mathbf{r})$, and

$$\mathbf{T}_R\mathbf{H}(\mathbf{r})=\mathbf{H}(\mathbf{r}+\mathbf{R})=\ ^{+i\mathbf{k}\bullet\mathbf{R}}\mathbf{H}(\mathbf{r})\tag{2.10}$$

Equation (2.10) is a form of Bloch's theorem. It is often more convenient to write it in different form. If $\mathbf{u}(\mathbf{r})=e^{-i\mathbf{k}\bullet\mathbf{r}}\mathbf{H}(\mathbf{r})$, then Bloch's theorem can be use to show that $\mathbf{u}(\mathbf{r})$ is a periodic function in **R.** Examining the expression $\mathbf{u}(\mathbf{r}+\mathbf{R})=$ $e^{-i\mathbf{k}\bullet(\mathbf{r}+\mathbf{R})}\mathbf{H}(\mathbf{r}+\mathbf{R})=\ e^{-i\mathbf{k}\bullet\mathbf{r}}\left[e^{-i\mathbf{k}\bullet\mathbf{R}}\mathbf{H}(\mathbf{r}+\mathbf{R})\right]$, it is apparent from Bloch's theorem (2.9) that the term in the brackets is $\mathbf{H}(\mathbf{r})$. Bloch's theorem can then be written as

$$\mathbf{H}\left(\mathbf{r}\right)=e^{ik\,\bullet\,\mathbf{r}}\mathbf{u}\left(\mathbf{r}\right)\tag{2.11}$$

where $\mathbf{u}(\mathbf{r})$ is a periodic function with period **R.**

The electric field can also be shown to satisfy Bloch's theorem. This can be done by substituting (2.10) into (2.4) and obtaining

$$\mathbf{E}(\mathbf{r})=\frac{e^{i\mathbf{k}\bullet\mathbf{r}}}{i\omega n^2(\mathbf{r})}\left[\mathbf{k}\times\mathbf{u}(\mathbf{r})+\nabla\times\mathbf{u}(\mathbf{r})\right]\tag{2.12}$$

The expression in brackets in equation (2.12) is a periodic function of **R.** The electric is composed of a phase $e^{i\mathbf{k}\bullet\mathbf{r}}$ multiplied by a periodic function, and Bloch's theorem holds for the electric field.

## *Reduced zone scheme*

If the value of **k** is outside the Brillion zone then **k** may be rewritten as $\mathbf{k} = \mathbf{k}_{\text{reduced}} + \mathbf{G}$ where $\mathbf{k}_{\text{reduced}}$ is inside the Brillion zone and **G** is a reciprocal lattice vector. A Bloch function with a wave vector outside of the Brillion zone $e^{\mathbf{i}(\mathbf{k}_{reduced}+\mathbf{G})\bullet\mathbf{r}}\mathbf{u}(\mathbf{r})$ can be rewritten in term of a wave vector inside the Brillion zone as

$$\begin{aligned}\mathbf{H}(\mathbf{r},t) &= e^{i\mathbf{k}_{reduced}\bullet\mathbf{r}}\mathbf{u}'(\mathbf{r})\\ \mathbf{u}'(\mathbf{r}) &\equiv e^{\mathbf{iG}\bullet\mathbf{r}}\mathbf{u}(\mathbf{r})\end{aligned} \tag{2.13}$$

If we demand to that all the wave vectors for a given field should be in the Brillion zone then we are working in the reduced zone scheme. Fields with different periodic functions, but the same wave vector $\mathbf{k}_{\text{reduced}}$ will (except for degenerate modes) have different frequencies. For two fields with the same wave vector, the field at a higher frequency will have more nodes or 'ripples' in the periodic function **u**(**r**) then the field at the lower frequency.

## *Band diagrams*

A band diagram is a graph of the photonic crystal's dispersion relation in the reduced zone scheme. Frequency is plotted as a function of $\mathbf{k}_{\text{reduced}}$. The reduce zone scheme will fold the bands at the boundaries of the Brillion zone. Figure 2.1 shows a

band diagram for a two dimensional photonic crystal with a triangular lattice. The two basis vectors have the same length ($a$) and are separated by an angle of $\pi/3$ radians. Each unit cell of the lattice contains a circular air hole of radius r=.45$a$ in a surrounding dielectric background medium with an index of 3.6.

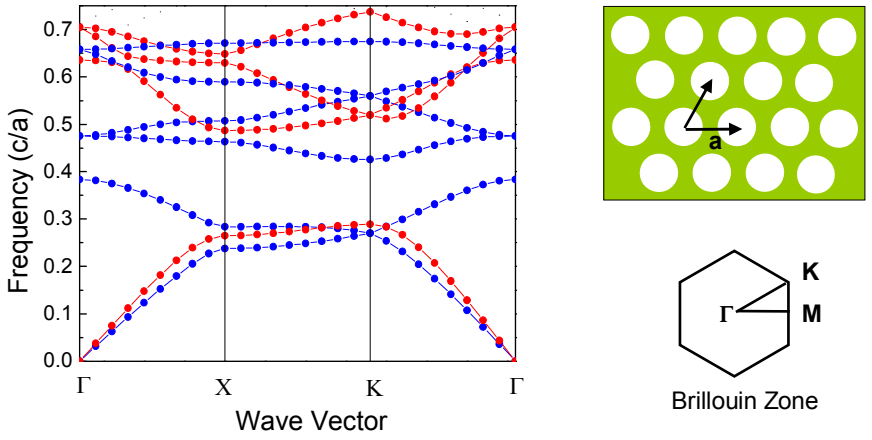


**Figure 2.1** Band diagram of a 2D photonic crystal. The air hole radius is .45$a$. Blue lines TM modes. Red lines TE modes.

## *TE and TM modes*

For a two-dimensional crystal, there are two sets of modes - transverse electric (TE) and transverse magnetic (TM). In Figure 2.1 the TM modes are blue while the TE modes are read. The TE modes have their electric field in the plane of the photonic crystal and their magnetic field perpendicular to the photonic crystal's plane. For the TM modes the magnetic field is in plane while the electric field is out of plane. The reason the modes split up into two distinct set is that a two-dimensional photonic crystal is symmetric under mirror reflection perpendicular to the plane. A field reflection operator $\Omega_l$ for mirror reflections about a plane $l$ can be defined as

$$\Omega\big(\mathbf{H}(\mathbf{r})\big) = \mathrm{M}_l\mathbf{H}(\mathrm{M}_l\mathbf{r}) \tag{2.14}$$

where $\mathrm{M}_l$ is the operator for reflections about the plane *l*. The field reflection operator reflects both the position of the points of a vector field and the direction of the corresponding vectors. (This becomes important for three-dimensions) When operated on by the field reflection operator odd modes have eigenvalue -1 or odd parity - and the even modes have even parity. This implies the vector reflection operator and the "photonic crystal" operator have simultaneous eigenmode. For two-dimensional photonic crystal the even and odd modes are strictly TM and TE modes. For three-dimensional photonic crystals (such as photonic crystal slabs) that have a symmetric structure about a plane *l,* the even and odd modes are not strictly TM and TE. But the even and odd modes are approximately TM and TE modes, and they are often referred to as TM and TE modes.

## *Frequency units*

Frequency is plotted in units of c/a in Figure 2.1. If the lattice is rescaled by a constant factor $\alpha$, the frequency of the bands will only be multiplied the factor $1/\alpha$. Changing the lattice constant does not change the shape of the bands - it only rescales the bands' frequencies.

In these dimensionless units the band diagram is the same. If the lattice constant ($a$) is multiplied by the factor $\alpha$, the modes will be stretched by the same factor $\alpha$, and the frequency of the bands will be multiplied by the factor $1/\alpha$. This can be shown by using the change of variables $\mathrm{r}' = \alpha\,\mathrm{r}$. The rescaled index function can be written

as $n_\alpha^2(r) = n^2(r/\alpha)$, or in terms of r' as $n_\alpha^2(r') = n^2(r'/\alpha)$ which implies $n_\alpha^2(r') = n^2(r)$.

The new gradient operator will be given by $\nabla_\alpha = \nabla/\alpha$ since $\frac{1}{dr'} = \frac{1}{\alpha dr}$. By replacing r with $r'/\alpha$ the wave equation (2.5) can be written as

$$-\nabla_\alpha \times \left(\frac{1}{n_\alpha{}^2(\mathbf{r}')}\right) \nabla_\alpha \times \mathbf{H}_\alpha\left(\frac{\mathbf{r}'}{\alpha}\right) = \left(\frac{\omega}{\alpha c}\right)^2 \mathbf{H}_\alpha\left(\frac{\mathbf{r}'}{\alpha}\right) \tag{2.15}$$

$\mathbf{H}_\alpha(\mathbf{r}'/\alpha)$ is the new eigenmode with frequency $\omega/\alpha$. With the index scaled by $\alpha$ the new eigenmodes and eigenvectors are just rescaled versions of the original eigenvectors and eigenmodes.

A single band diagram can be plotted in terms the dimensionless frequency units ($\omega$a/2$\pi$c) for all scaled lattice constants. To convert to the actual frequency the dimensionless units are multiplied by c/a. This is also equivalent to plotting the frequency in units of c/a which is the convention for this thesis.

## *Bandgaps*

Sometimes there are no solutions of the wave equation (2.5) for a given range of frequencies and the band diagrams will have a photonic bandgap. In Figure 2.1 a gap in the TE modes occurs from .29 (c/*a*) to .49 (c/*a*). and smaller TM gap occurs from .38(c/a) to .43 (c/*a*). The two-dimensional structure of Figure 2.1 is said to have a complete band gap from .38-.43 (c/*a*). A two dimensional photonic crystal with air holes will tend to have large gaps in the TE modes. While a two dimensional

photonic crystal that consists of dielectric pillars surrounded by air will tend to have large TM gaps.

## *Scaling the index of refraction*

If the index is scaled by a factor $\alpha$ then from equation (2.5), the eigenmodes will be unchanged, and the eigenvectors will be scaled by the factor $1/\alpha$. Lower index material will have higher eigenfrequencies while a higher index material will have lower eigenfrequencies. The index of refraction may be viewed as a potential that

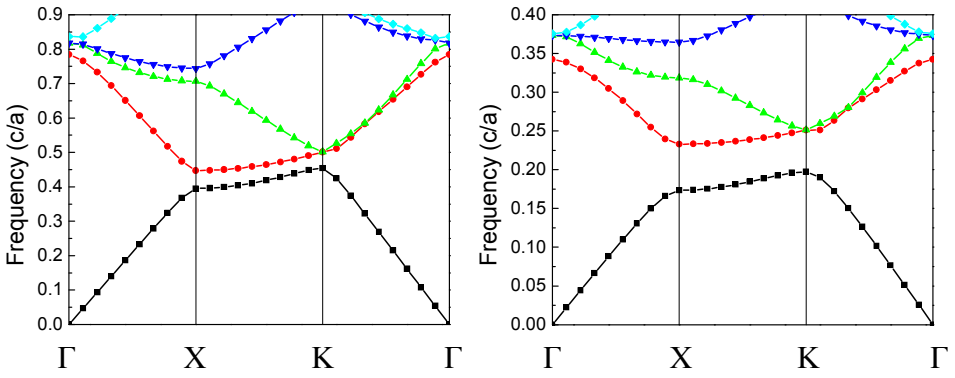


**Figure 2.2** Two-dimensional triagonal photonic crystal. Air hole radius is .45$a$. Left: index of refraction 1.5. Right: index of refraction 3.5**.**

confines photons and a deeper potential has lower energies, or in the case of photons lower frequencies. In general lower frequency modes have more of fields confined in higher dielectric regions. Where as the upper frequency modes will have more of their fields confined in the low dielectric regions or air regions.

Figure 2.2 shows the band diagram of two photonic crystals with identical structures but different values of the index of refraction. The band diagram on the left side of Figure 2.2 has an index of refraction of 1.5 while the band diagram on the right side of Figure 2.2 has an index of refraction of 3.5. Note the different frequency scales of the two diagrams. The bands of the low index structure are at higher frequencies then the bands of the high index structure. The large index of refraction also opens up a bandgap that is not present in the low index structure.

## *Photonic crystal cavities and waveguides*

Light with a frequency in a band gap is forbidden to propagate in the photonic crystal. It will decay exponentially inside the photonic crystal with an imaginary component of the wave vector. Any light whose frequency is in a photonic crystal's bandgap, will be completely reflected when it is incident with on the photonic crystal.

If a uniform dielectric region is surrounded by a photonic crystal light with a photonic bandgap, light will not be able to escape from the region, and will be trapped. Such defects regions will have resonances caused by interference from multiple reflections off the photonic crystal walls. Line defects can form waveguides and point defects can form resonant cavities with dimensions comparable to the wavelength of light.

## *Photonic crystal slabs*

Photonic crystals are fabricated by engineering a dielectric structure with periodic variations in the index of refraction on a length scale on the order of the

wavelength of light. Semiconductor photonic crystals can be made with the same fabrication technology used make integrated electronic circuits. Lithography is used to define patterns such as air holes on a wafer's surface. The patterns can then be transferred into the semiconductors using reactive ion etching.

Two dimensional slab photonic crystals are more amenable to cleanroom fabrication then three dimensional photonic crystals. Three dimensional photonic crystals have been made out of semiconductors using micro-fabrication techniques, but are more difficult to fabricate. Two dimensional slab photonic crystals are periodic in the plane of the wafer's surface. Two dimensional slab photonic crystals are terminated in the direction perpendicular to the wafer's surface by an air-dielectric or high-index - low-index interface. Light is confined in the remaining vertical dimension by total internal refraction at the semiconductor air interface.

Two dimensional photonic crystals do not have a complete three dimensional bandgap. Any light ray that is above the critical angle will escape from the slab. All frequencies even those in the two dimensional bandgap will be able to be transmitted through the slab from the air in this manner.

## *Dielectric slab waveguide modes*

In order to understand photonic crystal slab modes, it is first helpful to review the modes of a uniform dielectric slab waveguide. Light can be trapped inside a uniform dielectric slab by total internal reflection. A simple model of a guided slab mode is a light ray in the geometrical limit that reflects back and forth off the air-dielectric

boundaries as it travels down the slab. The path of the light ray will make a zigzag pattern as shown in Figure 2.3.

The zigzagging light ray can be viewed as a superposition of a transverse light ray and a longitudinal light ray. The transverse component $k_z$ changes directions after each reflection while the longitudinal component $k_{//}$ is constant. For a guided mode the reflecting transverse component of the light ray with wave number $k_z$ must interfere constructively with itself as it reflects back and forth from the air-dielectric interface. Otherwise it will experience destructively interference and will decay as it

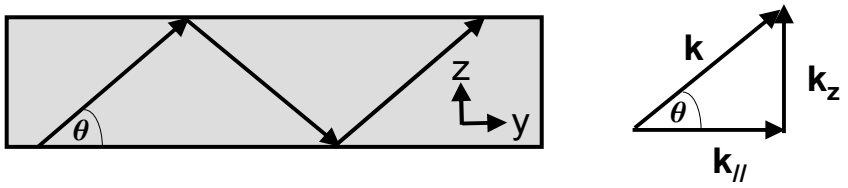


**Figure 2.3** A guided mode in a dielectric slab can be viewed as a light ray undergoing total internal reflection.

propagates. For a guided mode to exist, when the transverse of its light ray returns to the same position its phase must change by $2\pi m$ where $m$ is an integer.

Light will undergo a phase shift when it is totally internally refracted. The phase shift is different for TM polarized and TE polarized light. Here TE and TM refer to an electric field and magnetic fields transverse to the plane of incidence - the zy plane in Figure 2.3. If the slab has infinite width (x-extant) then the dielectric is symmetric

about any mirror reflection in the zy plane. This implies that the slab waveguide modes will separate into TE and TM modes.

If $\phi_{TE/TM}$ is the phase change upon total internal reflection, the transverse resonance condition can then be written as

$$2kd\sin\theta + 2\phi_{TE/TM}(\theta) = 2\pi m \tag{2.16}$$

where $\theta$ is the angle of the light ray with respect to the longitudinal direction, $d$ is the thickness of the slab, $k$ is the wave number of the light inside the slab, and m is a non negative integer. The phase change $\phi_{TE/TM}$ is function of the angle $\theta$. For both TE and TM polarizations the phase shift is zero at the critical angle and approaches $-\pi$ monotonically as the angle of incidence approaches 90°.

The lowest order mode occurs when $m=0$. The lowest order mode is never cut off. As $kd$ goes to zero (2.16) can always be satisfied since $\phi_{TE/TM}$ goes to zero as $\theta$ approaches the critical angle.

As $kd$ is increased more integers ($m$) will be able to satisfy the resonance condition (2.16), and more modes will exists. For a given $kd$, a higher order mode (with a greater value of m) will have a larger value of $\theta$ then a lower order (with a lesser value of m).

The fields for the dielectric slab waveguide can be found by solving the wave equation for the regions inside and outside the slab. Once the fields are solved, an equation equivalent to (2.16) can be obtained by ensuring the fields satisfy the

boundary conditions at the dielectric air interfaces. Inside the dielectric slab the field profiles for the TE electric fields /TM magnetic fields are

$$\begin{aligned} H_{TM} / E_{TE} &\propto \cos(kz)\, e^{i(\omega t - k_{//} y)} \text{ for m even (symmeteric modes)} \\ H_{TM} / E_{TE} &\propto \sin(kz)\, e^{i(\omega t - k_{//} y)} \text{ for m odd (anti-symmeteric modes)} \end{aligned} \tag{2.17}$$

where $z=0$ is taken to lie in the center of the slab. From the form of (2.17) we can see that propagation constant $k_{//}$ is an effective wave vector for the mode. If $k_o$ is the vacuum wave vector, then the wave vector in the slab $k$ is given by $k = n\, k_o$. An effective index $\eta$ of the mode may then be defined by $k_{//} = \eta\, k_o$. The effective index is always less then the actual dielectric index. If the index of refraction of a photonic crystal is increased, the frequency of the bands will also increase. Thus a photonic crystal slab will push the frequency of the bands up from the corresponding two-dimensional photonic crystal.

For guided modes light is trapped inside the dielectric slab. Outside of the slab the guided mode's wave vector is imaginary and the modes will exponentially decay away from the dielectric-air boundary. The fields for the TE electric field/TM magnetic field outside the slab are

$$\begin{aligned} H_{TM} / E_{TE} &\propto e^{-\gamma z} e^{i(\omega t - k_{//} y)} \quad \text{for the region outside the slab where z > 0} \\ H_{TM} / E_{TE} &\propto e^{+\gamma z} e^{i(\omega t - k_{//} y)} \quad \text{for the region outside the slab where z < 0} \end{aligned} \tag{2.18}$$

where $k_o^2 = \beta^2 - \gamma^2$. The evanescent wave vector $\gamma$ can be written in terms of $\theta$ by noting from Figure 2.3 that $\cos\theta = \beta/k$

$$\gamma = k_o \sqrt{\left(n^2 \cos^2\theta - 1\right)} \tag{2.19}$$

For lower order modes with $\theta$ close to zero the evanescent wave vector approaches $k_o\sqrt{\left(n^2-1\right)}$ and the modes decay into the air with an attenuation length $\lambda\left(4\pi^2(n^2-1)\right)^{-1/2}$. Near the critical angle $\theta_c = \cos^{-1}(1/n)$, the evanescent wave vector $\gamma$ goes to zero and the physical extant of the fields will go to infinity. Higher order modes, or any modes where $\theta$ approaches $\theta_c$ will have a significant amount of their energy outside the dielectric slab.

A mode's physical extant into the air, effective index $\eta$, and value of $\theta$ are all interrelated. A mode with a large amount of energy outside the slab will have a low effective index $\eta$. The angle $\theta$ of such a mode will approach the critical angle $\theta_c$. While, the effective index $\eta$ of a mode with most of its energy inside the slab will approach the index of the slab material $n$ and have a small value of $\theta$.

Mathematically, the lowest order TE and TM mode can never be cutoff. However, if the waveguide it too thin, the lowest TE and TM modes can be effectively cutoff. A mathematical solution of a confined mode will still exist. But the evanescent wave vector may be so small that the most of the energy of the mode is spread over a large area outside the slab.

The TM mode is more susceptible to being effectively cut off then the TE mode. To see this one must examine the expressions for the reflected phase changes from total internal reflection[11]

$$\phi_{TE} = -2\tan^{-1}\left(\frac{\gamma}{k_x}\right)$$
$$\phi_{TM} = -2\tan^{-1}\left(n^2\frac{\gamma}{k_x}\right) \tag{2.20}$$

The phase change of the TM reflection ($\phi_{TM}$) will always be greater then the phase change of the TE reflection ($\phi_{TE}$). The terms in the left hand side of the resonance equation (2.16) must sum to zero for the lowest order mode ($m = 0$). Since $\phi_{TM} < \phi_{TE}$, sin $\theta$ will have to be greater for the m=0 TM mode then the m=0 TE mode. In fact for any given $m$, the TM mode resonance will always correspond to a higher

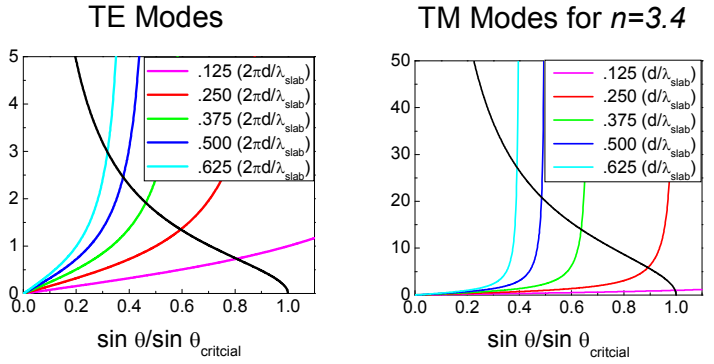


**Figure 2.4** Graphical solutions for the lowest order TE and TM dielectric slab waveguide modes.

angle $\theta$, then the TE mode.

Equation (2.16) and (2.20) can be put in a more useful form by introducing the parameter $\xi = \sin\theta/\sin\theta_c$. The range of $\xi$ is from 0 to 1. It can be regarded as a normalized angle $\theta$ of the light ray. If $V = d/\lambda_{slab}$ for the lowest order mode m=0, the resonance equation (2.20) can be rewritten as

$$\tan\left(2\pi V\xi\right) = n^2\sqrt{\frac{1}{\xi^2}-1} \quad \text{for TM modes}$$
$$\tan\left(2\pi V\xi\right) = \sqrt{\frac{1}{\xi^2}-1} \quad \text{for TE modes} \tag{2.21}$$

The right hand side of equation (2.21) will go to infinity as $\xi$ approaches zero. At the critical angle when $\xi_c = 1$, the left hand side of (2.21) is equal to zero. Figure 2.4 shows plots of the right and left hand sides of equation (2.21) for TE and TM modes. Various values of V are plotted, and an index $n = 3.4$ is used for the TM modes. The intersections of the curves give the solution to the transcendental equations of (2.21). For values of $\xi$ near 1 the modes will be effectively cut-off, most of the mode will propagate outside the waveguide. As the thickness of the waveguide is reduced the TM modes are cutoff before the TE modes. If a high index slab is thin enough only the lowest order TE mode will be able to realistically propagate in it.

## *Photonic crystal slab band diagrams*

For a photonic crystal slab one is not interested in plane waves that pass through the photonic crystal slab at an angle above the critical angle. These extended modes have a large out of plane component ($k_z$) of their wave vectors. One is interested in the guided modes which are trapped inside the slab. In contrast to the extended modes the guided modes have a large in-plane component ($k_{//}$) of their wave vectors.

For this reason the three dimensional band diagram of a photonic crystal slab is projected onto the plane of the photonic crystal. In other words, the frequency is plotted versus the in-plane component of the wave vector ($k_{//}$). Figure 2.5 shows the

band diagram of a triagonal photonic crystal slab. The air hole size is .3$a$, and the thickness of the slab is .5$a$. The out of plane component of the wave vector ($k_z$) is not plotted in Figure 2.5. Its value can be obtained from the expressions $\omega^2 = c^2\left(k_z^2 + k_{//}^2\right)$ outside the slab and $\omega^2 = n^2c^2\left(k_z^2 + k_{//}^2\right)$ inside the slab where $n$ is the slab's index of refraction.

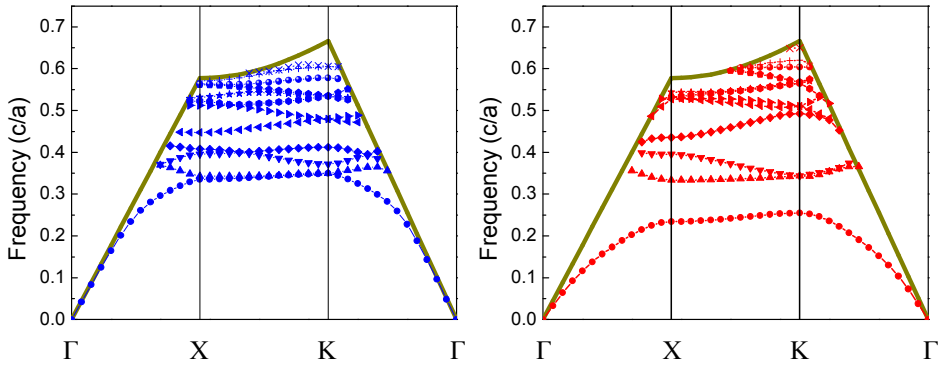


**Figure 2.5** Band diagram of a triangular photonic crystal slab. Slab thickness is .5$a$. Air hole radius is .3$a$. Blue bands: TM modes. Red bands: TE modes. The dark yellow line is the light-line.

The light-line is defined by $\omega_{lightline}^2 = c^2\left(k_{//}^2\right)$. It is shown as a thick black line in Figure 2.5. Above the light-line ( $\omega_{lightline}^2 > c^2\left(k_{//}^2\right)$ ) extended modes in free space can exist with a real out of plane component ($k_z$) of the wave vector. Below the light-line ( $\omega_{lightline}^2 < c^2\left(k_{//}^2\right)$ ) modes in free space are evanescent since $k_z$ must be imaginary to satisfy $\omega^2 = c^2\left(k_z^2 + k_{//}^2\right)$. Modes below the light-line can propagate inside a photonic crystal with a real value of $k_z$ and without attenuation provided the frequency is above what might be termed the dielectric light-line $\omega_{dielectric\ line}^2 = n^2c^2\left(k_{//}^2\right)$. The guided

modes below the light-line cannot couple to free space. They would have an evanescent wave vector above the light-line.

The TE modes in Figure 2.5 have bandgap below the light-line from .25(c/*a*) to .33 (c/*a*). The slab can be thought of as decreasing the effective index of refraction. This will cause the bands of the photonic crystal slab to be at higher frequencies then the bands of the corresponding two dimensional photonic crystals. The bands of the slab may also have modes corresponding to higher order vertical modes. These higher order vertical modes may lie in the bandgap. In general the slab must be made thin enough to cut off the higher frequency modes. However if the slab is two thin the effective index will be too small.

In Figure 2.5 for low frequencies the TM modes are very close to the light-line, and are effectively cut off. The evanescent wave vector outside of the slab ( $\gamma$ ) must be very small, since $\omega^2 = c^2\left(k_{//}^2 - \gamma^2\right)$ and $\omega^2 \approx c^2\left(k_{//}^2\right)$ for light close to the light-line. Thus a large portion of a mode's energy will be outside of the slab if it is just below the light-line the. If the slab is two thin the dispersion of the modes will follow the light-line all the way to the M and X points, and the modes will be effectively cutoff.

The effective index concept from the previous section can be applied to photonic crystal slab modes. The field profiles of these modes will be similar to the field profiles of the corresponding two-dimensional photonic crystal. However the photonic crystal slabs modes will be pushed up in frequency from the two-

dimensional modes by an effective index of refraction. A slab mode with many vertical nodes (a large value of $k_{vertical}$) will have a smaller effective index then a guided mode with no nodes. The dielectric bands of the higher order vertical modes can be pushed up into bandgaps and remove them. For this reason, it is desirable to make photonic crystal thin - to effectively cutoff all the higher order vertical modes.

# 3 Fourier transform infrared spectroscopy

Fourier transform infrared spectroscopy (FTIR) was used to measure spectra of Si THz photonic crystals. FTIR spectroscopy is capable of measuring spectra from the far infrared to visible frequencies. An FTIR is essentially a Michelson interferometer. The detector of the FTIR measures the output of the interferometer as a function of the path difference between two mirrors. As the path difference is changed the fields will interfere constructively and destructively with each other modulating the output. This modulation is the autocorrelation function of the electric field of the source. By taking the Fourier transform of the autocorrelation function the spectrum of the source can found. In general the beamsplitter and detector will have a nonuniform frequency response. In this case the measure spectrum will be a convolution of the frequency dependence of the source, beamsplitter, detector etc. The source of radiation is often an incoherent thermal source with a broad spectrum. The transmission of samples can be found by dividing the spectra of the sample in the beam path by the spectrum without the sample in the beam path.

## *Schematic of FTIR*

A schematic of the FTIR is shown in Figure 3.1. A commercial machine - the Bruker I66V - was used obtain spectra in this thesis. An Mg arc lamp acts as a blackbody and emits a broad range of electromagnetic frequencies. It is desirable for

the temperature of the emitting blackbody to be as high as possible. Even though the tail of the blackbody scales as $1/T^2$ according to the Jeans Raleigh approximation, the total energy emitted by the blackbody will scale as $T^4$. At higher temperatures a blackbody will emit more THz radiation, but the proportion of the THz radiation to the total energy emitted by the blackbody will be less.

A pinhole is used to spatially aperture the electromagnetic radiation to ensure it is spatially coherent. The electromagnetic radiation is collimated and brought to a focus with paraboloidal mirrors. After being collimated, the radiation is sent through a Michelson interferometer consisting of a beamsplitter, a stationary mirror, and a moving mirror. The electromagnetic radiation is then sent through the sample to be measured. The intensity of the electromagnetic radiation is recorded by a detector as a function of the moving mirror's position.

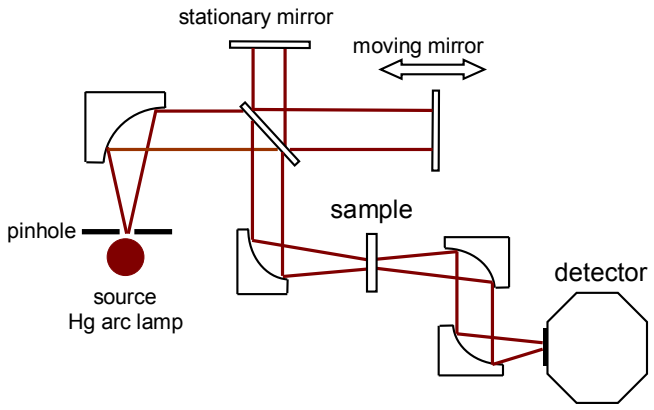


**Figure 3.1** Schematic of the Fourier transform spectrometer instrument (FTIR)

The electric fields from the two arms of the interferometer will interfere as the path length between the mirrors is varied. The output of the detector will be modulated as a function of the moving mirror's position. The recorded modulation is known as an interferogram. By taking the Fourier transform of the interferogram, the spectra may be found.

## *Wiener-Khinchin theorem*

If $E_1(t)$ is the electric field from the stationary arm, and $E_2(t+\tau)$ is the electric field from the moving arm, then the power measured at the detector is proportional to

$$I(\tau) \propto \frac{1}{T} \int_{-T/2}^{T/2} (E_1(t) + E_2(t+\tau))^2 \, dt \tag{3.1}$$

where $\tau$ is the delay time between the two mirrors, and $T$ is the response time or integration time of the detector. The detector's response time is much longer then the period of light (the time scale over which $E_1(t)$, and $E_2(t+\tau)$ vary), and the limit of equation (3.1) can be taken as $T$ goes to infinity. The integrals containing the terms $E_1^2(t)$ and $E_2^2(t+\tau)$ in equation (3.1) do not depend on $\tau$ and are constants. Then the modulated output of the detector will be proportional to

$$I(\tau) \equiv \lim_{T\to\infty} \frac{1}{T} \int_{-T/2}^{+T/2} E(t)E(t-\tau)dt \tag{3.2}$$

The quantity $I(\tau)$ is the interferogram, it is function of the time delay $\tau$ between the two mirrors. Taking the Fourier transform of (3.2) with respect to $\tau$, making the substitution $\tau' = t - \tau$, and noting that the electric field is real, it can be shown that

$$\begin{aligned} F[I(\tau)] &= \int_{-\infty}^{+\infty} \left( \int_{-\infty}^{+\infty} E(t)E(t-\tau)dt \right) e^{-i\omega\tau} d\tau \\ &= \int_{-\infty}^{+\infty} E(t) \left( \int_{-\infty}^{+\infty} E(t-\tau) e^{-i\omega\tau} d\tau \right) dt \\ &= \int_{-\infty}^{+\infty} E(t) e^{-i\omega t} \left( -\int_{+\infty}^{-\infty} e^{i\omega\tau'} E^*(\tau') d\tau' \right) dt \\ &= \left( \int_{-\infty}^{+\infty} E(t) e^{-i\omega t} dt \right) \left( \int_{-\infty}^{\infty} E^*(\tau') e^{i\omega\tau'} d\tau' \right) = \tilde{E}(\omega)\tilde{E}^*(\omega) \end{aligned} \tag{3.3}$$

The Fourier transform of the interferogram is the spectral power density. This

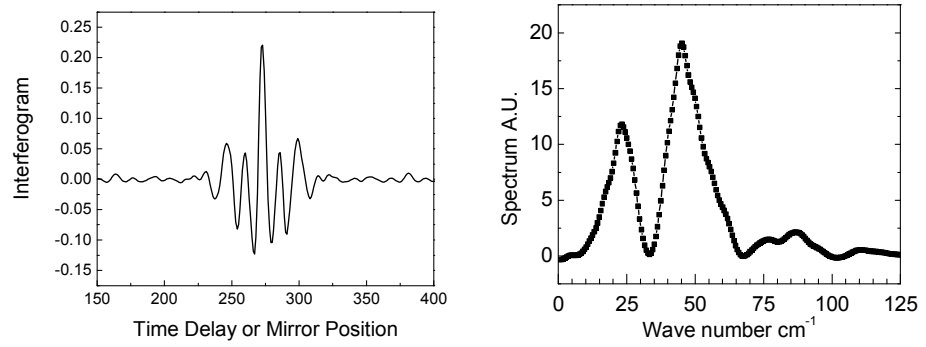


**Figure 3.2** Interferogram of a 100$\mu$m mylar beamsplitter and the corresponding spectrum.

mathematical result is known as the Wiener-Khinchin Theorem.

By recording the output power as a function of the time delay and taking the Fourier transform of the interferogram the spectrum of the light can be found. Figure

3.2 shows an interferogram taken with a 100$\mu$m mylar beamsplitter. The maximum of the interferogram occurs when the path difference between the two mirrors is the same. All frequencies from the source will constructively interfere at this point. In theory the interferogram should always be symmetric about the zero path difference point. In practice there are often small asymmetries in the interferogram. To the right of the interferogram is shown the corresponding spectrum. The minimums in the spectra near 33 $cm^{-1}$ and 67 $cm^{-1}$ are due to fabry-perot reflections in the Mylar beamsplitter. The recorded spectrum will be a combination of the frequency response of the source, the beamsplitter, and the detector.

## *Mylar beamsplitters*

For far infrared frequencies mylar is used as a beamsplitter for the Bruker. Interference between the front and black reflections of the Mylar leads to sinusoidal fabry-perot fringes in the spectrum. The period of the fringes is inversely proportional to the thickness of the mylar. For a slab with thickness $d$, having an index of refraction $n$, and tilted at an angle $\theta$ with respect to the incident light, the period $P$ of the fringes is

$$P = \frac{n}{2d\cos\theta} \tag{3.4}$$

The Bruker has several beamsplitters with different thickness to cover the far-infrared spectral range between 15 $cm^{-1}$ and 600 $cm^{-1}$. For lower frequencies thicker mylar beamsplitters have a greater spectral response. For higher frequencies thinner mylar beamsplitters are more advantageous as they have very broad fringes. A plot

of the period of the fabry perot fringes versus the thickness of the beamsplitters is shown in Figure 3.3. For a Michelson interferometer the angle $\theta$ of the beamsplitter is 45°. Using equation (3.4) the index of refraction of mylar for the far infrared spectral range is found to be 1.78.

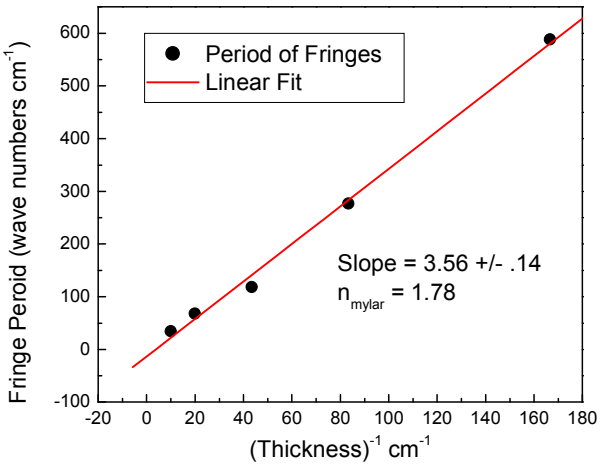


**Figure 3.3** Fringe period of mylar beamsplitter versus mylar beamsplitter thickness.

## *Si composite bolometer*

A commercial Si composite bolometer was used as a detector for the FTIR. The bolometer element increases in temperature when radiation is illuminated on it. The increase in temperature leads to a change in the resistance of the element. A bolometer may be thought of as a thermal absorber and a temperature detector. The change in temperature changes the resistance of the element. The bolometer is operated in series with a load resistor. A constant voltage applied across the bolometer element on the load resistor. A change in resistance of the bolometer

element will change the voltage across it. The in voltage across the bolometer element is often measure with a JFET.

The bolometer has a flat spectral response since it is a thermal detector. Besides the radiation to be measured the bolometer will also detect blackbody radiation given off by objects having a temperature above absolute zero. This thermal emission of photons is a random process and introduces noise. For a detector of area $A$, in radiative contact with a background of temperature $T$ the mean square of thermal photon noise is

$$\overline{P}^2_{thermalphoton} = 16kT^5 A\varepsilon\sigma \tag{3.5}$$

where $k$ is Boltzmann's constant, $\sigma$ is the Stefan Boltzmann's constant, and $\epsilon$ is the emissivity. In addition to thermal photon noise the bolometer element will also be sensitive to noise from temperature fluctuations - phonon noise and noise from thermal motion of charge carriers Johnson noise. The root mean square value do of the phonon an the thermal noise are

$$\overline{P}^2_{phonon} = 4kT^2 G \tag{3.6}$$

$$\overline{P}^2_{Johnson} = 4kT^2 R \tag{3.7}$$

where $G$ is the thermal conductance, and $R$ is the resistance. All of the previous noise sources are thermal in nature and can be reduced by operating the bolometer element at cryogenic temperatures. The composite Si bolometer is in contact with a bath of liquid helium and has an operating temperature of 4.2 Kelvin. To reduce thermal photon noise from objects at higher temperatures the bolometer element is

surrounded by a metal enclosure in contact with the liquid helium bath. A Winston cone connected to the helium bath collects electromagnetic radiation and sends it to the detector. A low pass cold filter on the face of the Winston cone is used as a window. It blocks thermal radiation at higher frequencies emitted by the dewar's

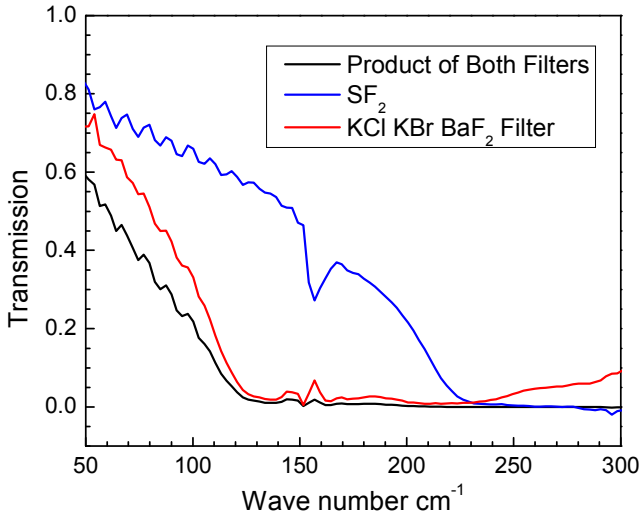


**Figure 3.4** The transmittance the cold filters place inside the bolometer.

outside window and the liquid nitrogen heat shield that surrounds the helium space. This reduces the detector's thermal photon noise given by equation (3.6).

The cold filter in the bolometer had a cutoff of 300 $cm^{-1}$. The signal to noise of the bolometer with the 300$cm^{-1}$ filter was not high enough to make the Si THz photonic crystal measurements preformed in Chapter 4. In order to reduce the noise of the detector two additional cold filters were put inside the bolometer. The filters consisted of salts that absorbed in the far infrared that were mixed into thin sheets of polyethylene. The transmission of the two filters used is shown in Figure 3.4. The

red line shows the transmission of the $SF_2$ filter, while the blue line shows the transmission of the KCl, KCr, and $BaF_2$ filter. The black line is the product of the two transmission lines. The combination of the two filters has a cutoff at 125 $cm^{-1}$. The added cold filter increased the signal to noise ratio of the bolometer and enabled the measurements in Chapter 4 to be performed.

## *Aliasing and apodization*

In order for the Fourier transform of the interferogram to accurately reflect the spectrum care must be taken during the analysis. If the instrument samples the

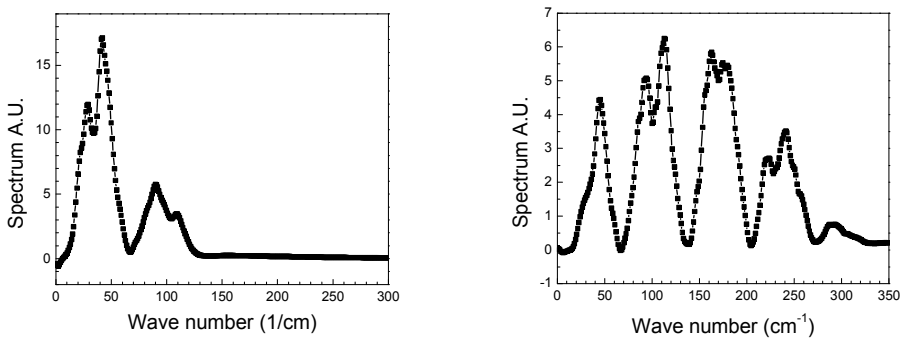


**Figure 3.5** The spectra with a 50$\mu$m beamsplitter. Left: with cold filter. Right: without cold filter.

interferogram at a frequency of 2f then the Nyquist theorems states that the highest recordable frequency will be f. If a frequency higher then this is measured it will be aliased, the high spectral component will appear at a lower frequency.

If the signal is apodized, the interferogram is multiplied by a Gaussian shaped function with a middle corresponding to the peak of the interferogram. Aliasing will

eliminate sharp corners at the end of the interferogram. These corners are constructed from many frequencies components and add spurious components to the spectra.

Noise is uniformly distributed along the length of the interferogram while the signal from the interferogram (from a broadband source) is mostly distributed along the zero time delay point. By apodizing the interferogram the signal to noise ratio of the spectrum is increased at the expense of frequency resolution.

## *Optical and electrical frequency filtering*

The detected power from the bolometer is converted into an electrical signal and recorded as a function of time. The electrical signal is made up of many different electrical frequencies. Each electrical frequency corresponds to a frequency of the measure electromagnetic radiation.

The measured spectrum can be electrically filtered. This is highly advantageous. Instead of inserting a physical filter in the far-infrared beam path, an electrical filter after the detector can be used. By filtering the signal the bandwidth of the measurement is reduced which reduces the noise. Unlike "optical" filters an electrical filter with arbitrary frequency cut-offs can be used.

To make an electrical filter the correspondence between the electrical frequency and the far-infrared frequency must be known. The position of the moving mirror is controlled by a HeNe interferometer and the mirror velocity of the Bruker is given as the number of HeNe fringes per second. Thus a velocity of 10 KHz will correspond to a speed of 3.164 mm/s. 1 THz has a wavelength of 300$\mu$m. Electromagnetic

radiation with a frequency of 1 THz will correspond to an electrical frequency of 10.5 Hz. It is best to measure at the highest scan frequencies at which the signal is not attenuated by the detector's response time. This avoids 1/f noise and allows more scans to be taken when averaging.

# 4 Two-dimensional Si photonic crystals

The first photonic crystal structures that we produced were made out of high restively Si wafers and fabricating using Deep Reactive Ion Etching (DRIE). Rectangular holes were etched in Si with the spacing of a rectangular lattice. Radiation from the FTIR was coupled into and out of the edges of the Si wafers.

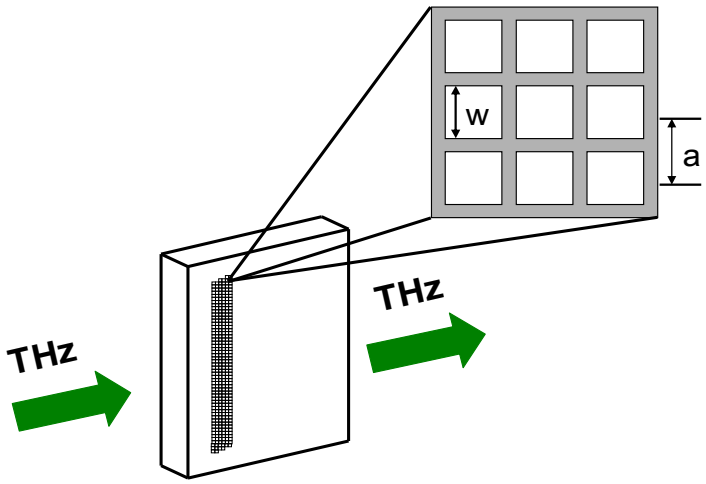


**Figure 4.1** Schematic of the transmission measurement of the THz Si photonic crystals.

Because the THz radiation was coupled from free space and the index of Si is very high, the THz radiation will be refracted at small angles with respect to the plane of the wafer. The THz radiation will only couple into the lowest order waveguides modes. Higher order modes do not have to be cut-off be thinning the Si wafer since they are not couple into from free space. The spectra of samples with and without

etched holes were measured. For TE polarized THz radiation stop bands were found in samples with photonic crystals that were not present in samples without photonic crystals. The width and position of the stop-bands was consistent with a two-dimensional calculation of the TE bandgaps.

## *High resistivity Si*

High resistivity Si has excellent THz optical properties. Its index of refraction is high $n_{THz}$ 3.42 and its absorption is low. Absorption at THz frequencies in Si is caused by free carrier absorption. The free carriers in semiconductors can be thought of as dilute plasma. The response of a plasma is characterized by the plasma frequency

$$\omega_{plasma} \equiv \sqrt{\frac{ne^2}{\varepsilon m^*}} \tag{4.1}$$

where $n$ is the free carrier density, $e$ is the charge of the electron $\epsilon$ is the dielectric permittivity and $m^*$ is the electron's effective mass. For frequencies below $\omega_{plasma}$ strong absorption will occur. For frequencies above $\omega_{plasma}$ the plasma will not be able to respond fast enough and no absorption will occur. Si with resistivity of .001 Ω-cm ($10^{20}cm^{-3}$) has a plasma frequency of 14.1 THz while Si with a resistivity of 500 Ω-cm ($10^{13}cm^{-3}$) has a plasma frequency of 4.45 GHz. By varying the doping, Si wafers can be either metals or insulators at THz frequencies. The photonic crystal samples were made out of 500 $\mu$m thick float-zone Si wafers with a resistivity of 8-9 KΩ-cm.

## *Photonic crystal dimensions*

Air holes were etched into the Si wafers using Deep Reactive Ion etching. The holes were rectangular and arrayed in a rectangular lattice. The same DRIE also defined the edges of the samples. The dimension of the samples was 8 by 11 mm. The photonic crystals consisted of 10 arrays of rectangular holes 10 mm long. The mask used for photolithography had 3 patterns – 60$\mu$m holes in a 75$\mu$m lattice, 80 $\mu$m holes in a 100$\mu$m lattice and 100$\mu$m holes in a 125$\mu$m lattice. The photomask was made using an older (obsolete) machine. The minimum feature size was 5$\mu$m and all features had to be rectangular. This pushed the machine to its limits as the spacing between air holes was 15$\mu$m, 20$\mu$m and 25$\mu$m respectively. The part of the mask with the 60$\mu$m features had large variations the size of the strips separating the holes. Samples could not be produced using the 60/75 portion of the mask.

## *Fabrication of samples*

The fabrication of the THz photonic crystals was challenging, as the air holes were etched through 500$\mu$m hick wafers and the spacing between the air holes was 20$\mu$m and 25$\mu$m thick. The masks used during the DRIE etch had to have nearly anisotropic sidewalls, and be thick enough to not be removed during the etch. $SiO_2$ was used as hard mask for the DRIE of the Si photonic crystals. It has a nominal selectivity for $SiO_2$:Si of 200:1. (The selectivity will vary depending on the conditions of the etch.) The $SiO_2$ hard mask could not be defined by isotropic wet

etching in hydrofluoric acid, since anisotropic sidewalls were needed. Conventional reactive ion etching was used to pattern the $SiO_2$ hard mask.

The gases $CHF_3/O_2$ gases are often used to etch $SiO_2$ and provide a relatively

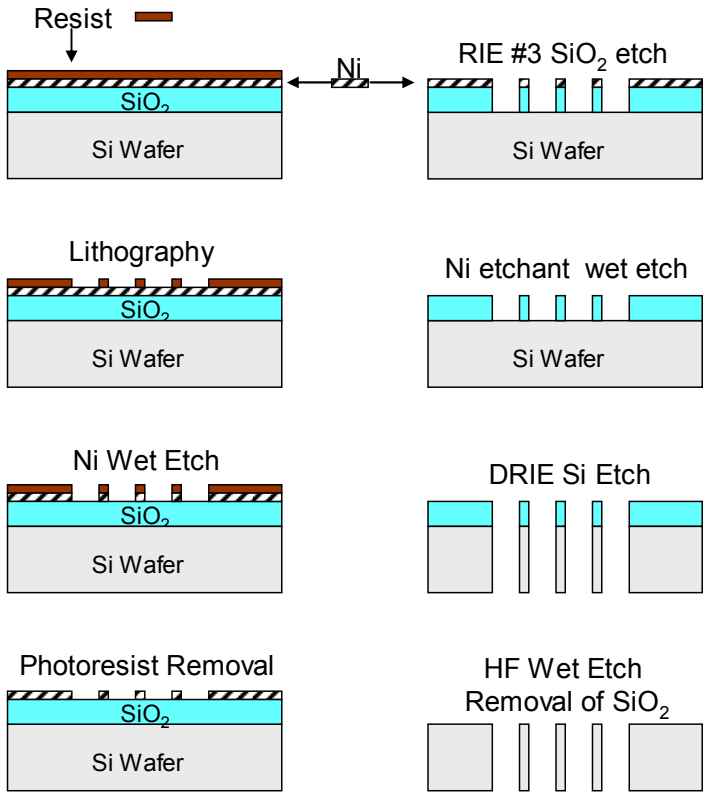


**Figure 4.2** Fabrication process for THz Si photonic crystals.

high selectivity with respect to photo resist. However, when these gases were used during reactive ion etching of $SiO_2$ hard masks, residue was left on the exposed Si. These residues were believed to be carbon based polymers (originating from the photoresist mask) that formed during the reactive ion etching. Attempts to remove them were unsuccessful. During the DRIE etch of the Si wafers, these carbon based

residues acted as micro masks which lead to the formation of Si spikes (commonly referred to as "grass") during the DRIE etch. The grass was thick enough to retard the etch and resulted in a negligible etch rate of Si.

In order to circumvent these problems a$SF_6/Ar/O_2$ chemistry was used for the reactive ion etching of $SiO_2$. This combination of gases etched the $SiO_2$ more rapidly then $CHF_3/O_2$, but was also found to attack the photoresist. Instead of photoresist a metal mask of Nickel was as a mask for the etching of the $SiO_2$. The selectivity of Ni to $SiO_2$ during the RIE was on the order of 40. 250 nm of Ni was evaporated onto the $SiO_2$ thick. This was thin enough for the sidewall profile of the Ni to not be important. An isotropic wet etch was used to define the Ni pattern.

During the DRIE of Si the removal rate of the $SiO_2$ hard mask was found to be greater then the nominal selectivity of $Si:SiO_2$ would indicate. The increase in the etch rate of the $SiO_2$ was believed to be due to thermal effects. Samples that are etched in the DRIE are bonded (with resist) to a carrier wafer whose underside is cooled by He gas flow during the etch. If samples are not bonded the mask material will be stripped off during the etch. Masks can be completely removed from unbounded samples that are etched for only a few minutes. During the DRIE etch the ridges around the holes become thermally isolated from the rest of the Si wafer. It is believed this leads to an increase in temperature of the $SiO_2$ mask and facilities its removal.

To combat these effects two strategies were employed. First a thick 4.5$\mu$m layer of $SiO_2$ was used as a mask. Second during the etch the DRIE was programmed to

shut off after 50 etching loops, wait for a specified period of time to allow the $SiO_2$ hard mask on the ridges to cool, and then resume etching.

After the DRIE the $SiO_2$ hard mask was removed with hydrofluoric acid. Figure 4.2 shows an outline of all the processing steps. Figure 4.3 shows SEM photographs of the $SiO_2$ hard mask and DRIE Si etches. For the reactive ion etch of $SiO_2$ at the Si

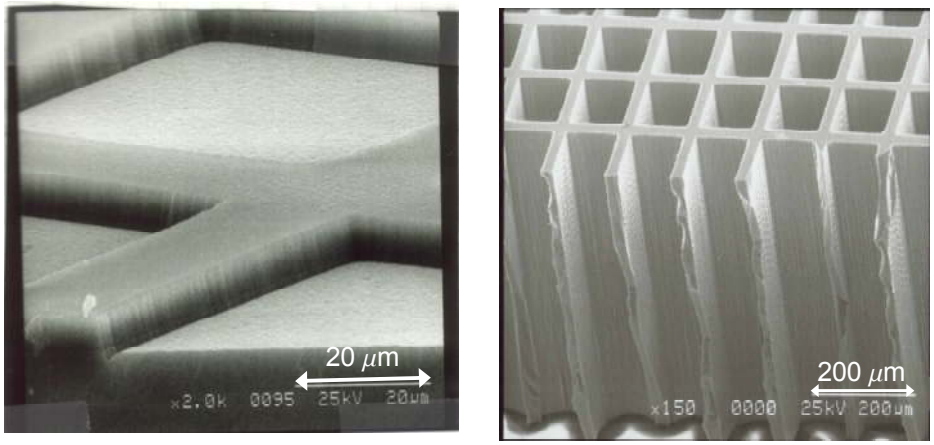


**Figure 4.3** SEM pictures of reactive ion etches. Left: $SiO_2$ hard mask. Right: Si photonic crystal.

forms a small ditch at the bottom of the exposed $SiO_2$. This phenomenon is known as trenching. If the sidewalls are not completely vertical, ions can be deflected towards the border of the mask. This can result an increase removal of material at the mask's edge from the increase ions flux. The photonic crystals samples could not be cleaved, since the air holes were etched all the way through the wafer. To obtain the SEM picture in Figure 4.3 the photonic crystal sample was broken in two which accounts for the rough edges. At the top of the wafers the corners of the rectangular

air holes are sharp. However the DRIE etch progress the corners become slightly rounded as can be seen at the bottom of the photonic crystal sample in Figure 4.3.

When this work was done RIE #3 was the only machine in the cleanroom capable of etching $SiO_2$. After this work was completed a Panasonic inductively couple plasma (ICP) etcher was installed in the cleanroom. The plasma formed by an ICP chamber is much denser then the plasma in a conventional RIE chamber, and the etch rate is proportional to the density of ions.

The long times (several hours for $CHF_3/O_2$ chemistries) of the $SiO_2$ etches in RIE #3 lead to heating of the samples which is believed initiate polymer formation. For short (several minutes) etches of $SiO_2$ with $CHF_3/O_2$, no polymer formation was observed. Etches several microns thick $SiO_2$ in the Panasonic ICP with a $CHF_3/O_2$ chemistry will be must faster then conventional RIE etches, and will most likely occur with polymer formation.

## *Coupling THz radiation into Si wafers*

Transmission spectra of the Si photonic crystals were taken with the Bruker FTIR spectrometer. THz radiation was coupled into and out of the edges of the samples using Winston cylinders. The Winston cylinders preserved the THz polarization while concentrating it along the wafer's edges. Paper with gold lines (with a periodic of 25$\mu$m) was used as a wire-grid polarizer. To ensure no light traveled thought both Winston cylinders without traveling through the sample, two THz absorbing pieces of foams were inserted on each side of the sample. Reference

samples were to provide a background spectrum. They were cleaved from the same 8-9 KΩ-cm wafer and were approximately the same size as the photonic crystal samples.

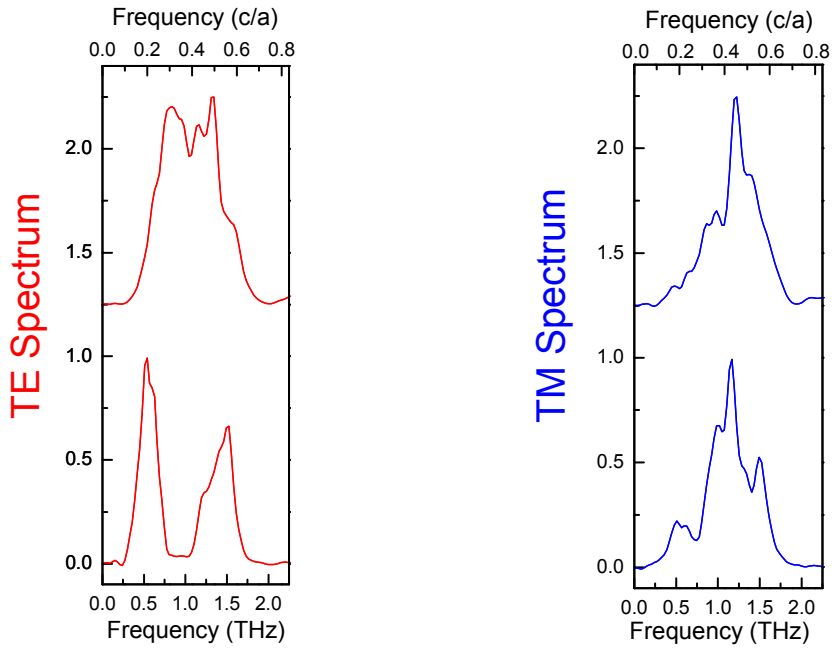


**Figure 4.4** Top: Transmission of the Si reference. Bottom**:** Transmission of a Si photonic crystal with lattice a constant 100 $\mu$m.

The critical angle of Si at THz frequencies is 74°. All of the light rays that are coupled into the slab waveguide will deviate no more then 16° from the in-plane direction. The majority of the coupled light will be refracted very close to normal incidence inside the Si wafer. The THz radiation will only couple into the lowest order dielectric waveguides modes and the photonic crystal can be approximated as a two-dimensional. If THz radiation was generated inside the Si, higher order slab the

radiation would couple to higher order slab modes, and the photonic crystal could not be approximated as two-dimensional.

The transmitted signal was detected with a liquid helium cooled composite Si bolometer. The bolometer had a cold filter with a cut-off of 125cm$^{-1}$ (~3.8 THz). A preamplifier inside the bolometer's dewar amplified the signal by 60 dB. The signal from the bolometer was amplified again at room temperature with a Stanford Research System preamplifier. The gain of the preamplifier was typically set to 100. The preamplifier was also used to electrically filter the signal with 1 to 100 Hz band pass with a roll-off of 6dB roll-off. The scanner velocity (HeNe fringes per seconds) was typically set to 20 KHz.

## *Experimental data*

Figure 4.4 shows the raw transmission spectra for the sample with a lattice constant of 100$\mu$m. The Au paper polarizer was used to select between the TM and TE spectra. The spectra are labeled TE for the case when the electric field was polarized parallel to the wafer's edge TM for when the electric field was perpendicular to the to the wafer's edge. The TE spectrum in Figure 4.4 shows a large stop band in the middle of the spectrum. The reference sample of unetched Si does not have a stop band.

The maximum values of the spectra in Figure 4.4 are normalized for clarity. The transmission through the reference samples were always greater then the transmission through the photonic crystal samples. The reference samples had two cleaved

interfaces, while the photonic crystals samples had 20 interfaces defined by the etch. Scattering from surface roughness along the etched interfaces is believed to cause the lower throughput of the photonic crystal samples.

The ratio of the air-hole width to the lattice constant was the same (.8) for the

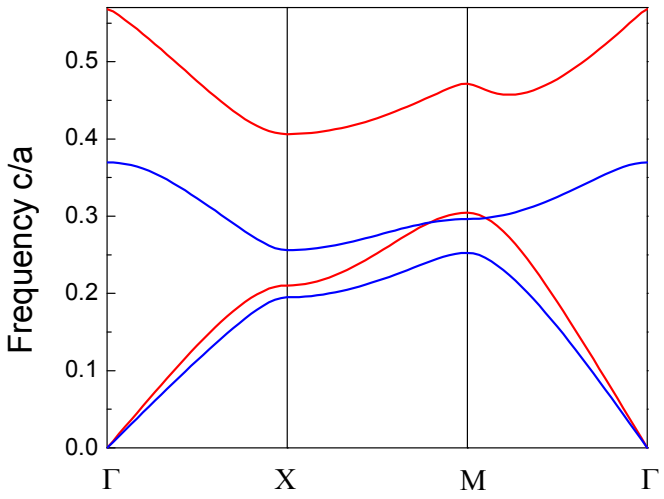


**Figure 4.5** The two lowest bands of a rectangular photonic crystal having rectangular air holes with a radius of .4*a*. Red: TE bands. Blue: TM bands

photonic crystal samples. The photonic crystal samples had the same band-diagram in units of *c/a*. The two-dimensional band diagram of the two lowest bands is shown in Figure 4.5. The band diagram was calculated using the MIT Photonic bandgap software package[12,13]. A large band gap for TE modes exists for frequencies between .31 *c/a* and .47 *c/a*. No band gap exists for the TM modes. The frequency of the dielectric band at the M point is .252 *c/a* while the frequency of the air band at the X point is .256 *c/a*. The measurements were taken in the Γ-X direction. (Because the

older mask making machining was incapable of making nonrectangular patterns, it was not possible to make a photonic crystal for the Γ-M direction.) The gap in the Γ-X direction for the TE modes is from .21 *c/a* to .47 *c/a*, and .20 *c/a* to .25 *c/a* for the TM modes. The stop band in Figure 4.4 corresponds to the gap in the Γ-X direction

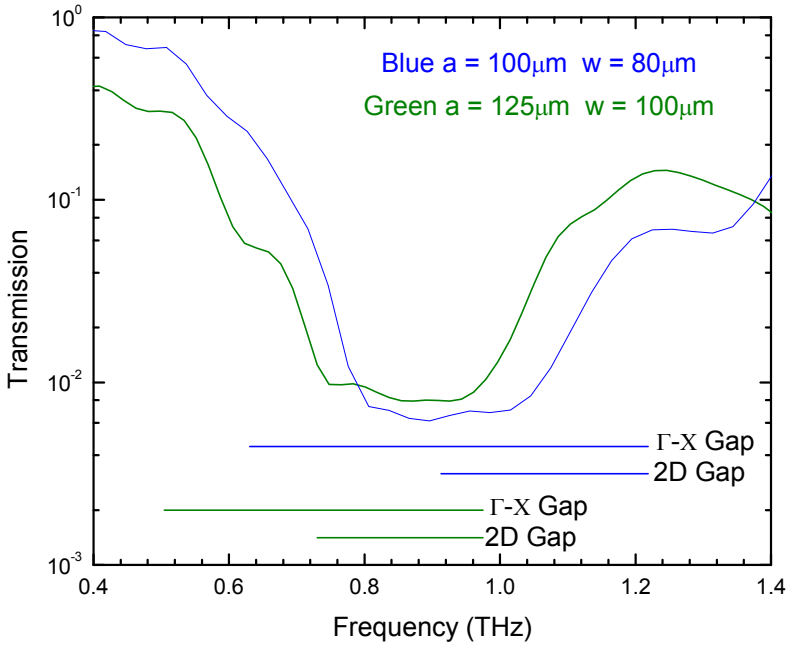


**Figure 4.6** Transmission of Si photonic crystals. Blue: 100$\mu$m Green: 80$\mu$m

for the TE modes. It is not know if the dip in the TM spectrum in Figure 4.4 corresponds to the gap in the Γ-X direction, or is an artifact of the measurement.

In Figure 4.6, the transmission of the both the 100$\mu$m and 125$\mu$m sample are plotted for TE polarization. The bandgap of the 125$\mu$m sample is at a lower frequency then the 100$\mu$m sample. This is to be expected since the frequencies of the band diagrams should scale with the lattice constant. The gaps in the Γ-X direction and the complete band gaps are shown as lines under the transmission in Figure 4.6.

The stop bands are smaller then would be predicted from the band diagram of Figure 4.5. There could be several reasons for the discrepancies. As the DRIE etched progressed, it was found that the corners of the etches would become round. This can been seen from Figure 4.3 in the SEM picture of the DRIE etch. The photonic crystal was 10 periods long. Frequencies inside the band gap will have evanescent wave vectors. As the frequency propagates it will be decay exponentially away. If the photonic crystal is not thick enough, these frequencies could tunnel through it. Frequencies near the center of the gap should decay very quickly while frequencies near the edges of the gap would not decay as fast

# 5 Free space electro-optic sampling

The electric field of THz radiation can be measured by taking advantage of the electro-optic effect in a crystal. The electro-optic effect is a birefringence in a crystal caused by an applied electric field across the crystal. If a laser probe beam is sent through the crystal, its components along the principal axes will experience a shift in phase (Γ) proportional to the applied electric field. By measuring the phase shift of

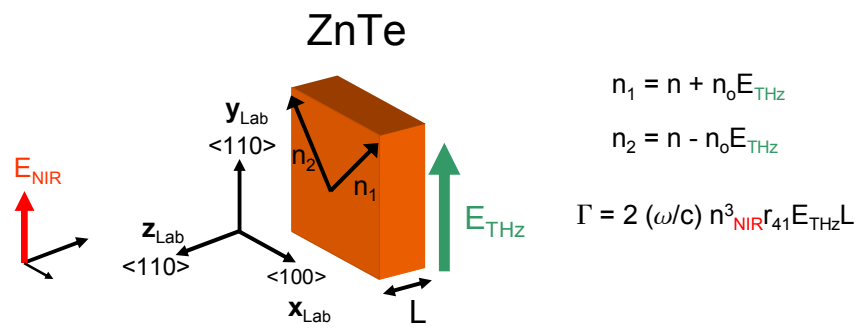


**Figure 5.1** A THz electric field in the <110> direction will induce a change in the principal indices of refraction ($n_1$ and $n_2$). When a probe travels through the ZnTe crystal it will experience a change in retardance (Γ) proportional the electric field. By measuring the retardance of the probe the applied electric field ($E_{THz}$) can be found.

the transmitted probe beam the applied electric field in the crystal can be found.

If there is a phase difference between the probe beam's different polarization components, the probe beam will be elliptically polarized. If the phase shift is small (<<1), the elliptically polarized probe beam can be approximated as linearly polarized light rotated by an angle (Γ) equal to the phase shift of between the principle axes.

For free space electro-optic sampling, the applied electric field is the field from a free-space THz pulse, and the probe beam is a femtosecond laser pulse locked in time

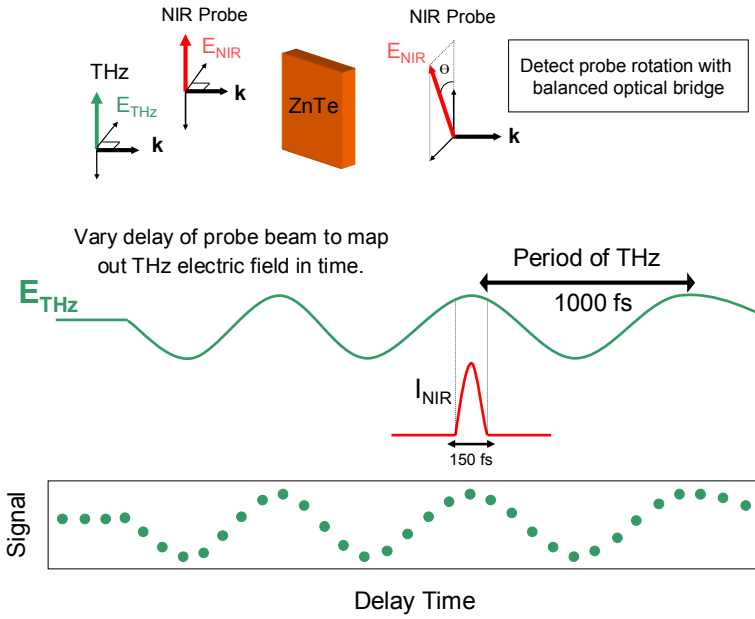


**Figure 5.2** Free space electro-optic sampling. THz beam and near infrared (NIR) probe are sent through a ZnTe crystal. The rotation of the probe beam is proportional to the electric field. The duration of a femtosecond probe beam is small compare to the period of THz radiation. If the probe beam is delayed in time with respect to the THz radiation the electric field of the THz radiation can be measured as function of time.

with the THz pulse[14] The THz beam and probe beam are both sent collinearly through an electro-optic crystal - often ZnTe. The width of the femtosecond laser pulse is less then time scale on which the THz pulse's electric field varies. If the group velocities of the THz and probe pulses are the same in the electro-optic crystal, the probe pulse will only sample one value of the THz electric field. The time delay between the laser probe beam and the THz radiation is varied. The rotation of the probe beam (which is proportional to the THz electric field) is recorded with respect

to the delay time. The THz induced rotation $\Gamma$ of the probe beam is very small - typically less then $10^{-4}$ radians.

The duration of the ultrafast probe beam must be small compared to the period of the THz radiation. Otherwise the trailing and leading edges of the probe beam will experience different values of the THz electric field. To avoid the probe beam becoming delayed or advanced with respect the THz electric field, the group velocity mismatch between the THz and probe beam in the ZnTe crystals should be small. A finite group velocity mismatch will limit the length of the ZnTe crystal. The group velocity mismatch and finite duration of the probe beam will have more effect on higher THz frequencies which have more abrupt THz field variations then lower frequencies.

There are several advantages of electric optic detection over bolometric and pyroelectric detection. The electric field is directly measured. All of the intensity and phase information of the THz pulse is obtained. The dynamic range of electric field measurements is greater then the dynamic range of power measurements. If an electric field and power measurement both have the same signal to noise ratio of $10^x$, the dynamic range of a transmission measurement would be $10^{2x}$ for the electric field measurement and $10^x$ for the power measurement. In THz electro-optic sampling only the probe beam power is directly measured. There is no need for cryogens to cool bolometers operating liquid helium temperatures.

There are disadvantages of electric optic detection. A femtosecond laser is needed. The probe beam must be locked in time with THz beam. The THz radiation

must be generated by the same femtosecond laser that produces the probe pulses. Adjusting mirrors may change the time delay between the femtosecond probe pulse and the THz beam. This will lead to a loss of signal even through the strength of the signal may have actually increased. This can lead to difficulties in maximizing the signal.

In the rest of this chapter free space electro-optic sampling is described in more detail along with the experimental electro-optic setup used for the measurements in Chapters 6 and 8. It is first explained under what conditions a THz electric field will induce a detectable birefringence in a ZnTe crystal. In order to do this it is first necessary to review the index ellipsoid and introduce the electro-optic tensor. The THz induced birefringence is then calculated for THz electric fields parallel to the <110> and <100> axis of the ZnTe crystal.

The measurement of the probe beam's rotation with a balance optical bridge is described using Jones vectors to describe the polarization state of the probe beam.

Once it is known how a THz field induces a detectable birefringence in the ZnTe, and how the optical bridge works, the reader is better equipped to understand the experimental setup when it is described in more detail. Lastly sources of measurement noise are discussed along with the measurement of the system's noise floor.

## *Index ellipsoid for a birefringent material*

In a material with a nonisotropic permittivity, the index of refraction of light depends on its direction and is described by the index ellipsoid[15].

$$\left(\frac{1}{n^2}\right)_1 x^2 + \left(\frac{1}{n^2}\right)_2 y^2 + \left(\frac{1}{n^2}\right)_3 z^2 + \left(\frac{1}{n^2}\right)_4 yz + \left(\frac{1}{n^2}\right)_5 xz + \left(\frac{1}{n^2}\right)_6 xy = 1 \qquad (5.1)$$

Equation (5.1) can be rewritten in matrix form as

$$\begin{pmatrix} x & y & z \end{pmatrix} \begin{pmatrix} \left(\frac{1}{n^2}\right)_1 & \frac{1}{2}\left(\frac{1}{n^2}\right)_6 & \frac{1}{2}\left(\frac{1}{n^2}\right)_5 \\ \frac{1}{2}\left(\frac{1}{2n^2}\right)_6 & \left(\frac{1}{n^2}\right)_2 & \frac{1}{2}\left(\frac{1}{n^2}\right)_4 \\ \frac{1}{2}\left(\frac{1}{2n^2}\right)_5 & \frac{1}{2}\left(\frac{1}{2n^2}\right)_4 & \left(\frac{1}{n^2}\right)_3 \end{pmatrix} \begin{pmatrix} x \\ y \\ z \end{pmatrix} = 1 \qquad (5.2)$$

The 3x3 index ellipsoid matrix in equation (5.2) can be decomposed into the product $\mathbf{U}^{-1}\mathbf{D}\mathbf{U}$ where $\mathbf{U}$ is a unitary matrix and $\mathbf{D}$ is a diagonal matrix. Multiplication by a unitary matrix is equivalent to a rotation of the coordinate system. In the coordinate system which diagonalizes the index ellipsoid matrix (5.2) equation (5.1) can written as

$$\left(\frac{1}{n^2}\right)' x'^2 + \left(\frac{1}{n^2}\right)' y'^2 + \left(\frac{1}{n^2}\right)' z'^2 = 1 \qquad (5.3)$$

where $\left(\frac{1}{n^2}\right)'_1 \left(\frac{1}{n^2}\right)'_2 \left(\frac{1}{n^2}\right)'_3$ are the eigenvalues of the index ellipsoid matrix (5.2). The primed coordinates in which the index ellipsoid is diaganolized can be written in terms of the unprimed coordinates as

$$\begin{pmatrix} x' \\ y' \\ z' \end{pmatrix} = \mathbf{U}^{-1} \begin{pmatrix} x \\ y \\ z \end{pmatrix} \tag{5.4}$$

The $x', y', z'$ coordinates are the principal axis of the index ellipsoid. From the eigenvalues of the index ellipsoid the index of refraction along each of the principal axes can be found.

## *Electro-optic tensor*

For a material with a 2nd order nonlinear susceptibility $\chi^2$ an applied electric field will change the coefficients $\left(\frac{1}{\mathrm{n}^2}\right)_i$ in the index ellipsoid (5.1). This change in the coefficients $\Delta\left(\frac{1}{\mathrm{n}^2}\right)_i$ be described by the electro-optic tensor $r_{ij}$ [16]

$$\Delta\left(\frac{1}{\mathrm{n}^2}\right)_{\mathrm{i}} = \sum r_{ij} E_j \tag{5.5}$$

The electro-optic tensor is 3x6 matrix. For the Zinc blende class of crystals which includes GaAs and ZnTe the only non-zero components of th8 electro-optic tensor are $r_{41}, r_{52}$, and $r_{63}$ which have the same value $r_{41} = r_{52} = r_{63}$ [16]

## *Coordinate systems*

To find the change in retardance ($\Delta\Gamma$) induced by the THz electric field it is necessary to use three coordinate systems; the coordinate system of the crystal axes, the coordinate system of the principle axes, and the coordinate system of the lab

frame. Throughout this chapter, the coordinate system of the lab frame will be denoted as $x_{lab}, y_{lab}, z_{lab}$, the coordinate system of the crystal axes will be denoted as $x, y, z$, and the coordinate system of the principal axes will be denoted as $x', y', z'$. The lab coordinate system is shown in Figure 5.1. The components of the electro optic tensor $r_{ij}$ (equation (5.5)) are given in terms of the crystal axes $x, y, z$. Equation (5.1) must be written in the same $x, y, z$ coordinate system of the crystal axes. The principles axes $x', y', z'$ can be found by diagonalizing the index ellipsoid equation (5.1) and (5.2).

## *Index ellipsoid and electro-optic tensor*

According to equation (5.5)the coefficients of the index ellipsoid are modified slightly by the product of the electro-optic tensor $r_{ij}$ and the electric field vector $E_j$. If index of ZnTe is taken as *n,* and is assumed to be isotropic in the absence of an applied field, then the index ellipsoid in the presence of an electric field is

$$\left(\frac{1}{\mathrm{n}}\right)_1^2 x^2 + \left(\frac{1}{\mathrm{n}}\right)_2^2 y^2 + \left(\frac{1}{\mathrm{n}}\right)_3^2 z^2 + E_1 r_{41} yz + E_2 r_{41} xz + E_3 r_{41} xy = 1 \qquad (5.6)$$

Equation (5.6) can be written in matrix form as

$$\begin{pmatrix} x & y & z \end{pmatrix} \begin{pmatrix} \left(\frac{1}{\mathrm{n}^2}\right)_1 & \frac{E_1 r_{41}}{2} & \frac{E_2 r_{41}}{2} \\ \frac{E_1 r_{41}}{2} & \left(\frac{1}{\mathrm{n}^2}\right)_2 & \frac{E_3 r_{41}}{2} \\ \frac{E_2 r_{41}}{2} & \frac{E_3 r_{41}}{2} & \left(\frac{1}{\mathrm{n}^2}\right)_3 \end{pmatrix} \begin{pmatrix} x \\ y \\ z \end{pmatrix} = 1 \qquad (5.7)$$

To find the principal axes equation (5.6) must be diaganolized. The principal axes will depend on the direction of the electric field. Each time the direction of the field changes equation (5.6) will have to be rediagonalized to find the principal axes. For specific directions of the THz electric field, the ZnTe crystal will become birefringent.

## *Orientation of the ZnTe wafer*

A <110> ZnTe wafer was used to measure the THz electric field as shown in Figure 5.1. The THz beam and probe beam were sent through the ZnTe along the <110> direction normal to the surface of the ZnTe wafer. The <110> direction of the crystal lies along the normal of the wafer, and the <110> and <100> directions lie along the edges of the ZnTe wafer. The THz and probe beam wave vectors normal to the surface of the ZnTe wafer. The THz and probe beam polarizations are always in the plane of the wafer, perpendicular to the wafer's normal.

To apply equation (5.6) the THz electric field must bet written in the coordinate system of crystal axes. To do this each unit vector of the lab frame $x_{lab}, y_{lab}, z_{lab}$ must be written in terms of the crystal coordinates. From Figure 5.1 we can write

$$\begin{aligned} x_{lab} &= \begin{pmatrix} 0 & 1 & 0 \end{pmatrix}_{crystal\ cordinates} \\ y_{lab} &= \begin{pmatrix} \frac{1}{\sqrt{2}} & 0 & \frac{-1}{\sqrt{2}} \end{pmatrix}_{crystal\ cordinates} \\ z_{lab} &= \begin{pmatrix} \frac{1}{\sqrt{2}} & 0 & \frac{1}{\sqrt{2}} \end{pmatrix}_{crystal\ cordinates} \end{aligned} \tag{5.8}$$

The THz electric field must lie in the plane of the wafer. The normalized THz electric field in the crystal axes can be written as

$$\left( \pm\sqrt{\frac{1-E_2}{2}}, \quad E_2, \quad \mp\sqrt{\frac{1-E_2}{2}} \right)_{crystal\ cordinates} \tag{5.9}$$

where $E_2$ is the normalized value of the THz electric field in the $x_{lab}$ direction.

Two cases of importance are when the THz electric field is parallel to the <110> edge of the ZnTe crystal and when the THz electric field is parallel to the <100> edge of the ZnTe crystal. For the case of an THz electric field parallel to the <110> edge the THz electric field in the coordinate of the crystal lattice can be written as

$$E\left( \frac{1}{\sqrt{2}} \quad 0 \quad \frac{-1}{\sqrt{2}} \right)_{crystal\ cordinates} \quad parallel\ to\ \langle 110 \rangle\ edge \tag{5.10}$$

When the electric field is parallel to the <100> edge of the ZnTe crystal, the THz electric field can be written in the coordinate of the crystal lattice as

$$E\left(0 \quad 1 \quad 0\right)_{crystal\ cordinates} \ parallel\ to\ \langle 100 \rangle\ edge \tag{5.11}$$

In the following two sections the THz induced retardance of the probe beam is calculated for the THz electric field polarized in the $y_{lab}$ and $x_{lab}$ directions. Any incident THz electric field (whose wave vector is normal to the ZnTe) can be decomposed into components along the $x_{lab}$ and $y_{lab}$ directions. By calculating the retardance for fields along $x_{lab}$ and $y_{lab}$ the response of the ZnTe crystal can be characterized for all THz polarizations in the plane of the ZnTe wafer.

### *Electric field parallel to the <110> edge of the ZnTe crystal*

When the THz electric field is in the $y_{lab}$ direction its electric field in the crystal coordinate axes is given by(5.10). Substituting the THz electric field (5.10) into the index ellipsoid (5.6) and writing the index ellipsoid in matrix form gives

$$\begin{pmatrix} x & y & z \end{pmatrix} \begin{pmatrix} \left(\frac{1}{n^2}\right) & -\frac{r_{14}E}{2\sqrt{2}} & 0 \\ -\frac{r_{14}E}{2\sqrt{2}} & \left(\frac{1}{n^2}\right) & \frac{r_{14}E}{2\sqrt{2}} \\ 0 & \frac{r_{14}E}{2\sqrt{2}} & \left(\frac{1}{n^2}\right) \end{pmatrix} \begin{pmatrix} x \\ y \\ z \end{pmatrix} = 1 \tag{5.12}$$

The eigenvalues and corresponding eigenvectors of equation (5.12) are

$$\begin{aligned} \left(\frac{1}{n^2}\right) \quad & \begin{pmatrix} \frac{1}{\sqrt{2}} & 0 & \frac{1}{\sqrt{2}} \end{pmatrix} = z_{lab} = z' \\ \left(\frac{1}{n^2} - \frac{r_{14}E}{2}\right) \quad & \begin{pmatrix} \frac{1}{2} & \frac{1}{\sqrt{2}} & \frac{-1}{2} \end{pmatrix} = \frac{\left(x_{lab} + y_{lab}\right)}{\sqrt{2}} = x' \\ \left(\frac{1}{n^2} + \frac{r_{14}E}{2}\right) \quad & \begin{pmatrix} \frac{-1}{2} & \frac{1}{\sqrt{2}} & \frac{1}{2} \end{pmatrix} = \frac{\left(x_{lab} - y_{lab}\right)}{\sqrt{2}} = y' \end{aligned} \tag{5.13}$$

The principal axes $x', y', z'$ are given by the eigenvectors of (5.12). The first eigenvector is parallel to the normal of the ZnTe wafer while the other two eigenvectors are in the plane of the wafer and rotated 45° from the $x_{lab}$ and $y_{lab}$ directions (<100> and <110> edges of the ZnTe wafer).

In the principal axis coordinate system the index ellipsoid is

$$\left(\frac{1}{n^2}-\frac{E_1 r_{41}}{2}\right)x'^2+\left(\frac{1}{n^2}+\frac{E_1 r_{41}}{2}\right)y'^2+\left(\frac{1}{n^2}\right)_3 z'^2 = 1 \qquad (5.14)$$

The electric-field induced change in the index of refraction along the principal axis can be found using the binomial approximation

$$\left(\frac{1}{n'_{\substack{x\\y}}}\right)^2 = \frac{1}{n}\left(1 \mp \frac{n^2 r_{14} E}{2}\right) \Rightarrow n'_{\substack{x\\y}} = n\left(1 \mp \frac{n^2 r_{14} E}{2}\right)^{-\frac{1}{2}} \approx n \pm \frac{n^3 r_{14} E}{4} \qquad (5.15)$$

If the probe beam is polarized along the <110> edge ( $y_{lab}$ direction) or the <100> edge ( $x_{lab}$ direction), the polarization is equally divided along the $x'$ and $y'$ directions. The change in phase between the two polarization components can be found from the difference in index of refraction

$$\Gamma(L) = \frac{2\pi L}{c}\left(n_x - n_y\right) = \frac{\omega L}{c}\frac{n^3 r_{14} E_{THz}}{2} \qquad (5.16)$$

where $\omega$ is the frequency of the probe beam, $L$ is the length of the crystal, n is the index of refraction of the probe beam, $r_{14}$ is the electro-optic coefficient, $c$ is the speed of light in vacuum, and $E_{THz}$ is the amplitude of the THz electric field.

## *Electric field parallel to the <100> edge of the ZnTe crystal*

The above procedure can be applied to the case where the THz electric field is polarized along the <100> edge. In the coordinates of the crystal axis the THz electric field is given by (5.11). The THz electric field (5.11) can be substituted into the index ellipsoid to give

$$\begin{pmatrix} x & y & z \end{pmatrix} \begin{pmatrix} \left(\frac{1}{n^2}\right) & 0 & \frac{r_{14}E}{2} \\ 0 & \left(\frac{1}{n^2}\right) & 0 \\ \frac{r_{14}E}{2} & 0 & \left(\frac{1}{n^2}\right) \end{pmatrix} \begin{pmatrix} x \\ y \\ z \end{pmatrix} = 1 \tag{5.17}$$

The eigenvectors and eigenvalues of the index ellipsoid matrix are

$$\begin{aligned} \left(\frac{1}{n^2}\right) \quad & \begin{pmatrix} 0 & 1 & 0 \end{pmatrix} = x_{lab} \\ \left(\frac{1}{n^2} - \frac{r_{14}E}{2}\right) \quad & \begin{pmatrix} \frac{-1}{\sqrt{2}} & 0 & \frac{1}{\sqrt{2}} \end{pmatrix} = -y_{lab} \\ \left(\frac{1}{n^2} + \frac{r_{14}E}{2}\right) \quad & \begin{pmatrix} \frac{1}{\sqrt{2}} & 0 & \frac{1}{\sqrt{2}} \end{pmatrix} = z_{lab} \end{aligned} \tag{5.18}$$

The equation of the index ellipsoid in the coordinate system of the principal axes is

$$\left(\frac{1}{n^2}\right)x'^2 + \left(\frac{1}{n^2} - \frac{E_1 r_{41}}{2}\right)y'^2 + \left(\frac{1}{n^2} + \frac{E_1 r_{41}}{2}\right)z'^2 = 1 \tag{5.19}$$

The principal axes $x', y', z'$ are defined by the eigenvectors. With the THz electric field parallel to the <100> edge of the ZnTe crystal ($y_{lab}$ direction) the principal axes are the same as the lab coordinate axes. If the probe beam is polarized in the $x_{lab}$ or $y_{lab}$ direction, then it will travel though the crystal along one of the principal axis. There will be no change in phase between polarization components of the probe beam. When the THz electric field is in the $y_{lab}$ direction there will be no signal if the probe beam is polarized in the $y_{lab}$ or $x_{lab}$ direction.

### *Measuring the change in retardance of the probe beam*

The THz electric fields are weak - on the order of 1 V/cm. The THz induced retardance between the two components of the probe beam along the principal axis can be very small ($< 10^{-6}$ radians). After the probe beam travels through the ZnTe crystal a balanced optical bridge is used to measure the small changes in retardance. A schematic of the optical bridge is shown in Figure 5.3. The optical bridge consists of a quarter wave plate, a polarizing beam splitter, and two photodiodes that measure the output from each arm of the beam splitter. If no THz electric field is present, the

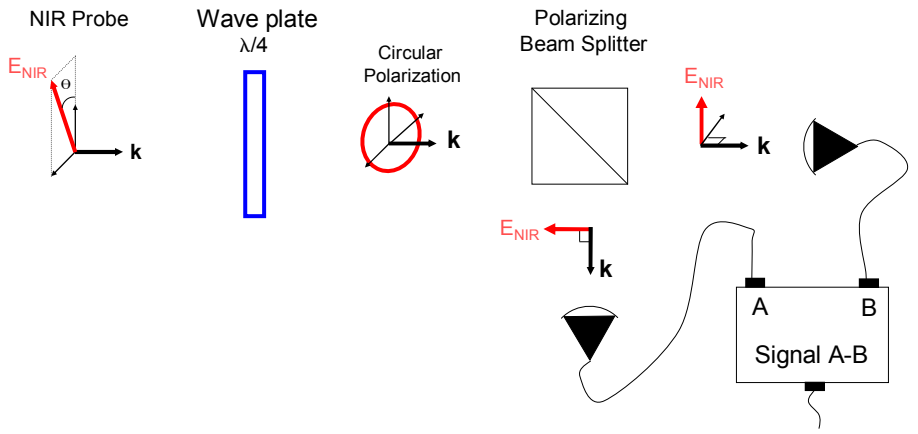


**Figure 5.3** Schematic of the polarization bridge. After traveling through the ZnTe crystal the probe beam is sent through a quarter wave plate and polarizing beamsplitter. The horizontal and vertical polarization components from the beamsplitter are measure with two identical photodiodes. When nulled the difference of the photodiode signals is proportional to the rotation of the probe beam.

linearly polarized probe beam is converted into circularly polarized light by the quarter waveplate. Circularly polarized light is as a superposition of vertical and horizontal polarized light shifted in phase by $\pi/2$. The polarizing beam splitter divides the circularly polarized light into vertical and horizontal polarization components of the probe beam. Two photodiodes record the power of the horizontal

and vertical components. The signal is the difference in output between the two photodiodes. If no THz electric field is present, the signal will be zero, and the optical bridge will be balanced.

If a THz electric field is present the linear polarized probe beam will be slightly rotated by the electro-optic effect. After the quarter wave plate the probe beam will not be completely circularly polarized. It will be elliptically polarized. There will be a small difference in the magnitude of the horizontal and vertical polarization components of the probe beam. This will produce a small difference in the output of the two photodiodes. The nulled optical bridge eliminates common mode noise from the laser. Any laser noise present in both arms will be subtracted out of the signal. Eliminating the common mode noise enables very small changes in the rotation of the probe beam ( $< 1\ \mu\Gamma$) that would not otherwise be possible.

## *Probe beam polarization state - Jones vectors*

Jones vectors can be use to calculate the power difference in the probe beams in the arms of the optical bridge. Jones vectors represent the polarization state of light as a 2x1 polarization vector. The components of the polarization vector are the magnitude and phase of light in two orthogonal directions (usually the vertical and horizontal directions). By convention polarization vectors are normalized. Polarizers, beam splitters, and retarders can all be represented as 2x2 matrices that act on the 2x1 polarization vectors. If an optical element is lossless, the matrix representing it will be unitary and preserve the normalization the polarization.

A polarizer placed before the ZnTe crystal and the optical bridge ensures that the input polarization of the probe beam is vertical. The upper (lower) component of the polarization vector will be taken to represent the vertical (horizontal) direction. The input Jones vector can by written as

$$\mathbf{P}_{\mathbf{input}} = \begin{pmatrix} 1 \\ 0 \end{pmatrix} \tag{5.20}$$

In the optical bridge, the quarter wave plate is rotated 45° to generate circularly polarized light. The principle axes of the quarter wave are in the $x_{\text{lab}} + y_{\text{lab}}$ and $x_{lab} - y_{lab}$ directions. If the THz electric field is in $y_{lab}$ direction (parallel to the <110> edge), the principal axes of the THz induced birefringence in the ZnTe wafer will also be in the $x_{lab} + y_{lab}$ and $x_{lab} - y_{lab}$ directions. Since the quarter wave plate is placed directly after the ZnTe wafer, the quarter waveplate and ZnTe wafer can be represented by the same matrix. If $\Gamma_{THz}$ is the retardance from the ZnTe crystal then the total retardance $\Gamma$ from both the ZnTe wafer and the quarter waveplate is

$$\Gamma = \Gamma_{THz} + \frac{\pi}{2} \tag{5.21}$$

The matrix for retarder with retardance $\Gamma$ and the principal axes in the $x_{\text{lab}}$ and $y_{\text{lab}}$ directions is

$$\begin{pmatrix} 1 & 0 \\ 0 & e^{i\Gamma} \end{pmatrix} \tag{5.22}$$

The principal axes of the quarter wave plate and ZnTe crystal are rotated 45° from the $x_{\text{lab}}$ and $y_{\text{lab}}$ directions and (5.22) must also be rotated by 45°. This can be

done using the 2x2 rotation matrix $\mathbf{U(\theta)}$ and noting that the rotation of a matrix $\mathbf{\Gamma}$ is given by $\mathbf{U(\theta)\Gamma U^{-1}(\theta)}$. The matrix representing the combined retardance of the quarter wave plate and ZnTe crystal is then

$$\begin{pmatrix} cos\theta & -sin\theta \\ sin\theta & cos\theta \end{pmatrix}\begin{pmatrix} 1 & 0 \\ 0 & e^{i\Gamma} \end{pmatrix}\begin{pmatrix} cos\theta & -sin\theta \\ sin\theta & cos\theta \end{pmatrix} \tag{5.23}$$

The state of the polarization after the quarter waveplate and before the polarizing beamsplitter is

$$\mathbf{U(\theta)\Gamma U^{-1}(\theta)P_{input}} = \begin{pmatrix} 1-e^{i\Gamma} \\ 1+e^{i\Gamma} \end{pmatrix} \tag{5.24}$$

Equation (5.24) can be rewritten in terms of the amplitude and phase for each component

$$\begin{pmatrix} \sqrt{\frac{1-cos(\Gamma)}{2}}\, e^{\,i\tan^{-1}\left(\frac{sin(\Gamma)}{cos(\Gamma)-1}\right)} \\ \sqrt{\frac{1+cos(\Gamma)}{2}}\, e^{\,i\tan^{-1}\left(\frac{sin(\Gamma)}{1+cos(\Gamma)}\right)} \end{pmatrix} \tag{5.25}$$

The polarizing beam splitter splits the electric field into horizontal ($x_{lab}$) and vertical ($y_{lab}$) components and the photodiodes measure the power of each component. The measured power in the horizontal *H* and vertical *V* arms of the optical bridge is

$$P_V = P\frac{1}{2}\left(1+cos(\Gamma)\right) \quad and \quad P_H = P\frac{1}{2}\left(1-cos(\Gamma)\right) \tag{5.26}$$

where $P$ is the total probe power. To find the THz induced retardance $\Gamma_{THz}$ the power in the two arms of the optical bridge is subtracted and the then divided by the sum of the power in each arm.

$$\frac{P_V - P_H}{P_V + P_H} = cos\left(\Gamma\right) = cos\left(\frac{\pi}{2} + \Gamma_{THz}\right) = sin\left(\Gamma_{THz}\right) \approx \Gamma_{THz} \tag{5.27}$$

The electric field can then be determined by substituting (5.27) into (5.16).

$$E_{THz} = \frac{2c\Gamma_{THz}}{\omega L \mathrm{n}^3 r_{14}} = \frac{2c}{\omega L \mathrm{n}^3 r_{14}} \frac{P_V - P_H}{P_V + P_H} \tag{5.28}$$

For ZnTe $r_{14}$ = 3.9 pm/V, and the index of refraction is 2.85 at 800nm. The lengths of the ZnTe crystals used in this thesis were 1mm and 2mm. For a 1mm (2mm) thick ZnTe crystal a rotation of one radian corresponds to an electric field of 27.94 KV/cm (13.97 KV/cm) and a rotation of $\pi$ radians corresponds to a rotation of 87.90 KV/cm (43.95KV/cm).

The index of ZnTe is 3.2 at THz frequencies while the index of ZnTe is 2.85 at 800nm. The group velocities of the THz pulse and femtosecond laser pulse are also not the same in the ZnTe crystal. This will cause an underestimation of the electric field for higher frequencies. In addition ZnTe has phonon absorption at THz frequencies[16]. (5.28) assumes a uniform electric field along the length of the crystal. For tight focus the electric field will not be constant.

## *Electro-optic sampling experimental setup*

The THz electro-optic sampling setup is shown in Figure 5.4. A mode locked Ti: Sapphire laser generates pulses with a time duration of 110 fs at a repetition rate of 82 MHz. The center frequency of the laser is 792nm and the output power is on the order of 650mW.

A beamsplitter divides the laser beam into a pump beam to generate THz radiation and a probe beam to electro-optically sample the THz electric field. The beamsplitter is a piece of float zone glass tilted at an angle with respect to the incoming laser beam. One side of the beamsplitter is uncoated. The other side is wedged and antireflected coated. The probe beam is reflected off the uncoated front face of the beamsplitter. The pump beam is transmitted through the beamsplitter. The wedge prevents any reflection from the back face from traveling the same path as the probe beam. The ratio of the probe beam power to the pump beam power is on the order of 10:90 or 20:80 and can be changed by varying the angle of beamsplitter's tilt.

After the beamsplitter the pump beams is modulated by a chopper. It is desirably to modulate the pump beam at a frequency as high as possible to reduce 1/f noise. However, the vibrations and air currents from the chopper were found to introduce noise into the measurement. This noise was observed to increase as the chopper rotation speed was increased. To lower the rotational speed of the chopper a 100 slot chopper wheel was used. The modulation frequency of the chopper was typically on the order of 2.3 KHz.

A half waveplate placed allows the polarization of the pump beam to be varied. For THz radiation produced by a material with a nonlinear susceptibility, the intensity and polarization of the radiation depends on the polarization of the pump beam. The pump beam is directed to strike a THz emitter which produces THz radiation. Chapter 6 discusses the generation of THz radiation from semiconductors using

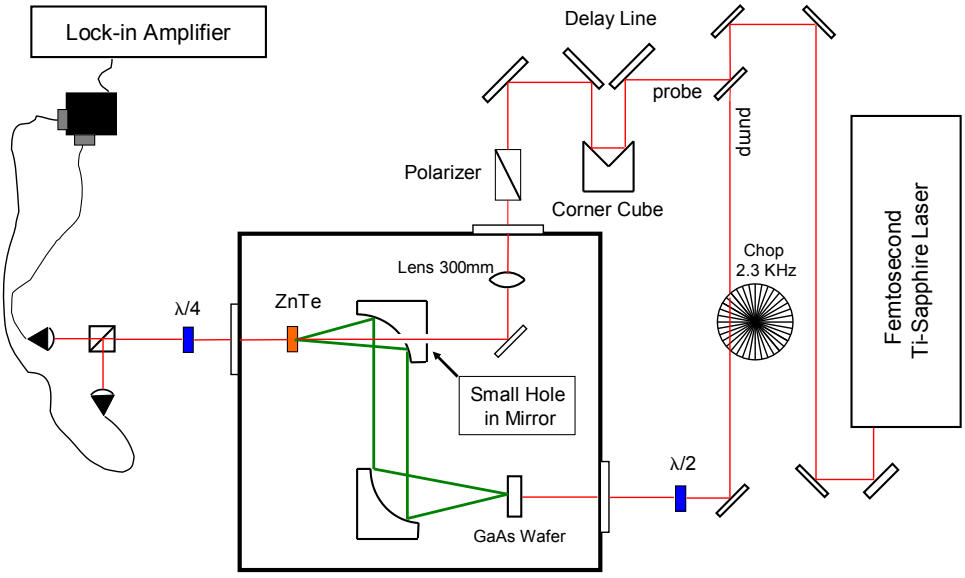


**Figure 5.4** Schematic of the experimental setup used for free space electro-optic sampling.

femtosecond lasers. Since the THz is produced by the pump beam, the emitted THz will be modulated by the chopper.

The THz radiation is collected and collimated with an off-axis parabolic mirror having a focal length of 4.8 inches and a diameter of 3 inches. An identical parabolic mirror refocuses the THz radiation onto the ZnTe sensor crystal. The ZnTe sensor is

in a rotating mount. The <110> direction of the ZnTe crystal can be rotated to detect either the vertical or horizontal component of the THz electric field.

A piece of polystyrene foam or high density polyethylene is placed between the two parabolic mirrors. This prevents any pump beam light from traveling to the ZnTe sensor.

The probe beam is delayed in time from the pump beam by a retro-reflector mounted on a translation stage. The stage is actuated by a screw with a motor controlled by a computer. The probe beam is sent through Glan-Thompson polarizer to ensure it is vertically polarized. The probe beam travels to the ZnTe sensor through a small hole drilled in the focusing parabolic mirror. A 300mm achromatic lens placed before the parabolic mirror focuses the probe beam on the ZnTe sensor. The lens ensures the probe beam only samples the region of maximum field at the center of the THz focus. The probe beam travels through the ZnTe crystal collinearly with the THz radiation. If the probe pulse overlaps in time with a portion of the THz electric field, the ZnTe crystal will become birefringent and rotate the polarization of the probe beam. The probe beam's rotation is then measured using the balanced optical bridge.

After the probe travels through the ZnTe crystal the measurement ceases to be time-resolved. At this point the probe beam can be thought as being quasi-continuous. The photodiodes are not fast enough to detect the 82 MHz pulse train of the laser.

After the ZnTe wafer, the probe beam travels through a quarter wave plate. It is then split into horizontal and vertical polarization components by a beamsplitting polarizer. The horizontal and vertically polarized beams are coupled into two optical fibers. The optical fibers send the light to two identical photodetectors. The signals from the photodetectors are subtracted and sent to a lock in amplifier. The reference for the lock-in amplifier is the frequency from the chopper. The probe beam is not chopped or modulated. The output of the lock-in measures changes in signal caused by the THz radiation. The lock-in's output is proportional to the difference in power between the two arms of the photodiode $P_V - P_H$ in equation (5.28) which is also proportional to the rotation of the probe beam and the value of the THz electric field.

### *Converting the signal to radians*

Before a measurement is taken, one arm of the optical bridge is blocked, and the power in that arm is recorded. The power in the other arm is approximately the same. In this way $P_V + P_H$ can be found. The lock-in measures the root mean square (RMS) of the signal $P_V - P_H$ at the modulated chopper frequency. To convert to radians the signal $P_V - P_H$ must be divided by the sum of the power in each arm $P_V + P_H$.

However the signal is the root mean square of a modulated quantity while the sum of the power in each arm is a DC quantity. The signal must first be converted from a RMS quantity to an equivalent DC quantity, before dividing the signal $P_V - P_H$ from the sum of the powers in the two arms $P_V + P_H$.

The width of the chopper blade is on the order of the beam size. The modulated THz radiation will not be a square wave function. The conversion factor between the lock-in's RMS signal and its equivalent DC value must be found experimentally. This was done by attenuating the pump beam and recording the chopped output on both an oscilloscope and a lock-in. (The chopper wheel was adjusted for maximum output on the lock-in amplifier.) The conversion factor between the RMS signal and equivalent DC signal was found to be 3.64. The conversion to radians can then be found using the expression

$$\Gamma = \frac{P_V - P_H}{P_V + P_H} = \frac{A \times R.M.S\left(P_V - P_H\right)}{D.C.\left(P_V + P_H\right)} \tag{5.29}$$

where A is the conversion factor.

## *Sources of noise*

There are several sources of noise in the THz electro-optic sampling setup. Noise sources include laser noise, shot noise, Johnson noise, and 1/f or flicker noise. Laser noise can be minimized by the nulling the optical bridge. However, the optical bridge can never be completely nulled. At DC frequencies the optical bridge can be nulled to one part in $10^4$. This implies common noise in both arms of the optical bridge will be reduced by at least $10^4$. Laser noise will always be present even when the bridge is balanced, and can be significant when measuring small rotations of the probe beam.

Johnson arises from voltage fluctuations across a resistor. For a resistance R and temperature T the Johnson noise is

$$\Delta V_{Johnson} = \sqrt{4kTRB} \tag{5.30}$$

where k is Boltzmann's constant, R is the value of the resistor, T is the temperature, and B is the bandwidth. Johnson noise can be minimized by choosing an appropriate value of the resistor.

Flicker noise is characterized by a 1/f spectral response and is dominant at low frequencies. It can be avoided by chopping the pump beam at high frequencies. The noise from the photodiodes (measured on a spectrum analyzer) flattens past approximately 2 KHz. The chopper frequency was set between 2.3 and 2.5 KHz. If the pump beam is chopped at too high of a frequency, noise will be introduced into the measurements from air currents and mechanical vibrations.

Shot noise is the noise in the current due to the quantization of electronic charge. The shot noise for a current *I*, and measurement bandwidth *B* is

$$\Delta I = \sqrt{2eIB} \tag{5.31}$$

In practice the shot noise will be larger then Johnson noise. If the laser noise and flicker noise can be neglected then shot noise will be the dominant noise of the measurement.

The noise of the rotation of the probe beam ($\Delta\Gamma_{shot}$) due to shot noise can be found using equations (5.27) and (5.31). If the current in each arm of the optical

bridge denoted as $I_V$ and $I_H$ and the current is proportional to the incident power, the rotational noise is

$$\Delta\Gamma_{shot} = \frac{\Delta I_H - \Delta I_V}{I_H + I_V} = A\sqrt{\frac{e}{I_{H\,or\,V}}} \tag{5.32}$$

It has been assumed that the shot noise from each photodiode is uncorrelated. The shot noise increases with increasing probe power, but the rotational noise ($\Delta\Gamma_{shot}$) increases with probe power. By increasing the probe power the shot noise contribution of the rotational noise ($\Delta\Gamma_{shot}$) decreases.

## *Photodiode detector characterization*

In order to decrease the shot noise contribution a higher probe power can be used. However for high probe power the photodiodes will saturate and their response will no longer be linear with power. The saturation power of the photodiodes will be proportional to the area of the photodiodes. Two identical photodiodes with an area of 613 $mm^2$ were used to measure the probe beam in each arm of the optical bridge.

Two fiber optic cables brought the probe beams from the experiment to the photodiodes. An aluminum box was machined to enclose the photodiodes. The ends of the two optical fibers were screwed into fiber couplers on the outside of the Al box. The angle of the diffracted beam emitted from the end of the fiber was found by looking up the numerical aperture of the fiber. The photodiodes were placed at a distance from the ends of the fiber, so that the diverging light was spread out over the entire photodiode. To prevent in light one arm of the optical bridge being recorded

by the photodiode in the other arm, the photodiodes were placed in separate chambers walled off from one and other.

The current was converted into a voltage using an OPA637 operational amplifier as a transimpedance amplifier. A schematic of the circuit is shown in Figure 5.5.

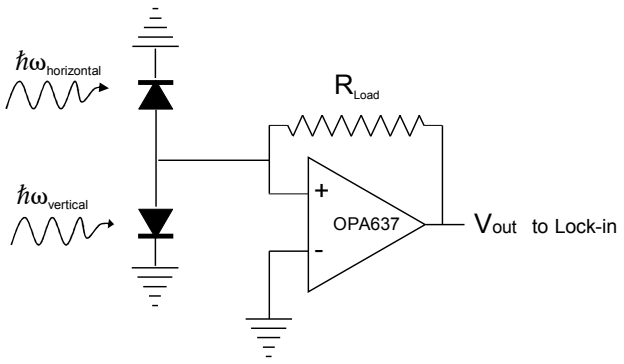


**Figure 5.5** Balanced photodiode circuit.

The feedback resistor of the op amp could be switch between 200Ω, 2KΩ, and 20KΩ. The response of the diodes was found by blocking one arm of the optical bridge and measuring the output voltage of the detector versus the incident power. The power was measured by unscrewing the fiber from the detector and using a power meter. The photocurrent was found by dividing the voltage by the value of the feedback resistor. The responsivity of the left and right photodiodes used in the optical bride of the electro-optics sampling setup is shown in Figure 5.6.

For both diodes the photoresponse was .52 A/W with a nearly negligible y-intercept. For probe beam powers greater then 20 mW the response of the photodiodes saturated. The same behavior was found with the 200 and 2 KΩ feedback resistors. This implies the saturation was due to the photodiodes and not

caused by output current saturation of the op-amp. Typically 10mW of probe beam power was incident on each photodiode.

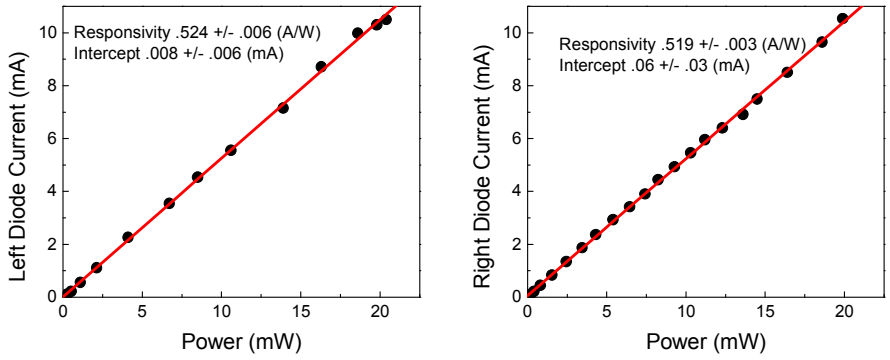


**Figure 5.6** The measured responsivity of the two photodiodes in the polarization bridge.

## *Measurement of the system noise floor*

The pump beam was blocked and the noise from the balanced photodiodes was measured with the lock-in and a spectrum analyzer. Instead of directly measuring the noise with the lock-in, the noise was calculated from recorded data. It was found that there was added noise when the lock-in was remotely controlled by the computer. For the following noise measurements the lock-in signal was measured by a DMM (digital multimeter) which was in turn controlled by the computer. The roll-off of the lock-in was set to 12dB. The wait time between measurements was set to seven times lock-in's time constant. The equivalent noise bandwidth at 12dB is 1/8T where T is the time constant.

The results of the noise measurements are show in Figure 5.7. At a time constant of 300ms the RMS value of the noise found to be .37 $\mu$V which corresponds to a rotational noise of .11$\mu\Gamma/\sqrt{Hz}$ . The noise output of the photodiodes was also measured to be .39 $\mu V/\sqrt{Hz}$ with a spectrum analyzer. This corresponds to a rotational noise of .07 $\mu\Gamma/\sqrt{Hz}$ which is close to the noise obtained by the lock-in. The shot noise limited probe power can be calculated to be .02$\mu\Gamma/\sqrt{Hz}$ .

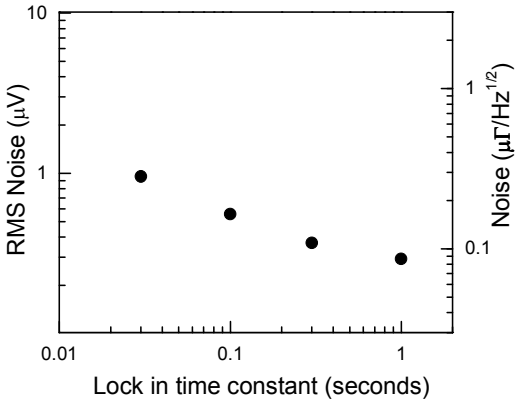


**Figure 5.7** The root mean square noise of the signal measured with the pump beam blocked.

The noise of electro-optic setup is not limited by shot noise. Other noise sources include the Johnson noise from load resistor of the transimpedance amplifier in the photodiode circuit. The calculated Johnson noise value from a 2KΩ resistor is .006 $\mu V/\sqrt{Hz}$ . This is an order of magnitude below the noise measured with the spectrum analyzer. After 2 KHz the noise spectrum is flat with frequency which indicates flicker noise or 1/f noise does not make a significant contribution to the total noise. The most probable cause of the excess noise is laser noise. The laser noise is significantly reduced by the balanced optical bridge. However the optical bridge can

only be nulled to one part in $10^4$ and will not eliminate all laser noise from the signal. The optical table of the Ti: Sapphire laser is not on air. In the lab there is also a running hepa-filter above the experiment attached to the optical table and a chiller to cool the Ti: Sapphire optics. Both could be sources of mechanical vibrations which could destabilize the laser. The power output of the Ti: Sapphire is also found drift with time and must be periodically aligned realigned. The most like source of the excess noise is from laser noise.

### *Water vapor lines - purging*

Water molecules have rotational absorption lines that strongly absorb THz radiation. THz radiation will experience loss when traveling through air from water vapor absorption. In order to eliminate the water vapor absorption lines a vacuum box was built. The vacuum box surrounded the portion of the experimental setup where the THz radiation traveled from its creation at the emitter to the ZnTe sensor crystal. It was found that either purging with dry Nitrogen or evacuating the experiment removed the absorption lines and increased the strength of the signal. No difference was found between purging and evacuating the vacuum box. Consequently, most of the data was taken with the boxed purged since no roughing pump was needed.

Figure 5.8 shows the measured THz signal with the vacuum box evacuated and the lid of the vacuum box open. The THz pulse created at the emitter consists of a one cycle pulse and has broad bandwidth. (Generation of THz radiation is described

in Chapter 6) The measured electric field when the vacuum box is evacuated is shown on the right hand side of Figure 5.8. When the box is open the signal is

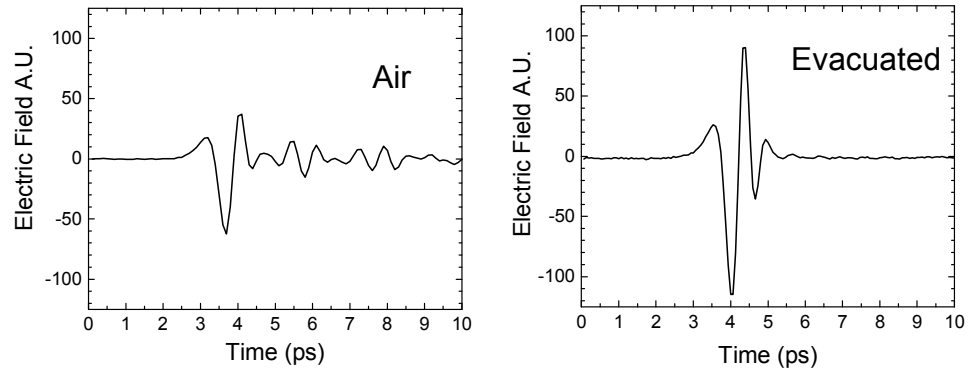


**Figure 5.8** THz electric field signal. Left: purge box opened and exposed to air. Right: vacuum box evacuated

reduced and a ringing occurs behind the main pulse cycle. The ringing is caused by the dispersion introduced by absorption from the water vapor.

# 6 Generation of THz from femtosecond laser pulses

THz radiation can be generated when a femtosecond laser is incident on a semiconductor wafer. The THz radiation produced is typically a one or two cycle electromagnetic pulse. The spectral width of such a short pulse will be very broad - on the same order of the pulse's central frequency. There are three widely used physical mechanisms used to generate THz radiation from femtosecond lasers; optical rectification, acceleration of photo-generated carriers, and diffusion of photo-generated carriers.

Optical rectification generates THz radiation from a nonlinear polarization. Different optical frequencies are mixed by the nonlinear polarization. Electromagnetic radiation is generated at the sum and difference of the optical frequencies. If the spectrum of the laser spans a THz, some difference frequencies will be at THz frequencies. The high instantaneous peak power of the femtosecond laser pulses increases the efficiency of the mixing.

THz radiation can also be produced from the acceleration of photo generated carries across an electric field. A femtosecond laser creates a non equilibrium distribution of electron hole pairs. The photo generated charge is then accelerated either by a built in electric field or an externally applied electric field. The accelerating charge generates a current pulse. The turn on time of the current pulse is

the time duration of the femtosecond laser - typically 100 fs which is less then the period of the THz electromagnetic fields. The current pulse will have THz frequency components and radiate THz electromagnetic fields.

Another method to generate THz radiation from a semiconductor is the photo-Dember effect. A femtosecond laser generates a non equilibrium distribution of electron-hole pairs at the surface of a semiconductor. The semiconductor's surface forms a barrier to diffusion. If the electron and hole mobilities are different, the lighter carriers (electrons) will diffuse away from surface faster then the heavier carriers (holes). A polarization field will be set up between carrier distributions on an ultrafast time scale. If the diffusion is fast enough the polarization field will contain THz frequencies and generate THz radiation. InAs is often used to produce THz radiation using the photo-Dember effect. InAs has a light electron mass ($.023m_e$) and a high electron mobility of $4 \cdot 10^4$ $cm^2$ $V^{-1}s$ while the hole mobility in InAs is only $5 \cdot 10^2$ $cm^2$ $V^{-1}s$. However, InAs wafers are doped, and opaque to THz radiation. Generated THz radiation from InAs wafers must be collected using a reflection geometry. InAs is not a candidate to make THz photonic crystals out of, since a photonic crystal needs to be transparent. For this reason generated THz radiation via the photo-Dember effect in InAs will not be discussed further.

GaAs is an excellent material to make photonic crystals out of as discussed in Chapter 1. THz radiation can also be generated directly inside GaAs using either optical rectification, or photo generated charges acceleration across electric fields.

THz GaAs photonic crystals can then be probe with THz radiation produced inside the photonic crystals.

For all methods of THz generation from a semiconductor and a femtosecond laser, the phase of the THz pulses will be independent of the phase of the femtosecond laser. Successive THz pulses will be identical to each other and locked in time with the femtosecond laser pulses which created them. This enables the generated THz electric fields to be measure using free space electro-optic sampling (discussed in Chapter 5).

## *Optical rectification*

A material's polarization in a strong electric field will have a nonlinear response. In the perturbative regime the polarization may be written as a power series expansion about the electric field. The electric field and polarization are vectors and the coefficients of the power series expansion of the polarization are tensors having a rank that corresponds to the order of the expansion. While the vector and tensor aspect of the power expansion is important for calculations, it is not necessary for a general understanding of optical rectification. In one dimension the electric field and polarization are scalars and the power expansion of the polarization may be written as

$$\begin{aligned} P(t) &= \chi^1 E(t) + \chi^2 E^2(t) + \chi^3 E^3(t) + \ldots \\ P^1(t) &\equiv \chi^1 E(t) \\ P^2(t) &\equiv \chi^2 E^2(t) \\ P^3(t) &\equiv \chi^3 E^3(t) \end{aligned} \tag{6.1}$$

If the electric field is $E\cos(\omega t - kx)$ then the 2nd order polarization term is

$$P^2(t) = \frac{\chi E^2}{2}\left(\cos(2\omega t - 2kx) + 1\right) \tag{6.2}$$

For a single frequency, the 2nd order polarization term has a frequency component at twice the fundamental frequency and a DC term. The generation of a static field from an oscillating field is referred to as rectification.

If two different frequencies are present $\omega_1$, and $\omega_2$, with amplitudes $E_1$ and $E_2$, the 2nd order polarization term is

$$\begin{aligned} P^2 = {} & \frac{\chi^2 {E_1}^2}{2}\left(\cos(2\omega_1 t - 2k_1 x) + 1\right) + \frac{\chi^2 {E_2}^2}{2}\left(\cos(2\omega_2 t - 2k_2 x) + 1\right) \\ & + \chi^2 E_1 E_2\left(\cos((\omega_2 - \omega_1)t - (k_2 - k_1)x) + \cos((\omega_2 + \omega_1)t - (k_2 + k_1)x)\right) \end{aligned} \tag{6.3}$$

The nonlinearity mixes the two frequencies generating sum and difference frequencies at $\omega_1 + \omega_2$ and $\omega_1 - \omega_2$. The sum and difference frequencies correspond to the DC and 2nd harmonic frequency components in equation (6.2).

A femtosecond optical pulse will have a broad spectrum composed of many optical frequencies. The 2nd order susceptibility term in (6.1) will mix the femtosecond laser pulses' frequency components. This will produce 2nd order polarization terms oscillating at sum and difference frequencies of the laser pulse's spectrum. The oscillating polarizations will be sources of electromagnetic radiation.

The spectrum of the Ti: Sapphire laser used in this thesis is shown in Figure 6.1. The width of the spectrum spans several THz with a FWHM of 5 THz. When the

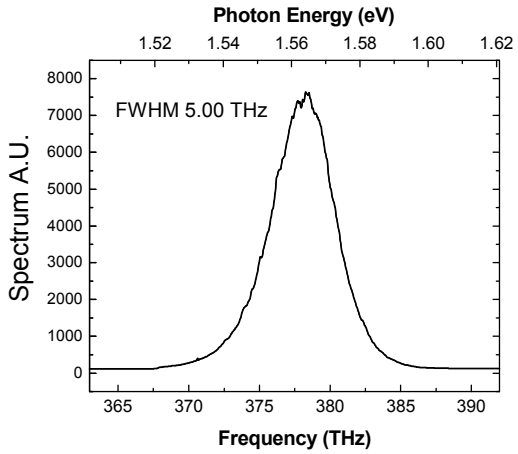


**Figure 6.1** The femtosecond laser's power spectrum. The center of the spectrum is 792.5nm.

optical frequency components are mixed some of the difference frequencies will be at THz frequencies and emit THz radiation.

## *Origin of 2nd order nonlinear susceptibility*

Not all materials will have a 2nd order susceptibility. In order to understand why, one must first understand the origin of medium's linear and nonlinear polarization response.

If an electron is bond to an atom, an electric field will displace the electron cloud from equilibrium creating a polarization. The atom's potential can be expanded in a Taylor series expansion about its equilibrium point. In the regime of linear optics only the lowest order parabolic term of the expansion is kept. All of the higher order terms are neglected. This is usually an excellent approximation. An external electric field will typically be very small compared to the inner atomic electric field. Any

external field will displace an electron cloud from its equilibrium position by a very small amount.

A parabolic potential is a spring-like potential. When the electron cloud is displaced the restoring force will be proportional to the electron cloud's displacement. This implies the atom's polarization will have a linear response to an external electric field.

In the regime of nonlinear optics the electric field is high enough for the parabolic approximation of the electron's potential to no longer be valid. Higher order terms must be kept in the series expansion of the potential. The 2nd and 3rd order terms in the series expansion have the form $k_2x^3$ and $k_3x^4$ ($x$ is the displacement from equilibrium and $k$ is the spring constant). These terms of the atom's potential produce the 2nd and 3rd order polarization terms $P^2$ and $P^3$ in (6.1).

The even terms ($P^2$, $P^4$…) of (6.1) arise from antisymmetric potentials while the odd terms ($P^1$, $P^3$…) of (6.1) arise from symmetric potentials. Many materials will be isotropic and the atom's potential will be completely symmetric. The power series expansion of their polarization will not have any even terms. In three dimensions the electron's potential must lack inversion symmetry for even order terms to appear. This lack of symmetry may occur in crystals where an atom's potential will be strongly affected by the surrounding atoms.

A material with a 2nd order nonlinearity will often have a non isotropic response. An applied electric field in one direction may generate a 2nd order polarization in an

orthogonal direction. To calculate the direction of the 2nd order polarization for a given direction of the electric field, equation (6.1) must be written in terms of vectors and tensors.

## *Other higher order nonlinear susceptibilities*

The third order susceptibility term will mix three frequency components $\omega_1$, $\omega_2$, $\omega_3$ and generate frequencies of the form $\omega_1$+/- $\omega_2$ +/- $\omega_3$. Only frequencies at the fundamental and 3rd harmonic third will be generated by a third order susceptibility.

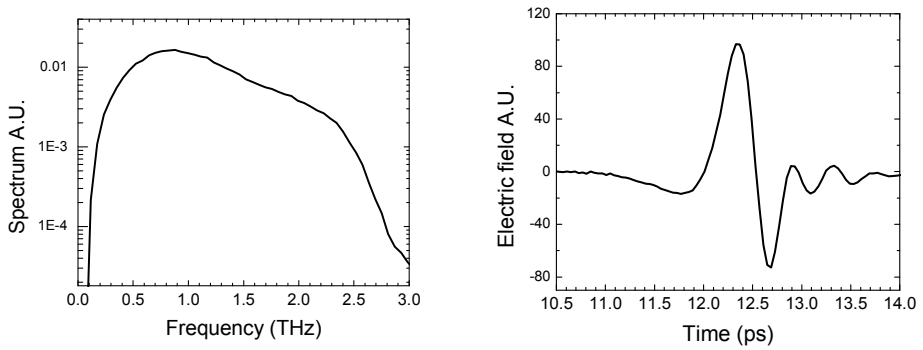


**Figure 6.2** Power spectrum (right) and electric field (left) of a THz pulse generated by optical rectification in <111> GaAs

No THz frequency components will be generated by a 3rd order susceptibility.

The fourth order polarization will produce THz difference frequency components. However in general $\chi^1 \gg \chi^2 \gg \chi^3 \gg \chi^4$ and the electric field from the laser pulse will be too weak to produce a significant $P^4$ contribution to the generated THz.

## *Optical rectification in GaAs and ZnTe*

Optical rectification can be used to generate THz radiation from GaAs and ZnTe crystals. Both are zinc blende crystals and have the same crystal symmetries. THz via optical rectification will be produced from a femtosecond laser from incident on <110> and <111> zinc blende crystals, but no THz radiation will be produced by <100> zinc blende crystals.

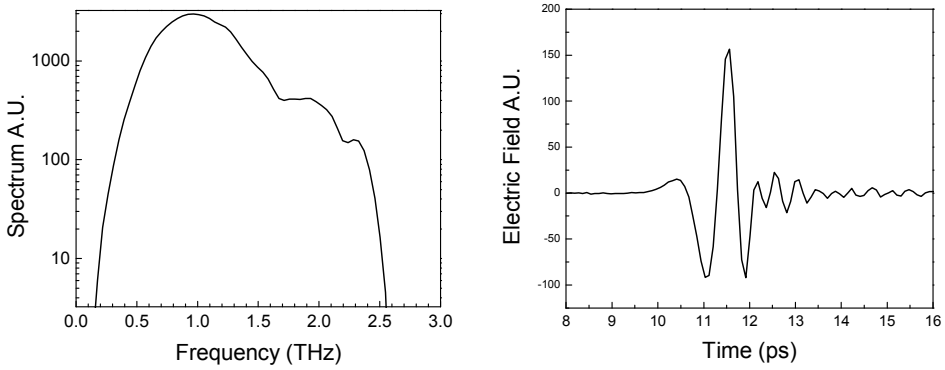


**Figure 6.3** Power spectrum (left) and electric field (right) from a 2mm ZnTe crystal.

For GaAs the nonlinear susceptibility is enhanced when the laser is tuned below the bandgap[17]. The power of the generated THz radiation will be greater for a laser tuned above the bandgap then for a laser tuned below the band gap photon[18] - in spite of strong absorption below the bandgap. Figure 6.2 shows the THz electric field and spectrum when a femtosecond laser beam is incident on <111> GaAs wafer. The laser photon energy is 1.56eV while the bandgap of GaAs is 1.42eV. The femtosecond laser is strongly absorbed by the GaAs. But optical rectification still occurs due to the bandgap enhancement of the susceptibility.

The bandgap of ZnTe is 2.39eV. In contrast to GaAs the laser frequency is below the bandgap of ZnTe and the ZnTe wafer will be transparent. This allows the femtosecond laser beam to continuously create THz radiation as it travels through the crystal. The group velocity of a THz pulses and the laser beam are nearly matched at a wavelength of 822nm. The emitted THz power will be proportional to the length of the crystal. In general the THz power produced by a ZnTe wafer will be greater then the power produced by a GaAs wafer.

The group velocities of the THz pulse and optical pulse are not equal. If the length of the ZnTe crystal is too large, THz created at the front face will destructively interfere with THz created at the back face. This will lead to an attenuation of the signal. Figure 6.3 shows the THz emission from a <110> ZnTe wafer used as an emitter. In Figure 6.3 the laser beam was focused on the sample and the dip near 1.7 THz is believed to correspond to phonon absorption[19]. (The dip near 2.2 THz is absorption from the HDPE used to block the pump beam and transmit the THz beam.)

## *Power dependence of optical rectification*

For optical rectification the THz electric field is proportional to the 2$^{nd}$ order polarization term $P^2$ in equation (6.1) which is proportional to the square of the optical electric field. The power of the generated THz pulse will scale as the square of the input power of the femtosecond laser pulse. For efficient frequency conversion to take place high peak values of the optical electric field are needed. For the Ti: Sapphire laser used in this thesis the average per pulse power is on the order of 8 nJ

per pulse. Pulses from a regenerative amplifier can have energies of over 1 $\mu$J per pulse at repetition rates of over 100 KHz and will produce more THz power from optical rectification then unamplified systems.

The dependence on the THz power on the pump power is shown in Figure 6.4. The femtosecond laser beam was unfocused and incident normal to the <111> GaAs surface. Then peak power of the THz electric field is plotted versus the incident pump power of the femtosecond laser. A parabolic fit to the data is also shown in Figure 6.4.

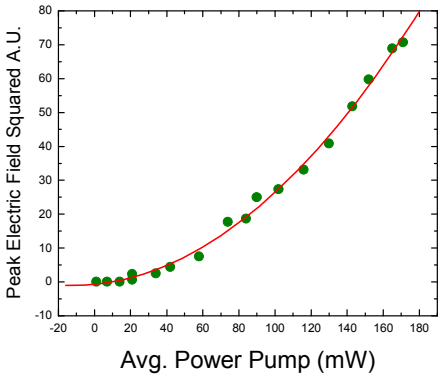


**Figure 6.4** Power dependence of the emitted THz from a <111> GaAs waver versus input laser power**.**

## *Polarization dependence of optical rectification*

The polarization of the generated THz depends in a complicated manner on the orientation of the crystal and the polarization of the femtosecond laser. If $\theta$ is the angle between the <110> direction of the crystal and the laser beams polarization,

then for a <111> zinc blende crystal the 2nd order polarization term that produces THz radiation is

$$\begin{pmatrix} P^2_{xTHz} \\ P^2_{yTHz} \\ P^2_{zTHz} \end{pmatrix} = \begin{pmatrix} -\frac{\chi^2}{2}\sqrt{\frac{2}{3}}\ E^2_{NIR}\sin 2\theta \\ -\frac{\chi^2}{2}\sqrt{\frac{2}{3}}E^2_{NIR}\cos 2\theta \\ -\frac{\chi^2}{2}\sqrt{\frac{1}{3}}E^2_{NIR} \end{pmatrix} \tag{6.4}$$

Equation (6.4) is derived in appendix B. The z-direction is normal to the plane of the wafer and is also the direction of prorogation for the pump laser beam and the THz beam. The z-component of the nonlinear polarization $P^2_{zTHz}$ is parallel to the

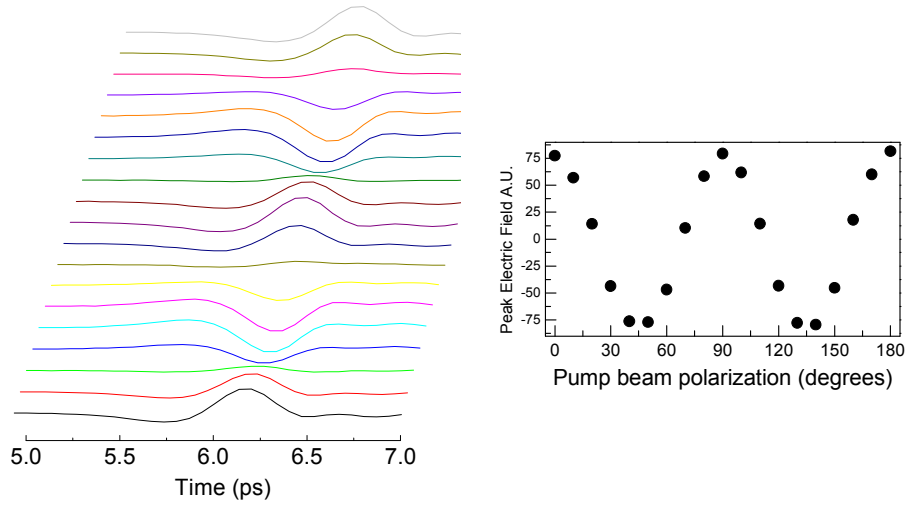


**Figure 6.5** Polarization dependence of the THz electric field on the pump beam polarization for <111> GaAs. Left: Emitted THz signal from rotating the pump beam with a half wave plate. Right: Peak THz electric field versus half waveplate rotation.

direction of the emitted THz radiation. Oscillating dipoles do not radiate along their direction of oscillation, consequently no THz radiation will be emitted by $P_{zTHz}^2$ in the forward direction.

Figure 6.5 shows the pump beam polarization dependence of the emitted THz electric from a <111> GaAs. The polarization of the pump beam is rotated 180° by a half-wave plate and the position of the <111> GaAs crystal is kept constant throughout the measurement. The ZnTe electro-optic sensor is a polarized detector - only the component of the THz electric field along the <110> edge of the ZnTe sensor is detected.

The maximum value of the measured THz electric field is plotted as a function of the pump beam's angle of polarization in Figure 6.5. The maximum THz electric field varies sinusoidally and goes through two periods which is consistent with equation (6.4)

In Figure 6.6 the pump beam's polarization is fixed and the <111> GaAs is rotated 360° such that the plane of the <111> GaAs wafer is always normal to the pump beam. The component of the THz electric field along the ZnTe sensor's <110> edge also varies sinusoidally as the <111> GaAs wafer is rotated about the axis of the pump beam in Figure 6.6. However, the period of the oscillation of the peak is 120°. This is in contrast to Figure 6.5 where the period of the measured peak field was 180°. Rotating the <111> GaAs wafer is equivalent to keeping the GaAs wafer fixed and rotating both the pump beam polarization and the ZnTe senor simultaneously.

This is different then just rotating the pump beam polarization. For a 360° rotation of a <111> GaAs wafer the peak detected THz electric field can be shown to undergo 3 periods. (The derivation is contained in Appendix B).

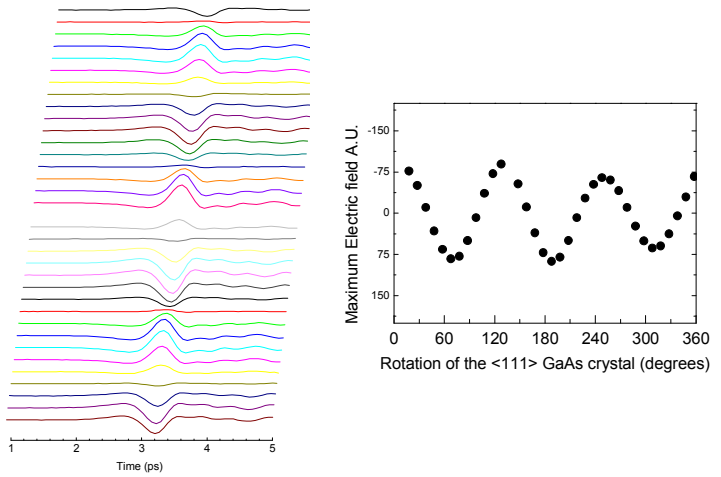


**Figure 6.6** Polarization dependence of the THz electric field on the crystal orientation for <111> GaAs. The pump beam polarization is held fixed. Left: Emitted THz field as the <111> GaAs crystal is rotated about the azimuth angle. Right: Peak THz electric field versus crystal rotation.

## *Plasma oscillations*

In the Drude model electrons (holes) ionized from donor (acceptor) atoms are responsible for a material's conductivity. The ionized carries are unbound and free to move about in a background of fixed charge - the donor or acceptor atoms. The ionized carriers may be thought of as a dilute plasma. If the ensemble of charged carries is displaced from equilibrium, they will under go collective oscillations. The resonant frequency of the oscillations is the plasma frequency. For a material where

$n$ is the density of the charge carriers, $e$ is the charge of a carrier, $\epsilon$ is the permittivity of the material, and $m^*$ is the reduced mass of the carriers, the plasma frequency $\omega_p$ is

$$\omega_{plasma} = \sqrt{\frac{ne^2}{\varepsilon m^*}} \tag{6.5}$$

The motion of the collective oscillation of carriers will be heavily damped by scattering in the semiconductor, and the resonance of the plasma will be very broad. For metals with a charge density on the order of $10^{22}$ $cm^{-3}$ the plasma frequency is at ultraviolet frequencies. However for semiconductors, the density of mobile charge carriers is much less. The charge density can also be controlled by varying the doping of the semiconductor. For GaAs with an electron density of $10^{16}$ $cm^{-3}$ the plasma frequency is .96 THz.

## *THz radiation from plasma oscillations*

Plasma oscillations in a doped epilayer of a GaAs semi-insulating wafer can be used to generate THz radiation[20]. If the plasma is displaced, the plasma will oscillate about its equilibrium position. The oscillating charge will radiate electromagnetic radiation at the frequency of oscillation - which is the plasma frequency. The displaced plasma will undergo one or two cycles of oscillations (due to the heavy damping) and produce a one or two cycle electromagnetic pulse.

In order for plasma oscillations to occur the plasma must be given a short 'kick' to knock the plasma out of equilibrium. This 'kick' is provided by photo-generated carriers created by the femtosecond laser that are accelerated across the semiconductor's surface depletion field.

The depletion field in n-doped GaAs is created by surface states that trap charge from the bulk. Near the surface there will be a depletion of conduction band electrons. The positive donor atoms and the trapped surface charge create a strong depletion field in the semiconductor. The strength of the built in depletion field and the length of the depletion zone both depend on the doping of the semiconductor and are given by

$$L_{depletion} = \sqrt{\frac{2\varepsilon\phi}{ne}}$$
$$E_{depletion} = \frac{ne}{2\varepsilon}\left(L_{depletion} - x\right) \tag{6.6}$$

where $n$ is the density of electron, $\varphi$ is a built in potential (.7eV for GaAs), m* is the reduced mass $\epsilon$ is the permittivity and $e$ is the charge of an electron. For GaAs with a doping density of $10^{16}$ $cm^{-3}$ the length of the depletion zone will be approximately 317 nm and the strength of the depletion field will be on the order of $10^4$ V/cm. The extinction coefficient of GaAs at 795nm is .087[21]. The corresponding absorption coefficient is 1.37 $\mu m^{-1}$. This implies that 63% (1-1/e) of the laser beam will be absorbed within 730 nm of the surface. A significant fraction of the photo generated carriers will be created in the depletion zone. They will be accelerated by the depletion field and give the bulk electrons in the epilayer a 'kick'. This will initiate plasma oscillations in the bulk epilayer which will radiate electromagnetic waves into free space.

### *Direction of emitted THz radiation*

The depletion field is always normal to the semiconductor surface. The emitting plasma dipoles will also be normal to the surface. If the laser illuminates the wafer at normal incidence, no THz radiation will propagate in the forward direction. (A dipole's radiation pattern will be zero in the direction parallel to the dipole.) If the wafer is tilted with respect to the pump beam, the dipoles will no longer be parallel with the laser beam and THz will be radiated in the forward direction.

When the wafer is tilted the dipoles across the wafer will be excited by the pump beam at different times. This is analogous to a light ray striking a tilted dielectric

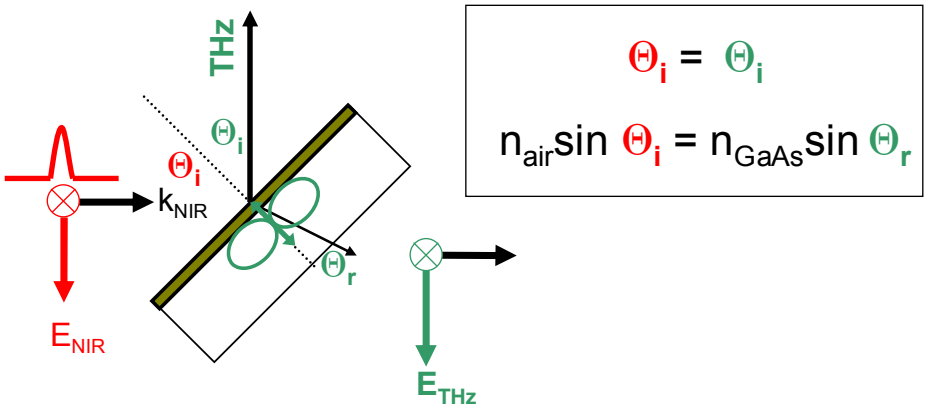


**Figure 6.7** The generated THz beams obey a Snell-like law.

slab. The angle of the refracted ray is prescribed by Snell's law and the angle of refraction is equal to the angle of incidence[22]. The direction of the refracted THz ray will obey Snell's law as shown in Figure 6.7. The angle of the reflected THz ray will be equal to the laser's angle of incidence.

As the wafer is tilted away from the normal defined by the pump beam the emitted THz will increase as the refracted ray will intersect with a stronger portion of the dipole's radiation pattern[23]. The peak THz electric field versus the angle of the wafer's tilt is shown in Figure 6.8. In Figure 6.8 the pump beam's polarization lies in the plane of incidence (horizontal polarization). The angle of the wafer's tilt is often set at Brewster's angle to maximize the absorption of the pump beam. The index of GaAs at 800nm is 3.7 [24], and it has a Brewster's angle of 75°.

Emitted electromagnetic radiation from an oscillating dipole will have the same polarization as the dipole. If the wafer is tilted about the vertical axis, the polarization of the THz will always be in the horizontal direction regardless of the pump beam's polarization.

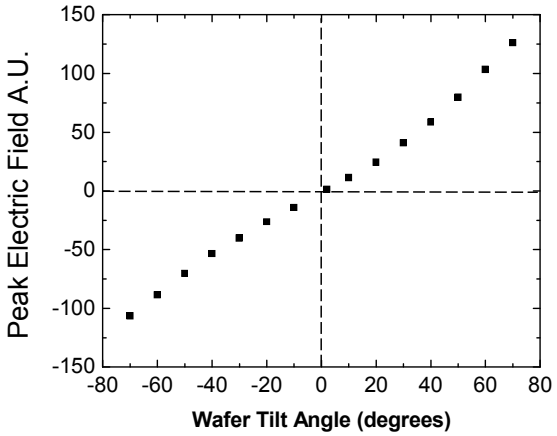


**Figure 6.8** Peak THz electric field versus the angle of tilt of the GaAs wafer with respect to the pump laser beam.

The peak THz electric field emitted from a GaAs wafer with a doped epilayer as a function of the wafer's tilt angle with respect to the pump beam shown in Figure 6.9. The GaAs wafer is a <100> semi-insulating wafer with a 2$\mu$m n-doped (2 x $10^{16}$ $cm^{-3}$) epilayer at the surface. No THz radiation is emitted at normal incidence, and

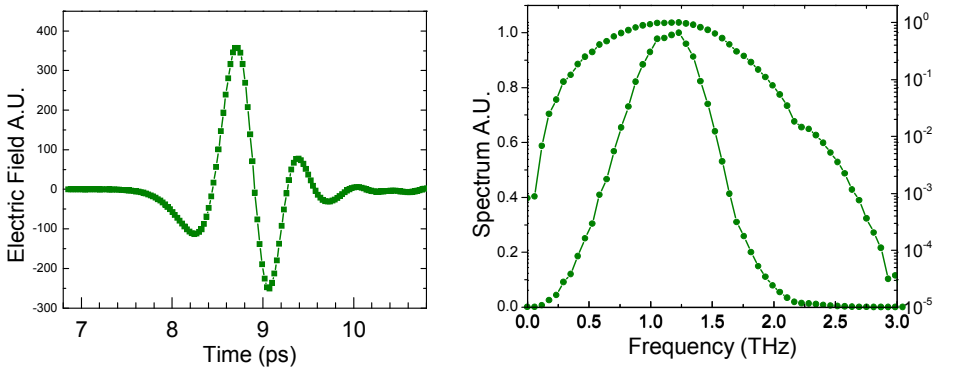


**Figure 6.9** Electric field (right) and spectrum (left) generated from plasma oscillations in an n-doped 2 $10^{-16}$ epilayer of a <100> GaAs wafer.

the THz power is maximized when the wafer is tilted at large angles with respect to the pump beam.

The THz electric field and the corresponding spectrum with the wafer tilted near Brewster's angle are shown in Figure 6.9. The THz electric is a one-cycle electromagnetic pulse with a broad spectrum centered at 1.2 THz. The calculated plasma frequency of the epilayer from the nominal doping is 1.35 THz.

## *Biased GaAs THz emitters*

A strong electric field can be applied in GaAs by fabricating metal gates on the GaAs surface. If the GaAs is semi-insulating, the resistance between the gates will be

high and no current will flow between gates that are biased. When a femtosecond laser strikes, the surface photo generated carriers will be absorbed and make the GaAs conductive. A current will be produced as they are accelerated across the applied electric field. The times scale on which this happens is the time duration of the laser pulse (~100fs). The femtosecond laser effectively gates an ultrafast current surge which emits electromagnetic radiation into free space.

For high carrier densities, after the carriers are initially accelerated by the applied electric field, an opposing space charge field will develop and decelerate the carriers[25]. The radiated electromagnetic field will be proportional to the time derivative of the photocurrent. Thus the current pulse produce by the femtosecond laser will have both positive and negative portions of the time derivative of the current, and the emitted electromagnetic wave will be a one-cycle pulse.

In contrast to the emission of THz radiation from plasma oscillations, the direction of the current surge (which may be viewed as a radiating dipole) will be parallel to the plane of the wafer. The polarization of electromagnetic radiation will be in the plane of the wafer. The emitted THz power will be radiated in the forward direction (normal the wafer's surface) where the dipole's radiation patterned is maximized. Because of this, THz power from biased GaAs emitters will typically be higher then the THz power produced by plasma oscillations.

The emitted THz power will increase as the laser power and applied bias are increased. However at high fields, electric breakdown can occur which will permanently short the devices. GaAs is more prone to breakdown at higher

temperatures. High bias and laser power will create a large amount of resistive heating, increasing the possibility of breakdown. For obtaining maximum THz powers, extracting the excess heat from the biased GaAs emitters becomes critical[26].

The THz beam can be modulated by applying a voltage square wave across the GaAs emitter. This has several advantages over using a chopper to modulate the THz signal. The THz beam can be modulated at higher frequencies to reduce 1/f noise. A chopper will also produce vibrations and air currents than can cause detection of spurious signals at the reference frequency. With electrical modulation, there will be no mechanical vibrations. Electrical modulation also offers control over the modulation function. For example the emitters can modulated with either a square wave or a pure sin wave. This control over the modulation function enables the duty

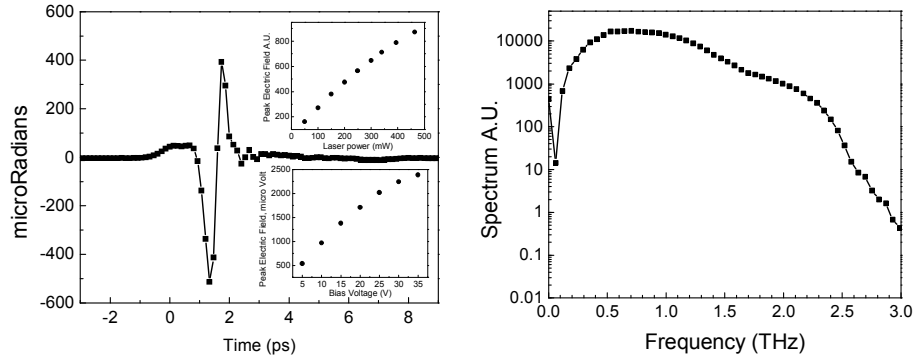


**Figure 6.10** Left: Emitted THz electric field from the GaAs biased at 35V. Inserts: Peak THz electric field versus bias voltage, and laser pump power. Right: Spectrum of the biased GaAs emitter.

cycle to be reduced, which will minimize device heating and extend their lifetimes.

Jing Xu built and tested a published "microstructure" design of a biased GaAs THz emitter[27]. The microstructure emitter consists of two finger gates. With the fingers biased the applied electric field alternates directions. If the laser is illuminated over the entire emitter, complete destructive interference of the THz radiation would occur. To prevent this, alternating finger regions are blocked from the femtosecond laser by masks fabricated over the finger structure.

The fabrication of the microstructure emitters is straightforward. The finger gate is patterned on the GaAs using e-beam evaporation of Au and liftoff with negative photoresist. On top of the Au finger gates an insulating $SiO_2$ layer is grown by plasma enhanced chemical vapor deposition (PECVD). Evaporated Pd is used as sticking agent between the Au and $SiO_2$. Au mask is patterned over the finger gates to ensure the laser strikes only regions of GaAs where the applied electric field has the same polarity. The metal mask reflects the laser beam and the insulating layer of $SiO_2$ prevents the metal mask from shorting the finger gates.

The spacing between the gates was 5$\mu$m. In contrast to the microstructure paper the area of the device was 100 x 100$\mu$m and no Si lens was used. The pump beam was focused onto the sample with an achromatic lens. The measured THz electric field and spectrum from the device are shown in Figure 6.10. With the 2mm ZnTe maximum rotation of the probe beam is on the order of 500 $\mu$Radians. At a bias of 35 Volts the electric field is on the order of 70 KV/cm. However all the devices would

eventually burn out at a bias 35 V if operated for a prolong time. To prevent device destruction the emitters were operated at bias below 20 V.

In Figure 6.10 the peak electric field is observed to increase linearly with applied bias at the maximum pump power (500mW). This can be explained if a simple capacitor model of the emitter is used. The femtosecond laser beam can be thought of as releasing the store energy of the capacitor which is emitted as THz radiation. The energy of a capacitor scales as the applied voltage square, and thus the emitted THz electric field (which is proportional to the square root of the emitted power) should be proportional to the square of the applied voltage. The peak THz electric field is also observed to increase linearly with pump power at a bias of 10Volts. The photo-generated carrier density which will be proportional to the current is proportional to the laser pump power. The radiated THz electric field is proportional to the derivative of the current, and thus the THz electric field should be proportional to the laser beam's pump power.

# 7 GaAs photonic crystal fabrication

Active THz devices could be placed inside GaAs photonic crystals. The photonic crystal modes could then directly interact with active devices to improve or enable device performance. It is routine to make quantum dots and quantum wells out of GaAs based III-V materials which can be made to have transitions at THz frequencies. THz Quantum cascade laser made of III-V GaAs based materials have lased at THz frequencies[28]. Shallow impurities in GaAs have hydrogenic outer electron levels with THz transitions. For THz photonic crystals fabricated from GaAs one can imagine active photonic crystal modes interacting with THz devices inside the photonic crystal. This is not possible with THz photonic crystals made from Si, or high density polyethylene. Such photonic crystals can only function as passive devices.

## *Coherent manipulation and quantum information processing*

Cole et al. observed coherent Rabi oscillations between the 1S and $2P^+$states of impurities in GaAs[29]. The transitions were driven by intense monochromatic THz pulses produced by UCSB's free electron laser. The 1S to $2P^+$ transition was brought into resonance with the monochromatic THz radiation with a magnetic field. The excited 2P+ state population was detected by ionization into the conduction band. The Rabi oscillations were heavily damped. However, this was due the destructive

nature of the $2P^+$ population measurement, and did not reflect the decoherence time of the system. Optical based measurement schemes would enable the impurity's state to be detected below the conduction band[30] and remove the measurement induced decoherence.

It has been proposed that a quantum logic gate could be created using Rabi oscillations to drive qubits, cavity vacuum Rabi oscillations to entangle qubits, and an appropriate readout scheme to measure the qubits[31]. Vacuum Rabi splitting of exciton quantum dot transitions have already been observed in photonic crystal cavities[32] The splitting is a manifestation of the entanglement of the cavity photon modes with the quantum states inside the cavity. This scheme could be applied to the THz regime using GaAs impurities as the qubits[33]. This would entail entangling THz photons with impurity states in a THz cavity, and the readout of individual states of the impurity atoms.

The optical phonon energy in GaAs is $288cm^{-1}$. Multiple photon transitions to the optical phonon line are expected to be the main source of decoherence. Previously in Chapter 1 we have seen that phonon transitions are responsible for absorption in GaAs at THz frequencies. However at low temperatures the population of phonons is suppressed and the probability for multi-phonon processes at THz frequency is expected to be negligible. The implementation of this scheme would require a THz resonator with GaAs inside it, or a resonator made out of GaAs. A photonic crystal cavity would be one candidate for such a resonator.

## *THz quantum cascade lasers*

Recently THz quantum cascade lasers have been produced that emit at THz frequencies[34]. A quantum cascade structure consists of series of repeating units of superlattices and quantum wells. Under an applied voltage bias electrons cascade down the series of levels by tunneling between levels and dropping down to lower levels. The quantum lifetimes of the levels are engineered so the lifetime of the upper lasing level is relatively long while the lifetime of the lower lasing level is very fast. This enables a population inversion to occur and lasing to proceed.

The cavity of the laser is formed by dielectric air interfaces cleaved or etched on the sides of the structure. THz radiation is confined in vertical direction either by two metal layers[35], or an evanescent plasmon waveguide[36]. An important aspect of a lasing is the interaction between the modes of the cavity and the lasing transitions. Photonic crystals can be employed to "engineer" the properties of laser cavities to improve performance. A THz GaAs photonic crystal could be used as a resonator to improve the performance of a THz quantum cascade laser.

## *Lasers and optical cavities*

The cavity of a laser serves as the feedback mechanism for lasing. A fraction $\beta$ of photons created by spontaneous emission will be emitted into the lasing mode of the cavity and induce stimulated emission. The photons created by stimulated emission will be recycled by the cavity to induce further stimulated emission. If the gain from stimulated emission is equal to the mode's total loss from absorption and

radiation leakage, lasing will occurs. The rate of stimulated emission is proportional to the energy density (or photonic density of states) of the lasing mode. The photonic density of states will be dependent on the properties of the cavity of the laser. Thus the laser cavity plays an important role in determining a laser's characteristics and whether a device will lase or not.

## *Photonic crystal defect cavities*

Photonic crystal cavities can be made by introducing defects in photonic crystals. Removing a single air hole in a photonic crystal slab will create a cavity with a modal volume on the order of a cubic wavelength. The photonic density of states will be very large at the mode's resonant frequency. A high portion of the spontaneous emission will be emitted into the cavity mode. For cavities with a model volume of a cubic wavelength the value of $\beta$ (the fraction of spontaneous emission emitted into the lasing mode) can very high and approach unity. As the value $\beta$ increases the lasing threshold of the cavity will decrease[37].

In addition the fraction of spontaneous emission emitted into a cavity mode, the rate of spontaneous emission can also be increased with a sub-wavelength cavity with a high quality factor.

Spontaneous emission can be viewed as stimulated emission by virtual photons. Stimulated emission is proportional to the energy density. The "energy density" of virtual photons will be increased as a cavity is made smaller. The enhancement of spontaneous emission for a cavity of volume V, with quality factor Q is

$$\frac{3}{4\pi^2}\left(\frac{\lambda}{n}\right)^3\left(\frac{Q}{V}\right) \tag{7.1}$$

(7.1) is also known as the Purcell factor[38].

## *Quasi-resonators*

Photonic crystals modify the dispersion curves (or photonic bands) of light. At a reciprocal lattice point, the bands are often flat and d$\omega$/d$k$ is zero. For these points the group velocity is very small and must be found from higher derivatives.

The slow group velocity at reciprocal lattice points can arises from strong diffraction at these points. Photons at reciprocal lattice points can be thought of as being diffracted - or scattered - backwards and forwards with no net velocity. The photonic density of state is proportional to d$\omega$/d$k$ and will be very high at the reciprocal lattice points. The slow group and high density of states of can lead to increase amplification in gain mediums.[39]

Photons scattering back and forth on itself can be viewed to be in a "quasi-resonance". If photons at a reciprocal lattice point are spatially localized, they will slowly diffuse outward via diffraction. This "quasi-resonance" can be used as a resonator for lasing[40]. A mode at a reciprocal lattice point with a very high density of states is somewhat analogous to a bond state which has an infinite density of states.

For lasing at a reciprocal lattice point, light can be coupled out of the edge of the photonic crystal. (Under specific conditions, it may also be diffracted out of the photonic crystal slab - see Figure 8.3 and the accompanying discussion on leaky

modes). Lasing at a photonic crystal's reciprocal lattice points is a two dimensional version of a distributed feedback laser[41]. Distributed feedback lasers can be viewed as a one dimensional photonic crystal lasers.

## *GaAs and Si reactive ion etching*

In contrast to Si, etching deep anisotropic features into GaAs wafers is challenging. A strong driver of Si RIE technology is the fabrication of MEMS and micromachining devices. To meet the demands of the MEMS industry advanced RIE processes have been developed for etching Si such as deep reactive ion etching (DRIE). DRIE consists of series of iterative steps. Each step has a specific function during the etch. For example in the passivation step, a carbon based coating is deposited on the sidewalls to ensure an anisotropic etch. While during the etch step, the Si is etched with a fluorine based chemistry. Between steps the gas composition, gas flow rate, RF power, and chamber pressure are all changed on timescale of a second. The etch must also proceed at a rate of a few microns per minute. This puts a lot of demands on the RIE machine. However, due to the demands of the MEMS industry, commercial machines and processes have been developed that have enabled deep anisotropic etches in Si to become routine.

To the author's knowledge, there are no commercial machines that employ iterative etching process for GaAs. However, there is some interest in etching deep vias into GaAs wafers for microwave circuits. An inductively coupled plasma (ICP) can be used to generate high plasma densities, and provide high etch rates. GaAs

reactive ion etching often uses chlorine based chemistry as opposed to the fluorine based chemistry used for Si etches. Since there is no iterative etching process to passivate sidewalls, GaAs are not as anisotropic and selective as Si etches. The result is that it is more difficult to etch deep anisotropic vias in GaAs. In general for GaAs etches, as the etch depth increases the condition of the etch will rapidly deteriorates.

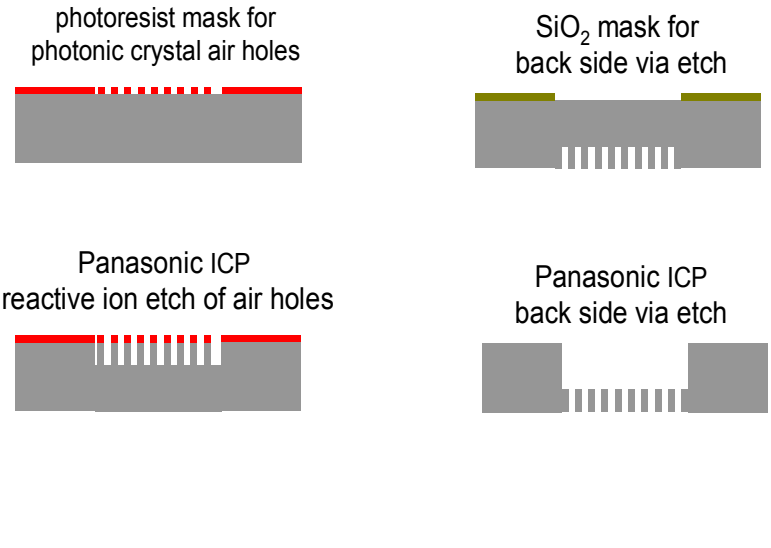


**Figure 7.1** Schematic of the GaAs THz photonic crystal fabrication process.

## *GaAs THz photonic crystal fabrication process*

Figure 7.1 shows a schematic of the fabrication process of GaAs THz photonic crystals. To make GaAs photonic crystal slabs, the air holes are first etched into the GaAs wafer using a Panasonic ICP RIE machine. The mask for the air holes was a thick layer of resist (>5$\mu$m) patterned with photolithography. The air holes were arranged in a triangular lattice and covered 4mmx4mm region of the wafer. Air hole

etches were typically 35$\mu$m to 65$\mu$m deep. After the initial air hole etch, a thick layer of PECVD grown $SiO_2$ was deposited on the back side of the wafer.

A 4mm diameter circular hole was transferred into the $SiO_2$ layer using photolithography and a hydrofluoric acid wet etch. A contact aligner with an infrared camera was used to align the 4mm diameter circle with air-holes on the other side of the wafer. A 4 mm circular via was etched into the back side of the wafer (with the Panasonic ICP) until the bottom of the air holes were reached. No etch stop was used for the via etch. The etch rate was calculated, and the via etch was timed. AlGaAs could be have been used as an etch stop with fluorine added to the plasma. However, this would have required a MBE growth of 40 $\mu$m of material. Under the right processing conditions, the back surfaces of the photonic crystal slabs were found to be relatively smooth. The thickness of the photonic crystal slabs found to be relatively uniform except for the regions of the slab near the via's sidewalls.

### *Air hole etch*

The Panasonic ICP uses a chemistry of $Cl_2$, $BCl_3$ and Ar to etch GaAs. Cl ions are the reactive component of the etch. $Cl_2$ etches of GaAs have isotropic profiles with a lot of local sidewall roughness. The addition of $BCl_3$ is believed to promote sidewall passivation. With $BCl_3$ added to the plasma, smoother sidewalls with a more vertical sidewall profile are produced. Argon is believed to stabilize the plasma and improve the etch's consistency by sputtering residues off the surface.

Many different materials are etched in the Panasonic ICP. Residue from prior etches can remain on the chamber's sidewalls altering the etch characteristics. This will lead to inconsistencies from run to run. To prevent this, the chamber was cleaned with a $CF_4/O_2$ plasma, and then coated with a $CL_2/BCl_3/Ar$ plasma having the same composition as the etch's plasma, before each series of etches.

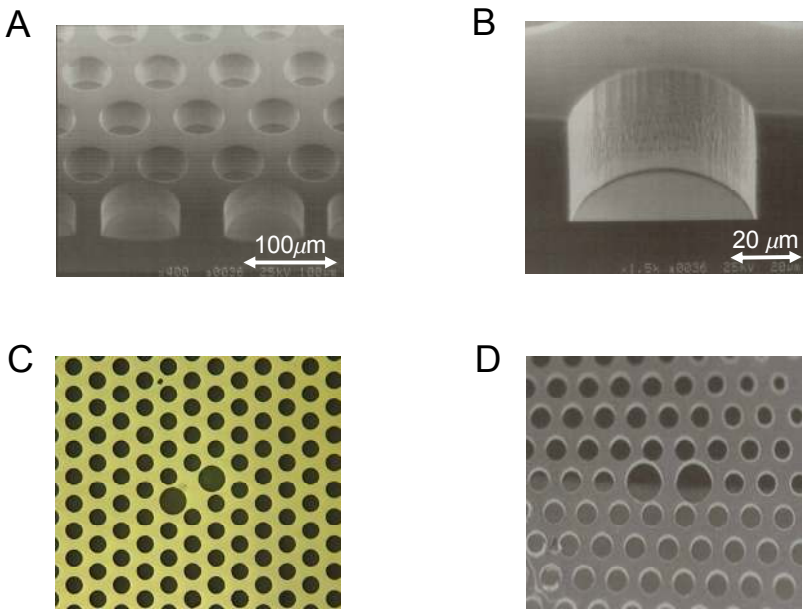


**Figure 7.2** THz photonic crystals with a defect. A. Cleaved image of the air hole etch. B. Close up of an air hole. C. Optical microscope picture. D. SEM image of the back side after the back side via etch.

The Panasonic ICP only handles 6 inch carrier wafers. The carrier wafers are mounted in the chamber with an electrostatic clamp. During the etch the back side of the wafer (which is not exposed to the plasma) is cooled with helium gas. This prevents the plasma from heating up the surface of the wafer. If the samples are not thermally connected to the carrier wafer, the etch's characteristics will deteriorate.

The GaAs samples typically had an area less then one square centimeter. They were thermally attached to carrier wafers using a liberal amount of vacuum pump oil. All of the carrier wafers were coated with a top layer of $SiO_2$, and only clean carrier wafers were used. Bare Si wafers were never used as a carrier wafers.

Initially AZ4330 photoresist was used as an etch mask. It was spun on at 3000 rotations per minute (RPMs) to produce a 4.5 $\mu$m thick layer of resist. The selectivity of the photoresist was high enough to allow for 35-40 $\mu$m deep air holes. The consistency of etches would vary from etch to etch. Some air hole etches were excellent as shown in Figure 7.2. The etch rate was 7-8 $\mu$m per minute. After the etch the remaining photoresist was on the order of 1.5 $\mu$m thick.

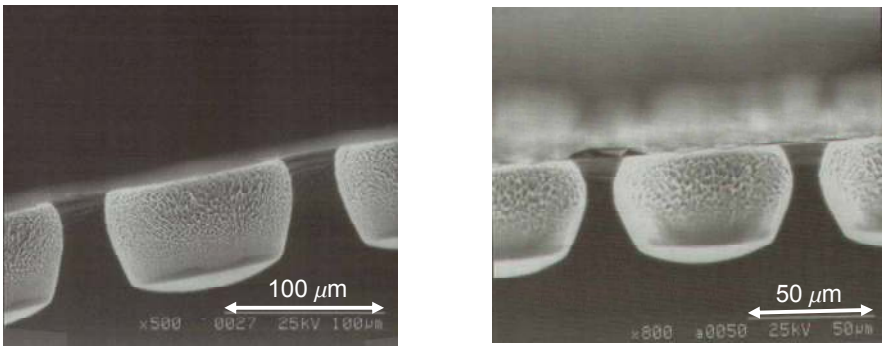


**Figure 7.3** SEM images of GaAs with a $SiO_2$ hard mask pattern by RIE etching (left) and an hydrofluoric acid wet etch (right).

The selectivity of the photoresist limited the depth of the air hole etches. Deeper etches were desired for, lower frequencies, TM photonic crystals, and to minimize the effect of over etching during the via etch. $SiO_2$ has a greater selectivity then

photoresist, and $SiO_2$ was tried as a mask material. With $SiO_2$ masks the sidewall profile of the etches became isotropic and rough as shown in Figure 7.3.

Initially a HF wet etch was used to transfer the resist pattern into the $SiO_2$ mask. Anisotropic $SiO_2$ masks were also etched in the Panasonic ICP using a $CHF_3/O_2$ chemistry. The Panasonic ICP is routinely used to etch vertical sidewalls in $SiO_2$ for MEMs etches with the Si deep reactive ion etcher. There are several well developed recipes for anisotropic $SiO_2$ etches with fast etch rates. Several recipes for anisotropic $SiO_2$ were used. However, similar results were obtained with anisotropic etched RIE etched $SiO_2$ masks as with an isotropic HF wet etch $SiO_2$ masks - as shown in Figure 7.3.

SPR-220-7 photoresist was used to obtain thicker resist films. Spinning AZ4330 photoresist at low spin speeds of 1500 and 2000 RPMs was also used. Both of these solutions allowed deeper etches, but the quality of the resist layer was not good. Later, it was found that AZ9260 produced high quality 6.5 $\mu$m resist films when spun on at 5,000 RPMs.

Overtime it was observed that the quality of the etches degraded. This probably was caused by changing chamber conditions as users etched exotic materials such as titanium in the Panasonic ICP. Near the end of this thesis it was found that the etching characteristics of the machine had drastically changed. Portions of the sidewalls were isotropic and rough. For short 4 minute air hole etches smooth sidewalls would be pocketed with rough holes and the top portion of the etch would

be severely undercut as shown in Figure 7.4 A. The roughness and isotropy of the etches were characteristics of a lack of passivation.

$CF_4$ was added to the plasma to try to coat the sidewalls with carbon increasing their resistance to being etched. However, no positive effect was observed when $CF_4$ was added as shown in Figure 7.4 B. .A higher ratio of to $Cl_2$ was used in an attempt to increase sidewall passivation. With a higher ratio $BCl_3$ the sidewalls were improved as shown in Figure 7.4 C and D. However a degree of roughness not present in earlier etches remained.

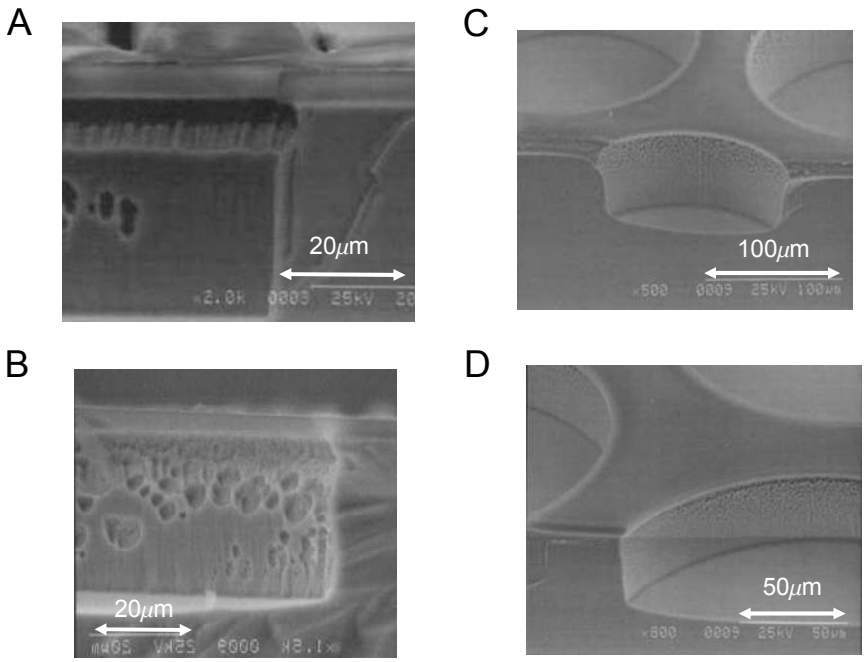


**Figure 7.4** (A) Standard air hole etch. (B) Air hole etch with the addition of 20 sccm $CF_4$ to the standard air hole etch. (C) Air hole etch with 60 sccm $BCl_3$. (D) Air hole etch with 70 sccm $BCl_3$. All etches were for 4 minutes long.

It was noticed that for the same etch conditions that GaAs etches with AZ4330 resists were slightly smoother then GaAs etches with AZ9260 resists. When photoresist is used as a mask, photoresist material will be introduced into the chamber. Carbon-based material deposited on sidewalls from resist removal has been shown to be a passivation agent for $Cl_2$/Ar etches[42 43]. The role of photoresist in the passivation of the etch was investigated by adding more photoresist to the chamber. Several microns of AZ4330 were spun on $SiO_2$ coated Si wafers. The area of the

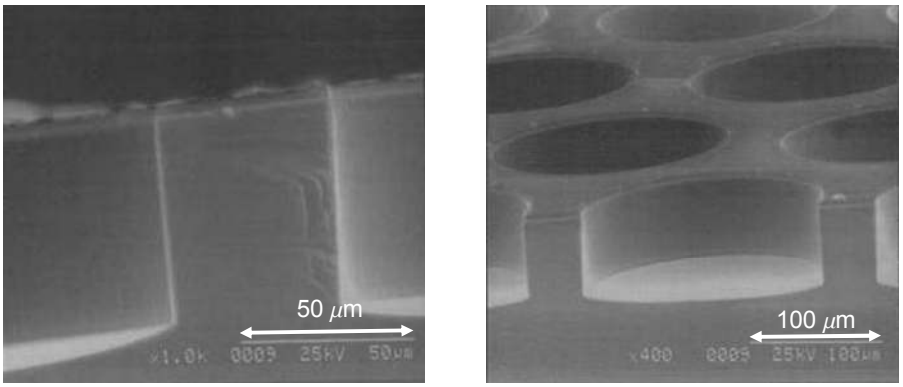


**Figure 7.5** SEM images of an air hole etch when resist coated wafers were placed in the chamber during the etch. The air hole etch was 8 minutes long.

wafers were 1-2 square inches. Two coated Si wafers were placed on either side of a GaAs sample during an air hole etch. The resist coated wafers were thermally contacted to the carrier wafer using vacuum pump oil. AZ9260 resist was used as a mask for the GaAs sample.

Figure 7.5 shows the results of an 8 minute etch (with a depth of ~60$\mu$m). The sidewalls are very anisotropic and smooth. This indicates that photoresist deposited on sidewalls is an important factor in the passivation of the sidewalls during the etch.

The addition of carbon to the plasma by adding $CF_4$ did not improve the anisotropy of the etch. This may indicate that a carbon based polymer is responsible for the sidewall passivation shown in Figure 7.5.

Resist passivation also explains why GaAs etches with $SiO_2$ mask were anisotropic and rough, while identical etches with photoresist masks had smooth anisotropic sidewalls. If photoresist is added to the chamber with a $SiO_2$ mask, the sidewalls should be smoother and more vertical. This could lead to deeper anisotropic etches in GaAs as the selectivity of $SiO_2$ is higher then photoresist. For very long etches multilayers of AZ4330 could be spun on Si wafers to ensure a constant supply of photoresist in the chamber throughout the etch.

Sharp spikes on the surface of the etch appeared in some air hole etches when photoresist was added to the chamber. These spikes are commonly referred to as grass. They are created when micromasks form on the surface. For THz GaAs photonic crystals the formation of grass is not a concern. It will be removed during the formation of the slab when the via etch reaches the bottom of the air hole etch. However if the grass is too thick, it can retard the etch rate. It will also lead to surface roughness when it comes in contact with a sidewall. There is probably an optimum amount of resist which will minimize the amount of grass while still allowing for vertical sidewalls. The aspect ratio of the etch may also play an important role in grass formation as it was observed that grass was more numerous when etching smaller air hole diameters.

If grass becomes a problem in the future, it can probably be reduced by increasing the Ar concentration in the plasma. More Ar will lead to more physical sputtering of the surface from Ar radicals. This will inhibit the formation of micromasks on the etch's surface.

### *Via etch*

Once the GaAs air holes were etched, the GaAs under the air holes needed to be removed. This was done so THz radiation could be confined at the bottom surface by total internal refraction. The back side of the wafer was cleaned and coated with a 4-6 $\mu$m layer of PECVD grown $SiO_2$. $SiO_2$ layer this thick is severely stressed. Careful handling of the wafers was necessary to prevent the stressed $SiO_2$ layer from peeling off the wafer. Any scratches on the $SiO_2$ layer would eventually result in the $SiO_2$ layer coming off the wafer. A large circular via with a diameter of 4 mm was etched into the back side of the wafers. AZ4330 resist was spun on top of the $SiO_2$. The circular via was aligned to the 4mm x 4 mm region of air holes using an IR camera on a contact aligner. The resist was exposed and developed. A hydrofluoric acid wet etch removed the exposed $SiO_2$. A wet etch is isotropic and will create sloping sidewalls. However, the sidewall quality of the via was not a concern as it is not part of the photonic crystal slab. After the wet etch all the resist was removed. No resist was placed put into the Panasonic ICP for the via etch. The same recipe as air hole etch was used for the via etch. The larger aspect ratio resulted in a faster etch rate on

the order of 10$\mu$m per minute. The bottom surface of the via etch was surprisingly smooth considering that approximately 450$\mu$m of material was removed.

However, any dirt or scratches present on the back surface of the wafer would create surface roughness as the etch progressed. During the lithography steps for the air hole etch, scratches would be created when back side of the wafer came in contact

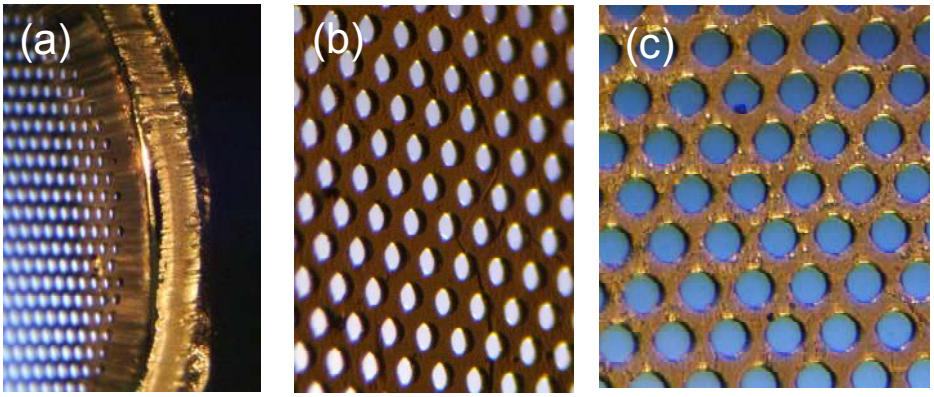


**Figure 7.6** Photographs of the back side of photonic crystals with lattice constants of 150$\mu$m (a) Photograph of the via sidewall (b) Photograph of the back side of a tilted photonic crystal slab. (c) Photograph of the back side of GaAs photonic crystal slab that is not tilted.

with the metal spinner and aligner chucks. To reduce back side scratches, a 200nm thick PECVD coating of $SiO_2$ was applied to the back side of the wafer before any lithography steps for the air hole etch. This $SiO_2$ coating protected the back surface of the wafer from scratches and kept it clean. It was removed with hydrofluoric acid before the deposition of the $SiO_2$ mask for the via etch. This allowed the $SiO_2$ via mask to be grown on a clean surface.

Before etching the wafer, its thickness was measured with a digital dial indicator. The etch rate of the 4mm diameter via was typically between 10 and 11 $\mu$m per minute. Using the estimated etch rate, the via was etched for a set time to a target depth of 50 to 100 $\mu$m above the bottom of the air holes. Afterwards the etch depth was measured using a microscope with a dial indicating the relative position of the objective lens with micron resolution. Any microscope lens has to be a specific distance away from the object for the image to be in focus. Under high magnification this distance cannot vary by more then a few microns. By recording the positions where the top and bottom of the etch would come into focus, the etch depth can be calculated. The error using this method is estimated to be less then +/- 5$\mu$m.

After the initial via etch, the target depth of the next via etch would be 10$\mu$m to 20$\mu$m above the air holes. The time of the etch would be calculated from the rate of the previous etch. Eventually, the etch would proceed in smaller increments of 5$\mu$m until the air holes were reached.

It was easy to over etch, and create a photonic crystal slab that was two thin. The best results were always obtained from a series of via etches targeted to reach progressively closer to the air holes. The actual etch depths were often over or under the targeted depths. By using a series of etches, errors in the desired targeted thickness of the photonic crystal could be minimized.

Once the air holes were seen from the back side of the wafer, the via etch was stopped. If the via etch was continued vacuum pump oil would eventually ooze out of the air holes onto the surface where it would act as a mask. The via etch would

reach the bottom of the air holes in the center of the via, and the bottom of the air holes near the sidewalls of the via at different times. The etch rate was slower near the sidewalls, then at the center of the via. However, for a region approximately $2/3^{rds}$ of the via radius away from the center, the air holes would always appear together. The thickness of this central region could not vary by more then 5$\mu$m which was the smallest increment etched for the via etches.

# 8 GaAs photonic crystal experimental results

This chapter describes measurements performed on GaAs photonic crystals slabs whose fabrication was described in the previous chapter. THz radiation was directly generated inside the photonic crystals with a femtosecond laser. Since the wavelength of the femtosecond lase is much less then the wavelength of the THz radiation, THz radiation could be coupled directly into the photonic crystal modes by either focusing, or spatially shaping the femtosecond laser beam on the photonic crystal surface. The emitted THz radiation from the slab was measured using free space electro-optic sampling (described Chapter 5).

Modes of a photonic crystal slab can be divided into TE and TM modes. TE (TM) modes have their electric field parallel (perpendicular) to the photonic crystal slab. The polarization of the THz electric field in the photonic crystal slab will determine what photonic crystal modes they are coupled to.

Optical rectification was used to try to couple into TE defect modes and observe photonic bandgaps. However it was unexpectedly discovered that the emitted THz radiation would saturate when it was brought to a focus. Because of this, no photonic defect modes, or signatures of photonic bandgap could be observed from the emitted spectra.

Plasma generated THz radiation was used to couple to leaky modes at the Γ point ($K_{Bloch}$=0). The leaky modes can form quasi-resonators at the high symmetry points of the Brillouin zone - such as the Γ point.

At normal incidence under patterned laser illumination sharp peaks in the emitted spectra were observed from the photonic crystal that corresponded to leaky mode emission. Both the spatial and phase dependence of the modes were investigated. Only dipole modes were found to radiate strongly in the forward direction. This was found to be consistent with finite-difference time domain (FDTD) based calculations of the far-fields.

The fact the photonic crystal signatures were found using doped epilayer photonic crystals, instead of <111> photonic crystal can be attributed to two factors. The THz power from the plasma generating wafers is much greater then the generated power using optical rectification. And, the TM wafer effectively nulls non-photonic crystal signals at normal incidence.

## *Coupling directly to photonic crystal modes*

There are numerous physical mechanisms (discussed in Chapter 6) by which a femtosecond laser incident on GaAs can create broad band THz radiation. In all of these cases the femtosecond laser can be envisioned as creating a collection of oscillating dipole point sources that emit THz radiation. The phase between identical dipole point sources is solely determined by the arrival time of the femtosecond laser. Emitted THz radiation will experience constructive and destructive interference at

different points in space. The interference pattern of the collection of the THz dipole point sources determines the direction of the emitted THz radiation. A femtosecond laser incident as plane wave on a GaAs wafer will generate a plane wave of THz radiation that obeys a Snell like law (see Chapter 6). A plane wave cannot couple into guided modes, or defect modes below the light-line.

If the femtosecond laser is focused to a spot less then the wavelength of the THz radiation in the semiconductor, it will approximate a single dipole point source of THz radiation. This single dipole point source will experience strong diffraction. It will be able to couple into defect modes and guided modes below the light-line. If the photonic crystal has a band gap, THz radiation generated in the slab with a frequency inside the bandgap will not be able to propagate in the slab. THz radiation could then be redistributed out of the slab[44]. If light is coupled to a defect mode, some Fourier components of the defect mode will be outside the light-line and radiate energy out of the slab.

## *Probing GaAs Photonic crystals with optical rectification*

THz photonic crystal slabs were made from <111> semi-insulating GaAs. Attempts were made to couple THz radiation generated by optical rectification into the photonic crystal modes. THz radiation is generated by optical rectification by frequency mixing between different spectral components of the femtosecond laser. The emitted THz field is proportional to a 2nd order nonlinear term of the polarization. The 2nd order susceptibility term that produces $P^2_{THz}$ is a tensor. The polarization of

the generated THz will depend on the crystal orientation and pump beam polarization in a complicated manner (see - Appendix A).

However for a <111> GaAs wafer the magnitude of the in plane and out of plane components of the polarization are constant. The in plane component $\sqrt{P_{x_{THz}}^2 + P_{y_{THz}}^2}$ is $\sqrt{2}$ times larger then the out of plane component $P_{z_{THz}}^2$. If the femtosecond laser is focused to a tight spot size, the in plane component $\sqrt{P_{x_{THz}}^2 + P_{y_{THz}}^2}$ will couple THz into the TE modes of the photonic crystal. The out of plane component $P_{z_{THz}}^2$ will couple THz into the TM modes of the photonic crystal.

Optical rectification generates broad band THz radiation with a frequency spanning over a THz. A defect mode will have a sharp resonance. Only a small fraction of the THz pulse's bandwidth will overlap the frequency of the defect mode. Any signal from a defect mode was expected to be small. Before probing defect modes an attempt was made to probe the bandgap of a THz photonic crystal.

Light with a frequency inside a photonic bandgap will be forbidden to propagate in the photonic crystal. Frequency components created inside a photonic crystal that are inside a bandgap may be redistributed outside of the slab.[46] With the femtosecond laser focused to a small spot size, generated THz frequencies outside of the band gap would couple into guided photonic crystal modes. Frequencies inside the band gap would not be able to couple into photonic crystal modes. It was hypothesized that the spectrum of the emitted THz would be enhancement for frequencies inside the band gap, and suppressed for frequencies outside of the band gap.

Photonic crystals with an air hole radius of .3$a$, a lattice constant of 94$\mu$m and a thickness of 40$\mu$m were fabricated out of <111> GaAs wafers. For these dimensions the photonic band gap should be centered at 1 THz with a width of 250 GHz.

## *Imaging the photonic crystal and femtosecond laser beam*

The <111> GaAs photonic crystal samples were placed at the focus of the collimating paraboloidal mirror in THz electro-optic sampling setup. A 30mm achromatic lens focused the near infrared pump beam onto the samples.

The samples were mounted in a rotation stage whose axis of rotation was parallel to the pump beam. The rotation stage was mounted on a xyz translation stage. This allowed the samples to be positioned at the focus with the pump beam. The position of the 30mm achromatic lens was fixed.

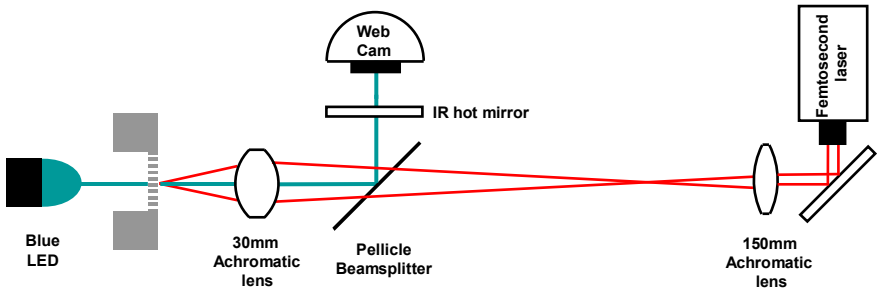


**Figure 8.1** Imaging system to view the focused laser beam and the photonic crystal surface at the same time.

The reflection from the photonic crystal surface was projected by a beamsplitter onto a webcam's CMOS array as shown in Figure 8.1. This allowed the focused laser spot on the photonic crystal to be imaged. To avoid saturating the webcam IR filters

were placed in front of the webcam. A blue light emitting diode placed behind the samples illuminated the air holes of the photonic crystals. (Later a green laser pointer was used).

To form an image of the air holes at the surface, the photonic crystal must be placed beyond the focus of the 30mm lens. But then the focus of the laser beam would not be on the photonic crystal surface. To allow both the air hole image and the focused laser spot to be imaged simultaneously, a 150mm achromatic lens was inserted far away from the 30mm lens as in Figure 8.1.

The two lens system had an effective focal length slightly longer then 30mm. This enabled the focused laser beam and the photonic crystal image to in-focus at the same position. The position of the 150mm lens was fixed and determined the positions where both the laser spot and photonic crystal surface would be in focus. The webcam and sample were both mounted on a translation stages and their positions could be moved to bring both images in focus.

## *Faraday optical isolator*

When the pump beam was focused with the 30mm lens, the laser reflections off the sample would travel back into the laser cavity. This would perturb the mode locking of the laser and introduce laser noise. Noise was not present on the scope trace of a fast photodiode inside the Ti: Sapphire laser. However, the electro-optic signal on the lock-in amplifier would experience large fluctuations. The electro-noise floor is small ~ $10^{-7}\mu\Gamma$. Even with the majority of laser noise nulled by the

optical bridge, a small amount of laser noise can overwhelm any signal. Back reflection into the laser cavity can be eliminated by using a longer focal length lens and slightly tilting the sample, so any back reflections will miss the lens. This was not possible with the 30mm lens which had a diameter of 25mm. To eliminate back reflections entering the laser cavity a faraday isolator was inserted into the pump beam line.

## *Experimental results from optical rectification*

The femtosecond laser beam was focused onto the <111> GaAs THz photonic crystals in an attempt to see redistributed emission out of the slab for frequencies within the bandgap. THz emerging from a small area will lead to collection losses from diffraction. However, the THz power generated by optical rectification is proportional to the square of the input laser beam power. It was assumed diffraction losses would be compensated by increased power produced from the higher electric field at the focus.

When the laser beam was focused on the photonic crystal sample, the observed signal approached the noise limit of the electro-optic sampling measurement. The dependence of the emitted THz radiation was measured as a function the input pump power as shown in Figure 8.2. For high pump powers the electro-optic signal had a DC offset - believed to be caused by laser reflections that returned to the laser cavity. The faraday isolator attenuates back reflections by a factor of over $10^3$ but does not eliminate them. In Figure 8.2 the DC offset has been subtracted from the electro-

optic signal. When the input laser power was varied by a factor of six, the output THz signal did not change. The emitted THz signal saturated with input laser power as low as 25mW. When the laser beam was unfocused, the THz power dependence

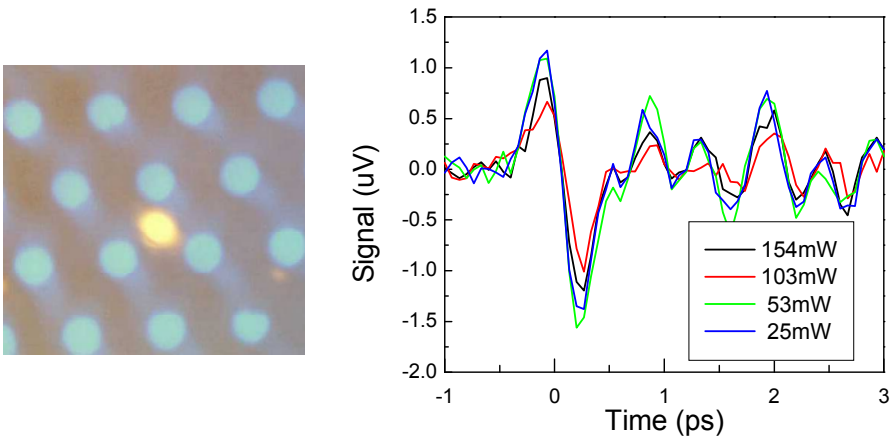


**Figure 8.2** Power dependence of the emitted THz signal when the femtosecond laser was focused to a tight spot on the photonic crystal.

varied quadratically with the input laser power as shown in Figure 6.4.

The optical rectification with light below the bandgap of GaAs, the nonlinear susceptibility $\chi^2$ has an imaginary component[45]. This implies absorption of carriers is necessary to generate THz radiation. It was believed saturation of the absorption of a carriers in the <111> GaAs caused the output THz signal to saturate with input laser power.

No signature of the bandgap could be observed. In order to reduce saturation while still diffracting into guided modes a cylindrical lens was used to bring the laser to a line focus. But the signal was still small, and no bandgaps signature was

observed. TE photonic crystals defects were also investigated, but the signal to noise was to low to perform measurements.

## *Probing GaAs photonic crystals with plasma oscillations*

GaAs photonic crystal slabs were fabricated from a semi-insulating <100> GaAs wafer. The wafer had a $2x10^{-16}$ $cm^{-3}$ n-doped epilayer on the surface. The doped epilayer produced THz radiation from plasma oscillations initiated by a femtosecond laser pulse. The photonic crystal slabs consisted of circular air holes arranged in a triangular lattice with a period of 150$\mu$m and a thickness of $\leq$ 60$\mu$m.

Four THz photonic crystal samples were made labeled W1, W2, W3, and W4. The air hole radius of the samples W1, W2, W3, and W4 were .20*a*, .31*a*, .31*a*, and .26*a* respectively. The thickness of samples W1, W2, W3, and W4 were 25$\mu$m, 41$\mu$m, 60$\mu$m, and 60$\mu$m respectively.

When the femtosecond laser strikes the GaAs epilayer photo-generated carriers are created. The photo-carriers are accelerated by the surface depletion field. This drives plasma oscillations in the epilayer which generate THz radiation. The generated THz electric field will be parallel to the surface depletion field which is normal to the GaAs surface. Plasma generated THz radiation will only couple to the TM modes which have their electric fields normal to the surface.

In contrast to TE modes, the TM modes of a triangular photonic crystal slab will not have a bandgap - unless the index of refraction and air hole index are very large. By introducing a defect in photonic crystal with a bandgap resonant cavities can be

formed. Without a bandgap it is not possible create TM resonant cavities. However, photonic crystal can have quasi-resonances when a mode has reciprocal lattice wav vector. Modes above the light-line are "leaky" and can be diffracted out of the photonic crystal slab. The TM modes with quasi-resonances above the light-line can be diffracted out of the slab. THz radiation coupled these leaky modes could then detected outside the slab using free space electro-optic sampling.

## *Leaky photonic crystal modes*

For leaky modes above the light-line, photonic crystal slabs can be viewed as two dimensional diffraction gratings[46]. Diffraction can be viewed as a scattering process with an initial and final state. For planes waves the initial and final states can be described in terms of the in-plane wave vector ($\mathbf{k}_{//}$) - that lies in the plane of the two dimensional grating - and the frequency ($\omega$). For light to diffracted or be scattered from a two dimensional grating two conditions must hold.[47] The initial ($\mathbf{k}_{i//}$) and final ($\mathbf{k}_{f//}$) in-plane wave vectors must differ by a reciprocal lattice vector ($\mathbf{G}$) such that $\mathbf{k}_{f//} = \mathbf{k}_{i//} - \mathbf{G}$. And the initial ($\omega_i$) and final ($\omega_f$) frequencies must be equal ($\omega_i = \omega_f$). The wave vector component normal to the surface ($k_z$) is not conversed, and light traveling in the in-plane direction can be diffracted out of the grating's plane.

To better understand of the plane diffraction, consider a one dimensional diffraction grating shown in Figure 8.3. Light incident at angle $\theta_l$ will diffract at angle $\theta_m$ if the wavelength of the light ($\lambda$) and period of the grating ($a$) satisfy the diffraction equation $m\lambda=a(\sin\theta_m - \sin\theta_l)$. When light travels in the plane of the

grating (at an angle $\theta_l = \pi/2$), it will be diffracted in the vertical direction ($\theta_m = 0$), if the period of the grating is a multiple of the wavelength $m\lambda = a$. This is equivalent to the in-plane wave vector of the light being equal to a reciprocal lattice vector of the

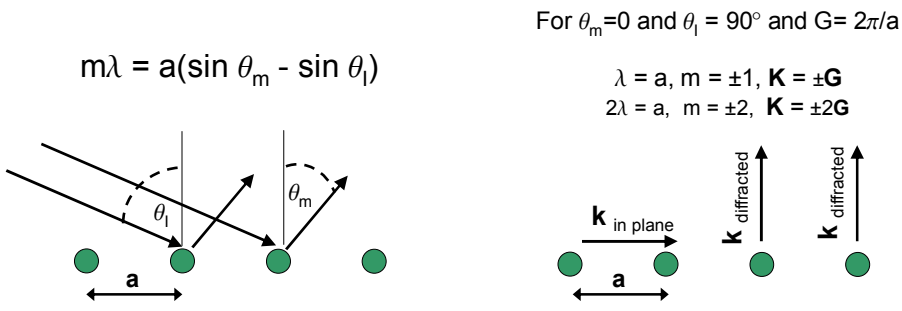


**Figure 8.3** Left: A one-dimensional diffraction grating. Right: Light traveling in the plane of the grating will be diffracted in the vertical direction if its wave vector is a reciprocal lattice vector of the grating.

grating ($2\pi/\lambda = m2\pi/a$). Diffraction out of a photonic crystal slab can occur in a similar manner.

For diffraction to occur the frequency condition $\omega_i = \omega_f$ must also be satisfied in addition to the wave vector condition $\mathbf{k}_{//f} = \mathbf{k}_{//i} + \mathbf{G}$. Because of the index of refraction, for a given $\omega$ the value of $|\mathbf{k}|$ will be different inside and outside a dielectric slab. Only light outside the light-line ($\mathbf{k}_{//} < \omega/c$) will be able to diffract out of the slab. Light inside the light-line ($\mathbf{k}_{//} > \omega/c$) will be able to satisfy the second diffraction condition $\omega_f = \omega_i$ only if $k_z$ is imaginary, and the wave is evanescent.

The light-line condition $\mathbf{k}_{//} < \omega/c$ is more restrictive for lower frequency modes. In general, leaky modes at higher frequencies will be able to diffract in more directions than leaky modes at lower frequencies. For some low frequency modes at

the Γ point, the only allowed direction for diffraction may be perpendicular to the slab.

### *Dipole radiation pattern - for focused excitation*

The emitted THz radiation from an unprocessed wafer was maximized when the wafer was tilted near Brewster's angle (74° in GaAs) while at normal incidence no emitted THz radiation was observed. The emitted THz radiation can be envisaged as arising from an array of THz dipoles oscillating normal to the slab. The radiation pattern of an individual dipole will be maximized perpendicular to the dipole and be zero parallel to the dipole axis. If excited by a femtosecond laser plane wave, the collection of dipoles will be forced to obey Snell's due to the collective interference of the dipoles.

By focusing the laser beam to a spot size much smaller then THz wavelengths, the oscillating dipoles will couple into photonic crystals slab modes. If these are leaky mode, they can be diffracted out of the slab by the photonic crystal.

Strong diffraction will occur for modes with Bloch wave vectors at the photonic crystal's reciprocal lattices. Since the interaction of light with the lattice is greatest at the reciprocal lattice points. The reciprocal lattice points of a triangular lattice are the Γ, X, and J points. At the Γ-point $k_{Bloch}=0$ and all of the modes will be above the light-line. The X and J points will have modes both below and above the light-line.

## *Emitted THz radiation from a line focus*

The femtosecond laser beam was brought to a line focus on the epilayer samples to couple into the leaky modes. A 25mm fused silica cylindrical lens was used to focus the laser beam. The laser beam was expanded by a factor of three before the

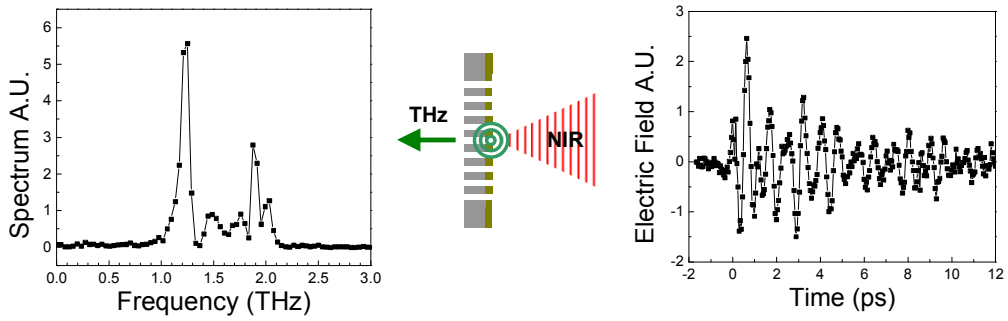


**Figure 8.4** The spectrum (left) and electric field (right) emitted by sample W4 when the pump laser beam is focused onto the photonic crystal slab with a cylindrical lens.

cylindrical lens to decrease the width of the focused laser line. The samples were rotated so the line focus was parallel to the Γ-J direction of the photonic crystals. This allowed the entire focused laser line to lie on the GaAs in between the photonic crystal's air holes.

Because of the cylindrical lens the photonic crystal surface could not be imaged. However, the photonic crystals could be positioned at the focus of the laser beam by looking at the transmitted light through the air holes with an IR card. (Since an IR card is laminated it will reflect laser light specularly. Wearing laser safety goggles that blocked 800nm light is mandatory using an IR card with a femtosecond laser.) With the photonic crystal not at the laser focus, the air holes could be seen on an IR

card held behind the sample. By moving the sample stage, the air holes could be made to disappear and reappear as the sample was translated into and out of the focus of the laser beam. By noting the micrometer positions when the air holes appeared and the disappeared, the approximate position of the laser focus could be found.

When the laser was focused on the samples with the cylindrical lens at normal incidence, THz radiation from the photonic crystals was observed. The emitted THz electric field consisted of a series of ringing oscillations and the spectrum of the field consisted of sharp peaks as shown in Figure 8.4. For sample W4 the sharpest and highest peaks were at 1.2 THz and 1.9 THz. The peaks are believed to be leaky modes diffracted out of the photonic crystal slab.

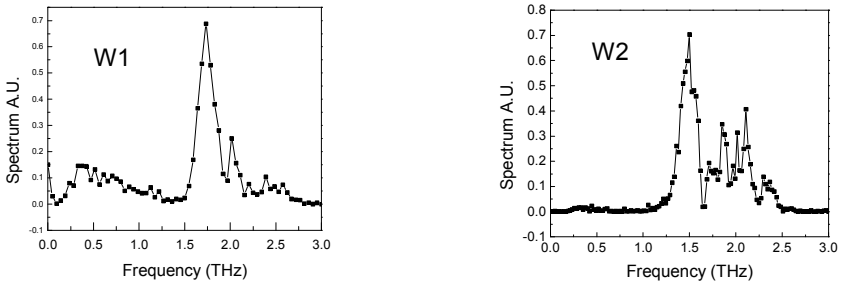


**Figure 8.5** The spectra of samples W1 (left) and W2 (right) with the pump beam is focus on the photonic crystals with a cylindrical lens.

At normal laser incidence, unprocessed portions of the GaAs wafer with the doped epilayer did not emit THz radiation. The unprocessed portions of the wafer would only emit THz radiation when they were tilted at an angle with respect to the femtosecond laser beam. The emitted THz electric field from a tilted wafer was a one-cycle electromagnetic pulse with a broad power spectrum as shown in Figure 6.9.

Figure 8.5 shows the spectra when the laser is focused with a cylindrical lens on samples W1, and W2. The peaks of samples W1, and W2 are broader then the peaks of sample W4. This was believed to be due to the quality of sample W4 which was much greater then the other samples. Viewed under a microscope W4's air hole were sharp and circular. The air holes of W1 and W2 were not sharp and W2's air holes had a somewhat oblong shape. The thickness of sample W4 is the same as the target thickness 60$\mu$m. Samples W1, and W2 (with thicknesses of 25$\mu$m and 41$\mu$m) were both over etched during the via etch. This could introduce back side surface variations in W1 and W2. The back side of sample W4 was the shiniest of the samples which indicates it has the smoothest back side surface.

The main peaks in the spectra samples W4, W2 and W1 spectra increase in frequency as the slabs become thinner. This is expected as the frequency of the bands increases as dielectric material is removed from photonic crystals.

The polarization of the emitted THz electric field was perpendicular to the line focus. For an emitted TM mode the magnetic field in the slab will be parallel to the line focus. The electric field will be perpendicular to the line focus and point in the direction perpendicular to the slab. When the light is diffracted out of the slab the electric field will be rotated by 90° while the magnetic field will remain in the same direction.

The xyz micrometer on the translation stage holding the sample was moved to maximize the signal. As the samples were moved across the line focus the signal would increase and decrease. There were regions of sample where the THz emission

would be stronger then other emission. The location of these regions could not be determined, since the cylindrical lens prevented image from being taken of the photonic crystal surface.

## *Spectra from tilted photonic crystals*

Plane waves can diffract into leaky modes, just as a leaky modes can diffract into plane waves. The photonic crystal samples were tilted with respect to the pump beam and THz was generated on the GaAs surface with an unfocused laser beam. The

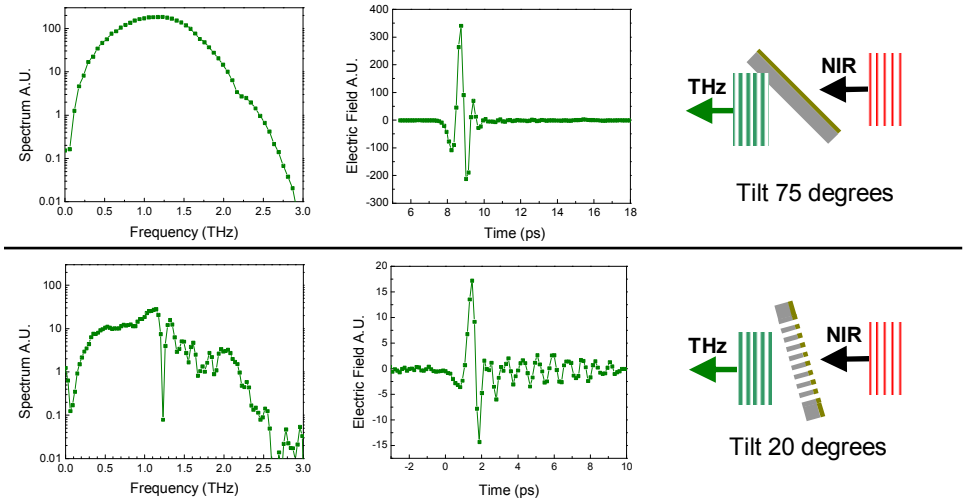


**Figure 8.6** Upper graphs: The spectrum and electric field of an unprocessed wafer tilted at 75°. Lower graphs: The spectrum and electric field of sample W4 tilted at 20°.

unpatterned THz "plane waves" were able to diffract into the leaky modes inside the photonic crystal slab. The emitted THz radiation was broad band, but showed absorption dips where the THz diffracted into the leaky modes inside the photonic crystal slab.

The lower portion of Figure 8.6 shows the electric field and spectrum of sample W4 when it was tilted by 20° and illuminated with an unfocused laser beam. For comparison the upper portion of Figure 8.6 shows the electric field and spectrum of an unprocessed wafer tilted at 75°. The electric field consists of a large one cycle pulse followed by ringing with smaller amplitude. The ringing indicates absorption lines in the spectrum of the pulse. Ringing was also observed in Figure 5.8 from water vapor lines when the vacuum box was exposed to error. However the data in Figure 8.6 was taken with the vacuum box purged. The absorption lines in Figure 8.6 are from diffraction into leaky photonic crystal modes.

With the exception of the absorption lines, the spectrum from the photonic crystal has a similar shape as the spectrum from the unprocessed wafer. The width

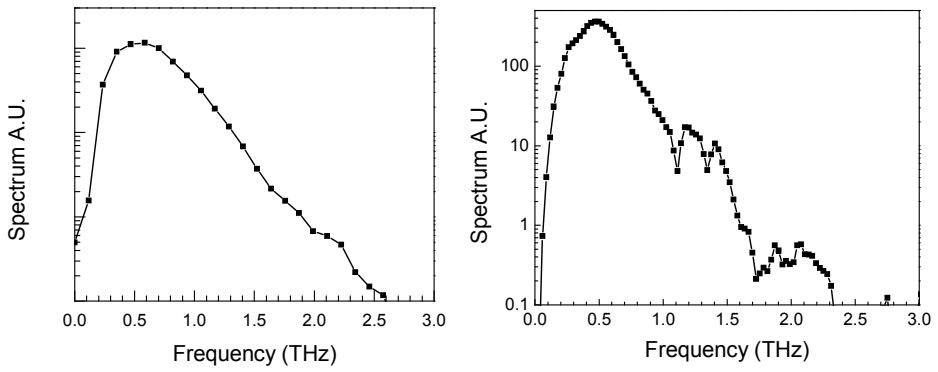


**Figure 8.7** Left: The spectrum when the back side of a un processed wafer is excited (near Brewster's angle) by the femtosecond laser. Right: They spectrum emitted by sample W3 when it is tilted and excited by the femtosecond laser.

and central frequency of both spectra are approximately the same.

The absorption line at 1.2 THz matches the frequency of the large peak in Figure 8.4 when the femtosecond laser was focused onto the sample with a cylindrical lens. Another absorption line in the lower portion of Figure 8.6 occurs near 1.9THz, which is same frequency of the 2nd largest peak in Figure 8.4.

In contrast to the other samples W3 shows anomalous behavior. When sample W3 is tilted the emitted spectrum is observed to shift to lower frequencies. The peak

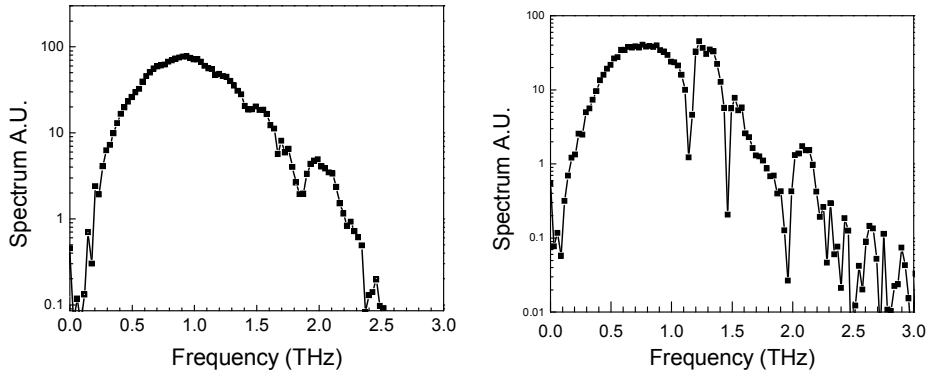


**Figure 8.8** The tilted spectra of sample W1 (left) and sample W2 (right) when the pump beam is unfocused.

of the tilted spectrum for sample W3 occurs near .5 THz and falls off sharply for higher frequencies as shown on the right side of Figure 8.7. The spectrum of the 500 $\mu$m thick unprocessed wafer is broader and it peaks at higher frequencies above 1 THz.

When the back side of an unprocessed wafer was illuminated with the pump beam near Brewster's angle THz emission was observed. The power of this emission was weaker then the front face of the wafer with the n-doped plasma wafer. The spectrum of the emitted THz from the back side of the wafer is shown left hand graph

of Figure 8.7. The power peaks near .5 THz and sharply rolls off afterwards. It bares a resemblance to the tilted spectrum sample W3.

A probable explanation for the anomalous results from sample W3, is that the back side of wafer W3 was accidentally processed instead of the front side. This could account for the different behavior of sample W3 from the other samples.

The tilted spectra of W2 and W1 are shown in Figure 8.8. Both wafers are tilted at 40° with respect to the wafer. The absorption dip of sample W1 occurs at the same frequency as the peak in W1's spectra when the laser beam is focused on it in Figure 8.5. There are three dips in the absorption spectrum of W2 one near 1.14THz, one at 1.46THz and on at 1.96THz. The middle dip appears to correspond to the large peak in the focused spectrum of W2 in Figure 8.5 while the peak at 1.96THz could correspond to one of the higher frequency peaks of Figure 8.5. It's not clear what the peak at 1.14THz corresponds to but it should be borne in mind that the sample is tilted at 40° while the focused spectra were taken at 0°.

## *Coupling into photonic crystal modes with a photomask*

The cylindrical lens prevented any image of the line focus being obtained by the webcam. Focusing the laser beam to a single spot resulted in a signal that was too small. To obtain image information while coupling into the photonic crystal modes, a photomask was inserted into the pump beam line. The image of the photomask was projected onto the photonic crystal by a lens. This created a patterned femtosecond laser excitation on the surface of the photonic crystal. The patterned laser excitation

generated a THz electric field distribution inside the photonic crystal. The THz electric field distribution will couple to photonic crystal modes if the overlap integral of the THz field profile with the photonic crystal modes must be nonzero.

A schematic of the experimental setup is shown in Figure 8.9. The pump beam was expanded by a factor of 3.95 by a beam expander. The beam expander consisted of a 19mm and 75mm achromatic lens. The distance separating the two lenses was

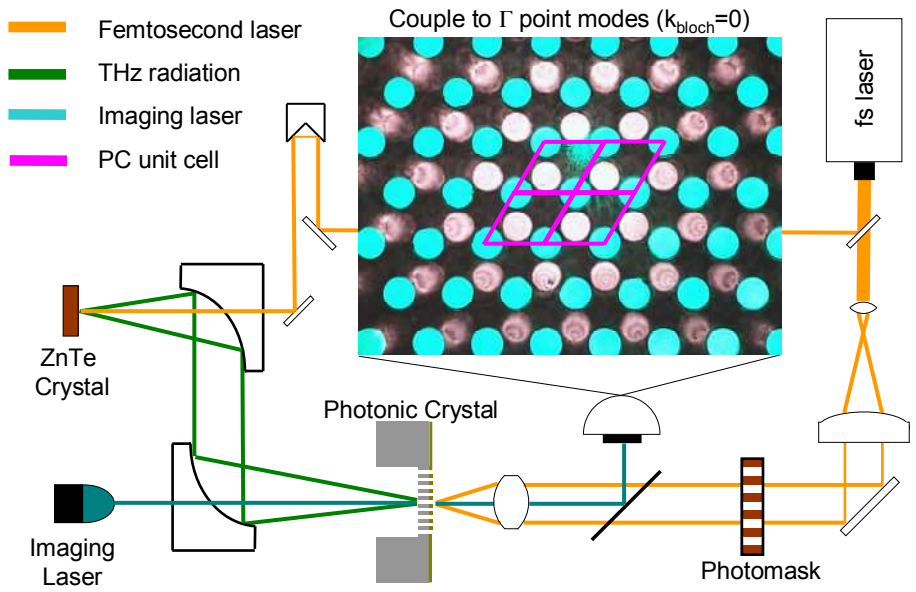


**Figure 8.9** Experimental setup with photomask. The laser beam is expanded (x4) and sent though a photomask. The image of the photomask is projected onto the sample with a 30mm lens. A pellicle beamsplitter sends the reflection of the photonic crystal surface into a webcam. An imaging laser illuminates the air holes. Paraboloidal mirrors collect the emitted THz from the photonic crystal and refocus it into the 2mm ZnTe crystal. The imaging laser, and the electro-optic probe beam pass thought small holes drilled into the paraboloidal mirrors.

the sum of their focal lengths. The pattern on the photomask had a lattice constant of 750$\mu$m. The image of the mask pattern was projected onto the photonic crystal

surface with a 30mm achromatic lens with a diameter of 1 inch. The reflected laser light from the surface of the photonic crystal was collected with same lens. A thin uncoated pellicle beam splitter picked off a portion of the reflected beam and directed it into the webcam.

To prevent saturation of the webcam IR hot mirrors were placed in the beam path before the photomask. IR hot mirrors reflect the majority of IR light incident on them while being transparent for visible frequencies. The IR hot mirrors had a minimal effect on the laser beam image. When the IR hot mirrors were slightly tilted the laser beam image did not change or move.

The webcam's lens was removed to expose its CMOS detector array. Reflected light from the surface of the photonic crystal formed an image on the exposed detector array. By removing the lens the color algorithm of the pixels was altered. The colors of the webcam images were not the true colors.

To image the air holes a green laser pointer was placed behind the photonic crystal. The green light was collected by the 30mm lens and reflected into the webcam by a pellicle beam splitter.

The green laser pointer was placed outside the vacuum box. It traveled into the vacuum box through a window directly opposite to the window the pump beam traveled through. A 1/8 inch diameter hole was drilled in the collecting paraboloidal mirror (identical to the hole in the focusing paraboloidal mirror). By placing the laser

pointer outside of the purge box, images of the photonic crystal could be taken while the vacuum box was purged.

The emitted THz radiation was collected from the side of the photonic crystal slab without the doped epilayer. The THz radiation was collected and then focused onto a 2mm ZnTe crystal with two identical paraboloidal mirrors. Each mirror had an effective focal length of 125mm and a diameter of 75mm.

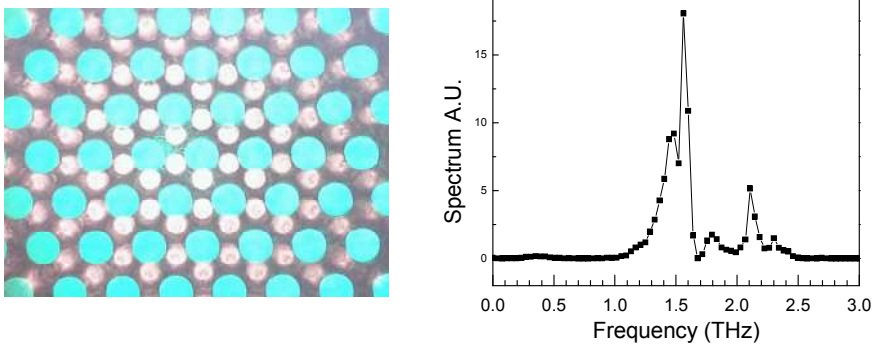


**Figure 8.10** The spectrum and corresponding image when a hexagonal mask pattern is projected on the photonic crystal sample W2.

The webcam, photomask, and sample were all attached to translation stages. The distances between the photomask, the sample, and the webcam relative to the 30mm lens could be adjusted. This allowed both the laser excitation and the photonic crystal surface, to be in-focus at the same position.

The photomasks were made of soda lime glass with a thickness of .06 or .09 inches. Soda lime glass will disperse the frequency components of a femtosecond laser pulse. This could lead to broadening of the femtosecond pulse and an attenuation of the THz signal. The emitted power from a tilted unprocessed wafer

was measured with and without a .09 inch thick soda lime glass in the beam path. The peak THz electric field was slightly attenuated (<10%) with the soda lime glass in the pump beam path. This could have been due to reflections and/or absorption in the soda lime glass. The normalized spectra of generated THz radiation with and without the soda lime glass were found to be identical. This implies the soda lime glass had a negligible effect on the femtosecond laser pulses.

## *Moving the photomask*

The position of the patterned laser excitation with respect to the photonic crystal could be changed by moving the photomask which was attached to a xyz translation stage. When the photomask was moved the positions of the 30mm lens, the photonic crystal sample, and the paraboloidal reflecting mirrors remained fixed. Changing the position of the photomask did not alter the paths of the femtosecond laser beams, and the emitted THz radiation. This allowed the emitted THz power dependence of the position of the laser pattern with respect to the photonic crystal to be investigated.

The period of the photomask image was reduced by a factor of 5 (750$\mu$m to 150$\mu$m) when it was projected onto the photonic crystal. If the photomask is move a given distance, the laser pattern on the surface of the photonic crystal will only be moved 1/5 the distance. This facilitated moving the laser pattern over very small distances on the photonic crystal.

Electro-optic sampling only detects THz electric fields parallel to the <110> edge of the ZnTe wafer. By rotating the ZnTe crystal 90° allowed the polarization dependence of the emitted THz radiation could be investigated.

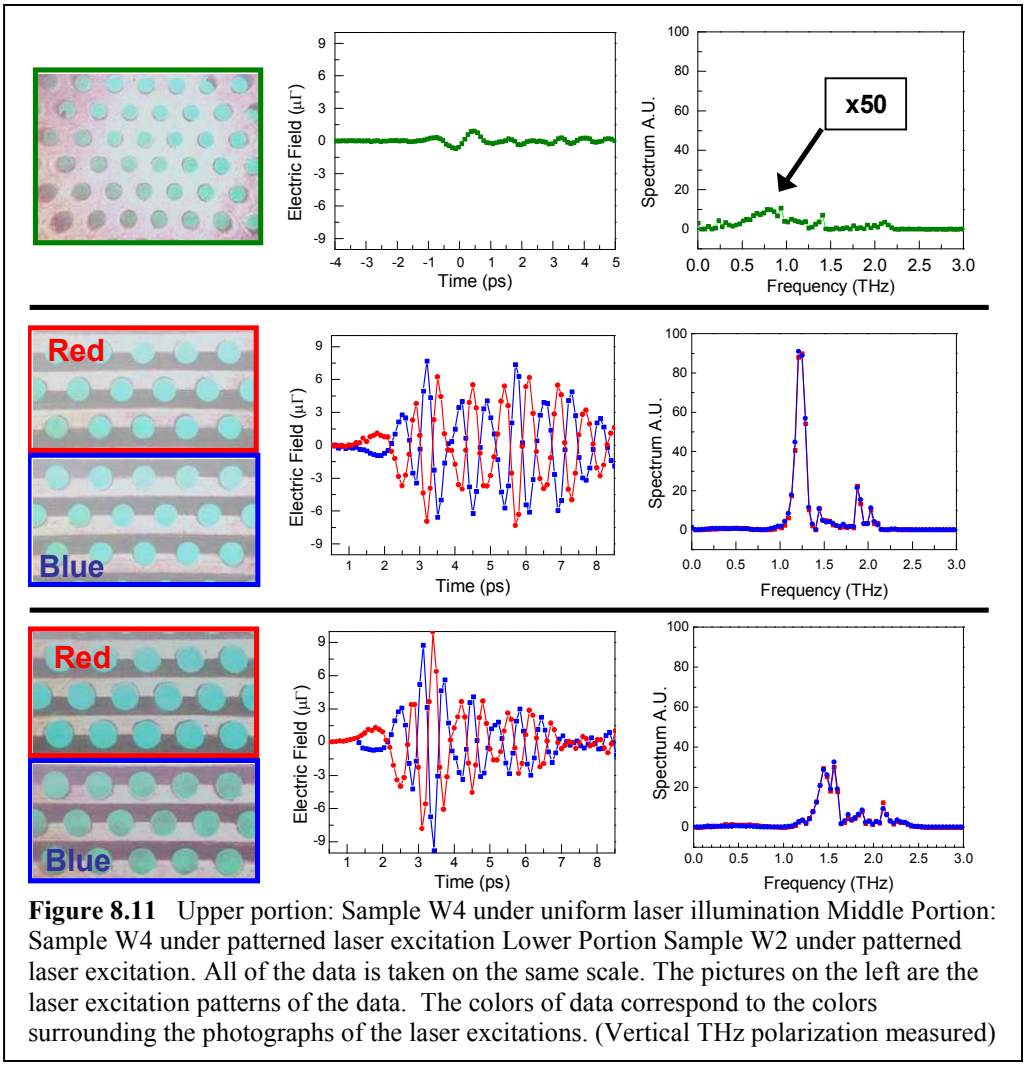


**Figure 8.11** Upper portion: Sample W4 under uniform laser illumination Middle Portion: Sample W4 under patterned laser excitation Lower Portion Sample W2 under patterned laser excitation. All of the data is taken on the same scale. The pictures on the left are the laser excitation patterns of the data. The colors of data correspond to the colors surrounding the photographs of the laser excitations. (Vertical THz polarization measured)

## *Periodic laser line excitation*

A THz electric field will not couple into a photonic crystal mode if the overlap integral of the generated THz electric field and the mode's electric field is zero. For

uniform laser excitation the overlap integral will often be zero. While for patterned laser excitation will the overlap integral will often be non-zero and direct coupling into the photonic crystal will be possible.

The top portion of Figure 8.11 shows the emitted THz electric field and power spectrum from sample W4 under uniform laser excitation at normal incidence. For Figure 8.11 the ZnTe crystal was rotated to detect the vertical component of the THz electric field. For uniform laser excitation the observed THz radiation is very small. The THz electric field consists of one cycle with small ringing afterwards. This is similar to the THz electric field emitted from a tilted photonic crystal under uniform laser illumination in Figure 8.6. For the upper portion of Figure 8.11 the sample is probably slightly tilted ( $< 1°$).

The middle portion of Figure 8.11 shows the THz electric field and power spectrum generated with pattern laser excitation at normal incidence. The laser pattern consisted of an array of straight lines with a period commensurate with the photonic crystal. In contrast to the upper portion of Figure 8.11, the electric field consists of many cycles and the power spectrum consists of peaks. The emitted THz power at normal incidence is much greater with patterned laser excitation than with uniform laser excitation. Note that the THz power spectrum from uniform laser illumination is multiplied by a factor of 50 in Figure 8.11.

The spectrum of sample W4 under patterned laser illumination in Figure 8.11 is similar to the spectrum of sample W4 under focused laser excitation in Figure 8.4. Some of the smaller peaks in Figure 8.4 are not present in the spectrum of W4 in

Figure 8.11. But all of the spectral peaks under patterned laser excitation in Figure 8.11 have corresponding spectral peaks under focused laser excitation in Figure 8.4.

The emitted THz power was found to be maximized when the laser lines were centered over the air-dielectric interfaces of the photonic crystal. The data in Figure 8.11 are taken for positions of the laser pattern that maximized the THz power. When the laser pattern was moved to be over the center of the opposite air-dielectric interface the magnitude of the electric field was identical but sign of the field changed.

The lower portion of Figure 8.11 shows the THz electric field and power spectrum from sample W2 under the identical patterned laser excitation. The emitted THz spectrum of sample W2 is also similar to the THz spectrum of the sample under focused line excitation in Figure 8.5. Some of the spectral peaks of W2 in Figure 8.5 under focused excitation are not present under the patterned excitation of Figure 8.11. The emitted THz power is maximized for the same positions of the laser patterns (on the air-dielectric interface) as sample W4. When the laser pattern is placed over the opposite air-hole edge of the crystal the electric field is also flipped as for sample W4.

Sample W2's spectral peaks are broader then the spectral peaks of sample W4. This is probably due to the slightly oblong shape W2's air holes and the over etching of sample W2 as discussed previously.

The peak spectral density of the modes is on the order of 10 percent of the peak spectral density of the emitted THz power from an unprocessed wafer. After the THz

is generated by the doped epilayer it will propagate for sometime in the photonic crystal slab where it will be highly absorbed by the doped epilayer. This also accounts for the broad peaks of the photonic crystal and the damping of the emitting THz electric fields after several picoseconds.

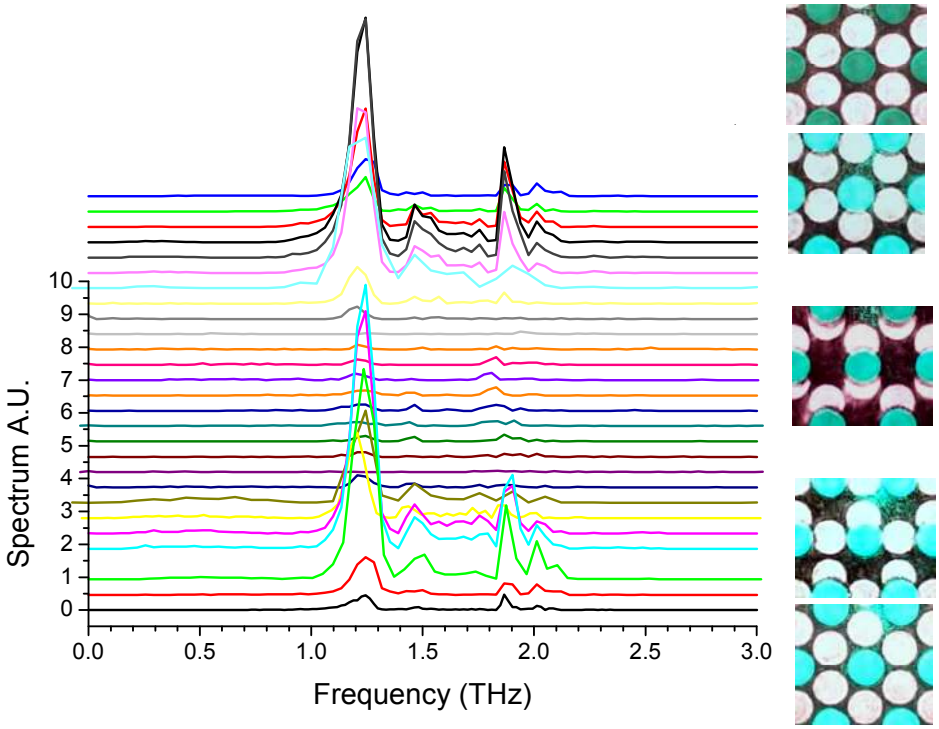


**Figure 8.12** Emitted THz spectra as the hexagonal mask pattern is moved in a vertical direction across the photonic crystal sample W4. The vertical component of the THz electric field is measured.

## *Attempt to couple into the hexapole mode*

One would expect different lattice patterns to couple into photonic crystals modes with different field distributions. In Figure 8.12 a hexagonal laser pattern is imaged onto sample W4 and the spatial dependence of the emitted THz radiation is

investigated. The hexagonal lattice pattern consists of two triangular lattices of circular spots displaced from one and other. In Figure 8.12 the vertical component of the emitted THz electric field is measured. When the hexagonal laser spots surrounded the photonic crystal the emitted THz power was minimized and approached zero. As the laser pattern was moved in a vertical direction so that some of the laser spots were over the air-dielectric interface the emitted THz power was maximized.

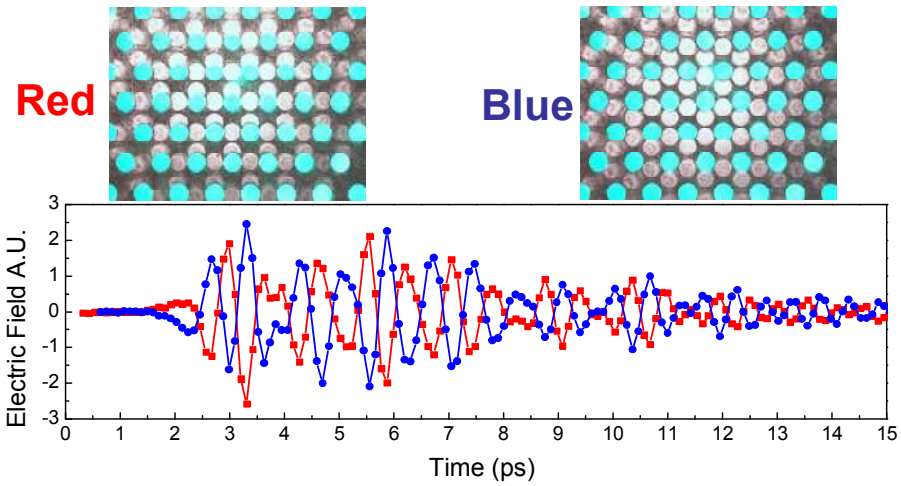


**Figure 8.13** The THz electric fields for the positions of the hexagonal laser pattern that maximizes the emitted THz in Figure 8.12.

The position of the spectral peaks from the hexagonal laser patterns was identical to the positions of the laser peaks from line laser pattern in Figure 8.11. This implies the hexagonal laser pattern was coupling into the same photonic crystal modes as the line laser pattern. This was unexpected one would expect to couple into different photonic crystal modes with laser patterns that have different symmetries. The modes appear to be concentrated along the air hole edges of the photonic crystal.

The emitted THz electric field was also investigated for the laser pattern positions where the emitted THz signal was maximized. Figure 8.13 shows the electric field at the positions of maximum signal in Figure 8.12. The sign of the THz electric field flipped when the laser pattern was over opposite air-dielectric interfaces. This was the same behavior that was found for the fields of the laser line pattern in Figure 8.11.

## *Photonic crystal field profiles*

At the Γ-point of the Brillion zone (were $k_{Bloch}$=0) the Bloch modes are periodic. They are the only modes a periodic laser excitation will couple to. However, having the same periodicity is not a sufficient condition for coupling THz radiation into photonic crystal modes. The generated THz electric field in the photonic crystal can be expressed as the sum of orthogonal photonic crystal modes. Thus for the generated THz to couple into a particular photonic crystal mode, the overlap integral of the generated THz field and the particular photonic crystal mode must be nonzero and preferably large. By changing the pattern, and the position of the femtosecond laser excitation, it should be possible to selectively couple between photonic crystal modes.

The lowest frequency modes of the photonic crystals were calculated using finite-difference time domain (FDTD) simulations (See Appendix F). For FDTD calculations of a photonic crystal slab, a broad frequency point source is placed in the slab. The electromagnetic waves in the simulation will experience constructive and

destructive interference. At long times only superposition of the photonic crystal modes will remain. The photonic crystal modes can be thought of as the resonances of the simulations. Fourier transforms can then be performed to find the mode field patterns. A dipole point source in time and space source will excite any mode, provided the point source is not placed at a field node.

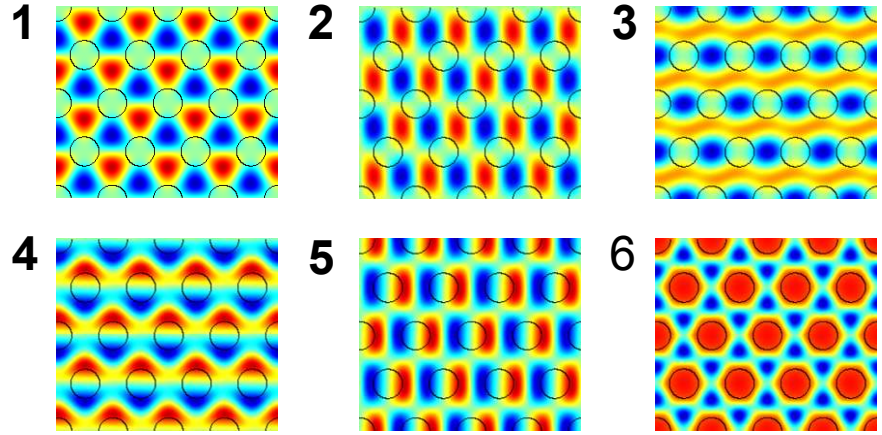


**Figure 8.14** $E_z$ component of the TM modes of a two-dimensional triangular photonic crystal with air hole radius r=.26*a*. The modes are labeled in order of increasing frequency. (color chart: red-positive blue-negative)

The computational grid of the FDTD simulation must terminate. In the plane of the slab periodic-Bloch boundary conditions can be used. Above and below the slab, electromagnetic wave must be able to radiate into free space. This can be accomplished by employing analytic or perfectly matched boundary conditions which absorbing all incident radiation without any reflections.

The FDTD method is accurate to $2^{nd}$ order and very robust. However this comes at the expense of large computational demands. As the gird spacing decreases the

time step will also decrease. If the grid spacing is reduced by a factor of two in all dimensions, the computational time will increase by a factor of 16 not by a factor of 8, since the number of time steps will also increase by a factor of 2.

In contrast to time domain calculations, frequency domain calculations are faster and more accurate. However they require periodic boundary conditions which are not present above and below a photonic crystal slab.

The modes of a three-dimensional photonic crystal slab are related to the modes of a two-dimension photonic crystal. Calculations for two-dimensional photonic crystal calculations are very fast. The modes of two-dimensional photonic crystal will have lower frequencies then its three-dimensional counterpart. However to first order the mode profiles will be the same and will be indiscernible to the eye. Thus two-dimensional photonic crystals can be used find the approximate modal patterns, and all of the degenerate modes. Later the information from the 2D calculations can be used in three-dimensional calculations to find the optimum position of the point source, and make sure that no modes are missed by the FDTD simulations.

The 2-D eigenmodes were calculated using the MIT-photonic bands software package[48]. The six lowest TM modes with at the Γ-point of a triangular two-dimensional photonic with air hole radius .26*a* are shown in Figure 8.14. THz radiation generated by the doped layer will only couple to the TM modes, since the generated THz electric field will be perpendicular to the plane of the photonic crystal. In Figure 8.14 the electric-field ($E_z$) perpendicular the photonic crystal is plotted. A "hot-cold" color chart is used. Blue refers to positive values of the electric field while

red indicates negative values of the electric field, and green is zero. The modes are labeled with numbers by ascending frequency. The lowest frequency mode (Mode 1) at the Γ - point has the symmetry of a hexapole. Modes 2 and 3 are degenerate quadrupole modes. Modes 4 and 5 are degenerate dipole modes, and mode 6 is a monopole mode.

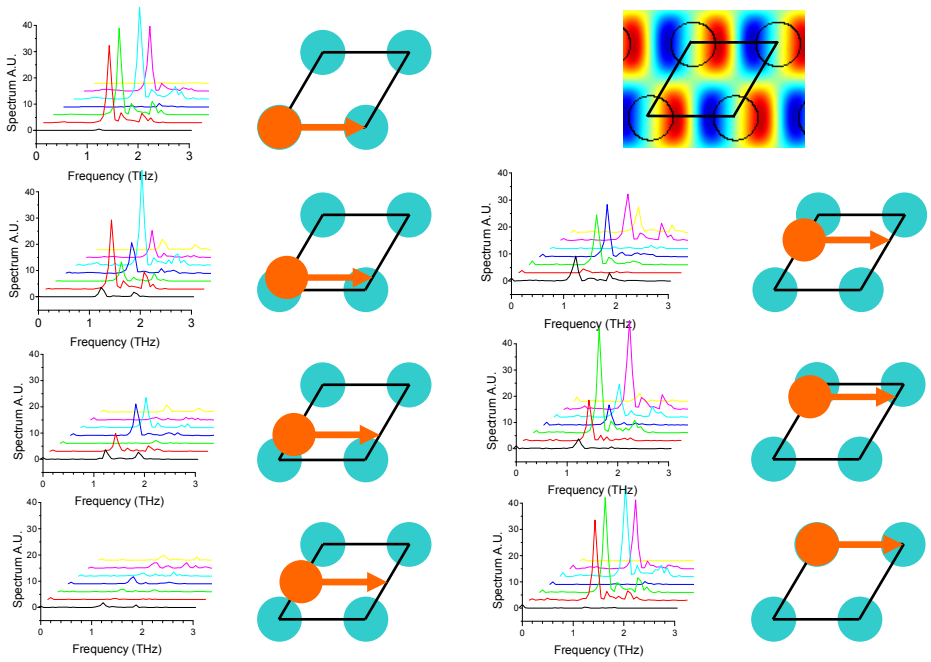


**Figure 8.15** The spectra of a triangular laser pattern spots scanned across the unit cell of sample W4. The upper right corner show the electric field profile of the horizontal dipole mode ( mode 5 in Figure 8.14) The horizontal component of the THz field is measured.

The degenerate dipole (mode 5) would have a large overlap integral with the line laser pattern excitation in Figure 8.11. If the line laser pattern was moved to the opposite side of the air hole it would couple into a region of the dipole mode having the opposite phase, but the same magnitude. One would expect to couple to the monopole with the hexagonal laser excitation of pattern in Figure 8.12. However

when the hexagonal laser pattern is positioned on the photonic crystal such that all of the laser spots are equidistant from the air hole the emitted THz power is minimized. No monopole mode is observed. The spectral peaks in Figure 8.12 correspond to the same dipole mode observed in Figure 8.11. When the hexagonal laser excitation is near the air hole edge the overlap integral of the hexagonal laser excitation and dipole mode 5 will be very large. This is same position where the emitted THz is maximized for the line pattern excitation in Figure 8.11.

### *Mapping out the photonic crystal modes over a unit cell*

To examine the spatial dependence of the photonic crystal modes in more detail, a triangular laser pattern of circular spots was used to map out the spatial profile of the photonic crystal modes. The lattice of the triangular laser pattern was identical to the photonic crystal lattice. Modes at the Γ point of the Brillion zone are periodic in the unit cell of the photonic crystal. Each unit cell of the photonic crystal will contain on circular laser spot. In the limit where the radius of the laser spot goes to zero the magnitude of the emitted THz field will proportional the magnitude of the photonic crystal mode at the laser spot. By rastering the triangular lattice pattern across the unit cell of the photonic crystal and recording the magnitude of the emitted THz radiation, one should be able to directly measure the spatial profile of the mode. This is impractical through, since as the size of the laser spot is reduced, the emitted THz signal is also reduced. Greater demands will also be placed on the image of the laser

excitation. In practice the laser excitation will never have the exact period of the photonic crystal, and astigmatism from the spherical lens will always be present.

To map out the modes' field distributions with a sufficient signal to noise ratio, a triangular lattice pattern of circular laser spots of with a radius of .25*a* was used. This will not allow the exact spatial profile of a mode to be found, but it will give a general idea of the mode's profile.

The unit cell was divided into a grid and a triangular coordinate system was used to determine the position of the laser spots. At each point in the grid a scan of the THz electric field was taken. The grid consisted of a 7x7 array of points.

Figure 8.15 show plots of the power spectrum of the emitted THz along each row of the 7x7 grid of the unit cell. In Figure 8.15 the ZnTe crystal is rotated to detect the horizontal component of the emitted THz electric field. The horizontal dipole mode (mode 5 in Figure 8.14) is shown in the upper right hand corner of Figure 8.15.

The spatial dependence of the large peak near 1.2 THz is seen to approximately match the spatial profile of the horizontal dipole in Figure 8.14. The smaller peak near 1.9 THz is also seen to approximately match the mode profile of the horizontal dipole mode. The magnitude of the peak at 1.9 THz increases with magnitude of the peak at 1.2 THz. The mode at 1.9 THz is most likely a higher order vertical mode of the planar horizontal dipole. A higher order vertical mode has a node in the center

plane of the photonic crystal. No peaks that can be attributed to hexapole, quadrupole, and monopoles are observed.

The triangular laser pattern was also scanned across the photonic crystal's unit cell with vertical component of the electric field measured. The magnitudes of the spectral peaks as a function position were consistent with mode profile of the vertical dipole mode (mode 5 in Figure 8.14).

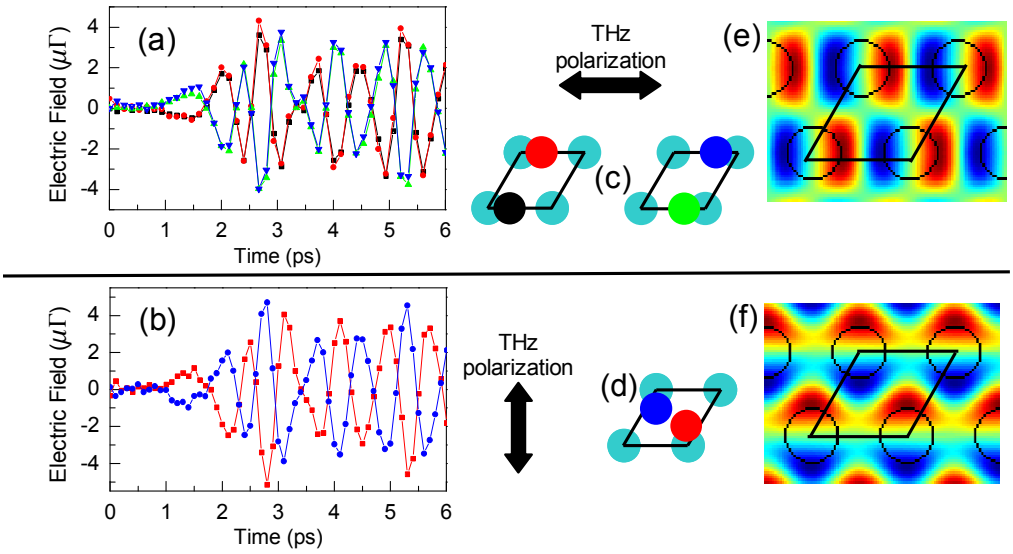


**Figure 8.16** Sample W4. Horizontal (a) and vertical (b) components of the emitted THz electric field with a triangular laser pattern. The unit cell diagrams indicate the positions of the laser pattern for horizontal (c) and vertical (d) polarizations, relative to the photonic crystal's air holes. The colored spots in (c) and (d) correspond to the positions at which the data of the same color were taken. (e) and (f) show FDTD calculated $E_z$ fields of the degenerate dipole modes (color chart: red-positive blue-negative**).**

## *Measuring the phase of the photonic crystal modes*

The emitted THz electric field can be examined to determine the relative phase of the mode the patterned laser excitation is coupling to. Figure 8.16 shows the emitted

THz electric fields for various positions of the laser spot in the unit cell. (The triangular laser pattern was used in Figure 8.16). In the upper portion of Figure 8.16 the horizontal polarization of the emitted THz electric field is measured, while in the lower portion of Figure 8.16 the vertical component of emitted THz electric field is measured.

The positions where the THz electric fields were taken is indicated by the matching colors of the plotted fields and the colored "laser" spots in the cartoons of the unit cells. For example, in lower half of Figure 8.16 one of the plotted THz electric fields is red. The red circle in Figure 8.16 (d) indicates where the red field plotted in Figure 8.16 (b) was taken with respect to the photonic crystal. For both polarizations the changes in sign of the emitted electric field are consistent with the changes in sign (or phase) of the horizontal and vertical dipole modes.

### *Stripe laser pattern - TM modes*

The dipole modes are the only modes that the laser pattern is observed to couple too. Attempts to couple to and observe the hexapole, quadrupole, and monopole modes were unsuccessful. The emitted THz radiation was always maximized when the laser pattern was near the air-dielectric interface of the air-holes. It may be objected that the emitted THz radiation does not arises from TM photonic crystal modes diffracted out of the slab, but an edge effect.

One plausible example of an edge effect would be coupling to the TE modes from laser absorption at the edge of the photonic crystal. If the laser pattern overlaps

the air hole edge, photo-generated carriers created at an upper air-hole edge within 2$\mu$m of the vertical surface will be accelerated in the plane of the slab by the depletion field. (The depletion field will always be normal to the surface). This would initiate plasma oscillations that only couple THz radiation into the TE modes

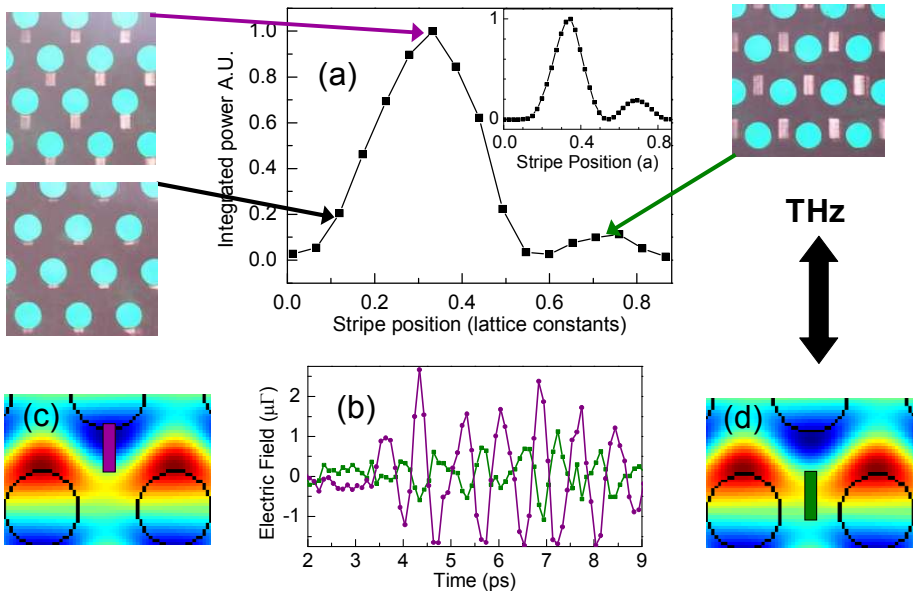


**Figure 8.17** Sample W4 (a) Spectral power of the peak at 1.2 THz as function of the position of the stripe laser pattern position. Insert shows the calculated spectral power from the dipole mode as a function of position. (b) The THz electric field (purple/green) at the (maximum / local maximum) of part (a). (c) and (d) E*z* component of the dipole mode showing the position of THz electric fields - purple/maximum (green/local maximum) - in part (b).

of the photonic crystal. It would also explain why the signal is maximized when the laser excitation is near the air-hole edge.

To confirm that the modes do not originate solely from the air-dielectric interface, a triangular lattice of thin stripes is moved across the air-hole dielectric interface as shown in Figure 8.17. The integrated spectral peak is then measure as a

function of the position of the laser stripe. If the emitted THz radiation originated from the air-hole interface, one would expect the integrated signal to remain constant as the laser stripe is move across the sample, and then rapidly fall to zero as the laser strip is moved off the air hole. If the signal originates only from the air-dielectric interface, the signal would be expected to rapidly disappear as soon as the thin stripe moves off the air-hole edge. However this is not observed in Figure 8.17.

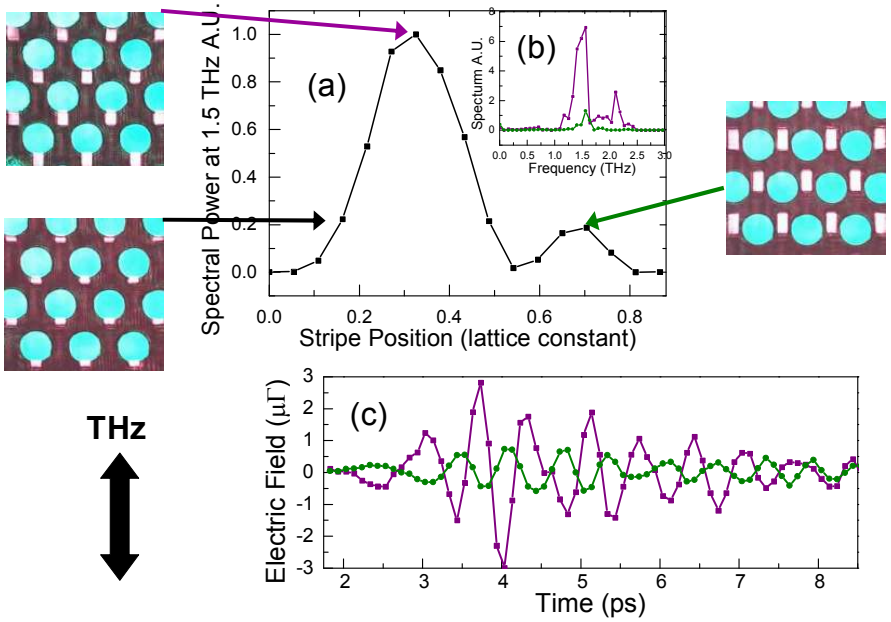


**Figure 8.18** Sample W2 (a) Spectral density at 1.5 THz as a function of the position of the stripe laser pattern. (b) Insert: as the stripe laser pattern moves away from the air holes the spectrum sharpens (c) The THz electric at the (maximum / local maximum) positions of part (a).

The integrated power of the dipole peak slowly increases and then decreases as the strip is moved across the air-hole edge. A small 2nd peak is also observed when the laser stripe is far away from the air hole edge. This 2nd peak is consentient with FDTD field calculations of the vertical dipole mode. At the location of the 2nd peak,

the phase of the mode is opposite to the phase of the mode at the 1st peak. The THz electric field at the 2nd peak in Figure 8.17 has an opposite sign as the THz electric field at the 1st peak.

This behavior is also shown in Figure 8.18 for sample W2. In Figure 8.18 the peak spectral density at 1.5 THz is plotted instead of the integrated peak power. For W2 the width of the spectral peak decreases when the laser stripes move away from the air holes. This seems to indicate roughness from the air holes plays a role in broadening the main peak in the spectrum of sample W2. The THz electric field also changes sign when the laser stripe pattern is over regions of the vertical dipole with different phase. (The decrease in noise in Figure 8.18 is due to using a long time constant for the lock-in amplifier.)

## *Far-field radiation patterns*

The hexapole, quadrupole, and monopole modes (modes 1, 2, 3 and 6 in Figure 8.14) are not present in any emitted THz spectra. In order for THz radiation to be detected, it must be collimated and refocused onto the ZnTe wafer. Free space electro-optic sampling measures the THz electric field that overlaps the femtosecond probe beam. The probe beam is slightly focused, so that only the peak spatial electric field is sampled. If the THz spot on the ZnTe crystal is not diffraction-limited, the peak spatial electric field will be decreased along with the electro-optic signal. In order to obtain a diffraction limited spot size, the spatial distribution of the THz electric field between the collimating and refocusing mirrors should be have a

gaussian profile. A non-optimal spatial distribution of the emitted THz radiation will result in a diminished signal or possibly none at all.

The far-field patterns of the emitted photonic crystal modes were investigated using the surface equivalence theorem[49]. The surface equivalence theorem enables the far-field radiation pattern to be calculated from the near-field tangential fields above the photonic crystal slab. In the Fraunhofer limit the far-field radiation pattern can be found by taking the Fourier transforms of the tangential fields.

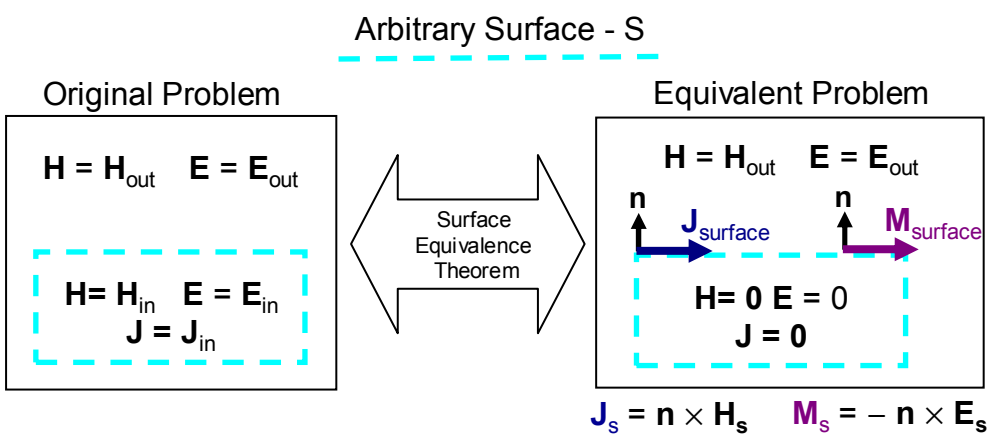


**Figure 8.19** The surface equivalence theorem. The electric and magnetic fields outside the arbitrary surface S are same, if the sources and field inside the arbitrary surface are replaced by surface current that are determined by the fields on the surface

Figure 8.19 shows a schematic of the surface equivalence theorem. If there are no current sources outside an arbitrary surface S, then the electric and magnetic fields outside the surface S are equal to the fields generated by surface currents ($\mathbf{J}_s$, $\mathbf{M}_s$) on the arbitrary surface. The surface currents do not exist, but the fields outside the surface can be envisioned as arising from the fictitious surface currents. The surface

currents produce an equivalent problem that is identical to the original problem outside the arbitrary surface. The magnetic and electric fields on the arbitrary surface ($\mathbf{H}_s$, $\mathbf{E}_s$) determine the fictitious surface currents.

$$\begin{aligned} \mathbf{J}_s &= \mathbf{n} \times \mathbf{H}_s \\ \mathbf{M}_s &= -\mathbf{n} \times \mathbf{E}_s \end{aligned} \tag{8.1}$$

Once the current source of the equivalent problem are known the fields outside the arbitrary surface may be found be found from the retarded vector potential

$$\mathbf{A}(\mathbf{r},t) = \frac{1}{4\pi r}\int_S (\mu \mathbf{J}_s + \varepsilon \mathbf{M}_s) e^{ikr} dS \tag{8.2}$$

where $k$ is the wave number of the light and $r$ is magnitude of the distance from a point to on the surface S. In general the vector potential will be a complicated function of the surface currents and by extensions the electric and magnetic field at the surface. In some sense the surface equivalence theorem is a version of Huygens's principle if the arbitrary surface is thought of as a wave front.

For the photonic crystal slab the arbitrary surface can be dawn to encompass two planes that are above the slab and parallel to it. The planes can be thought of as being very long. Contributions from the ends of the surface can be neglected. This leaves only two planes from which to calculate the vector potential. The problem can be further simplified to a single plane using image theory. The region of the problem can be divided in two along the center plane of the photonic crystal. For the even TE-like modes one the two identical regions can be replaced with a PMC material (perfect

magnetic conductor) without changing the fields in the other region. For the odd TM-like modes one of the two regions can be replaced with a PEC material without changing the field in the other region. Thus there is another equivalent problem, consisting of half of the original problem and PEC material. The fields in the PEC region are zero, thus the vector potential can be found using the surface fields in one

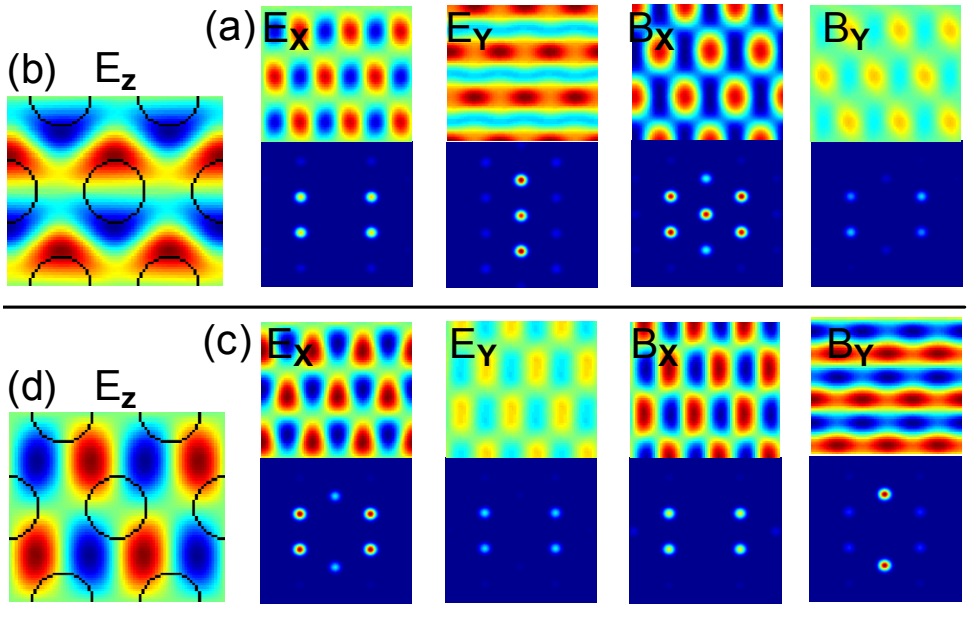


**Figure 8.20** (a) Tangential fields of the dipole mode in a plane above of the photonic crystal slab along with their apodized Fourier transforms. (b) $E_z$ field of dipole mode in the photonic crystal slab. (c) Tangential fields and Fourier transforms of a quadrupole mode (d) $E_z$ field of the quadrupole mode.

plane above or below the photonic crystal.

In the Fraunhofer limit, the far-fields may be found by taking Fourier transforms of the tangential fields. The two-dimensional Fourier space of the transforms will consist of the $k_x$ and $k_y$ wave vector components of the emitted fields. The $k_z$

component can be found using the free space dispersion relation ($\omega^2 = c^2\mathbf{k}^2$), if $k_x$ and $k_y$ are known. If $k_x^2 + k_y^2$ is greater then $|\mathbf{k}|^2$ then $k_z$ will be imaginary. A light circle ($\omega^2 = c^2 k_{//}^2$) will exist on the Fourier space centered at $k_x = 0$, $k_y = 0$. Fourier components beyond the light circle will be evanescent waves in free space. Radiation in the forward direction will result if there is a large Fourier component at $k_x = k_y = 0$. Points below the light circle not at $k_x = 0$ and $k_y = 0$ will correspond to angled emission.

The two-dimensional Fourier transforms of the hexapole, quadrupole, and dipoles were calculated in a plane above the photonic crystal slab. It was found that only the dipole modes had $k_x = 0$ and $k_y = 0$ components. Thus the dipole modes are the only modes that will radiate in the forward direction normal to the slab.

The dipole modes have their field anti-nodes near the edge of the air hole, while the hexapole and quadrupole modes have their anti-nodes away from the air-dielectric interface. The air-dielectric interface can be thought of as strongly scattering the modes. The dipole modes are scattered since an appreciable fraction of the dipole mode is concentrated near the air-dielectric interface. The hexapole, quadrupole and monopole modes do not experience strong scattering since their modes are concentrated away from the dielectric interface.

# Appendix A Alignment of the electro-optic sampling setup

Careful thought and attention should be put into the alignment of the THz and laser beams in free space electro-optic sampling. There are several factors that can make the alignment for THz free space electro-optic sampling difficult. However, by following the procedures outline in this section and having a basic understanding of the principals involved, the alignment can be done quickly and efficiently.

THz radiation is invisible and cannot be seen with IR cards. However the pump beam can be used for as a rough alignment beam. Provided it is properly aligned. The time duration of the THz pulse will be on the order of 1 picosecond. Two light pulses that are separated by 1 picosecond in time will be separated by 300 $\mu$m in space. The path of probe beam, and the pump and THz beams may be on the order of a hundred of centimeters. The THz and probe must overlap in time for a signal to be measured. A careful layout and planning of the position of the beams will facilitate finding the zero delay point. This will reduce the amount time spent scanning for it and facilitate. Another alignment difficulty is tweaking up the signal. If the probe and THz do not arrive at the ZnTe receiver at the same time no signal will be present. By changing the parabolic mirrors one can increase the collected

THz while decreasing the signal if the time delay between the probe and THz pulse is changed.

### *Finding the zero time delay point of the probe and THz*

Free space electro-optic sampling is a time-resolved measurement. To observe a signal the THz pulse and laser probe pulse must not only spatially overlap each other in the ZnTe crystal, but must arrive at the same. The path length of the THz and laser beams may be on the order of a 10 or 100 cm while the duration of the THz pulse will be on the order of 100 $\mu$m.

A lot of time can be wasted scanning the delay probe to make the probe and pump/THz beam paths equal. To minimize scanning time, the probe beam and pump/THz beams should travel over the threaded holes on the optical table whenever possible. This will enable an initial estimate of the path lengths of the probe beam, and the pump/THz. Aligning beams over the optical table's hole also aids in placing optical components (lens, waveplate, and apertures) in the beam path. The post holders for such components can be screwed directly into the holes on the optical table. No horizontal translation of the components will be necessary. The purge box was machined to have its' holes directly over the holes of the optical table.

The height of the beams should also be constant. If the height is not constant the polarization of the laser beams may change. Beams that are not level will also add extra path length to the beam line, and throw of the estimate of the path length. If the THz beam is not at the right height the parabolic mirrors will introduce astigmatism.

A reference aperture attached to a post, post holder, and standing base should be used to set the height of the laser beams. The height of the reference aperture should be set with a ruler. Once it is set, it should never be changed. All of the laser beams will be referenced to the reference aperture's height. A wide rectangular base should be used to mount the post holder of the reference aperture. The user can place the two outer slots in the standing base over the holes in the optical table. This will allow the user to slide the reference aperture directly over a hole in the optical table. The reference aperture will also be used to align laser beams over the holes in the optical table. The bottom plate of the purge box is one inch high. Two reference apertures will have to be used one for inside the purge box and one for outside the purge box. The beam outside the purge box should be set at 5.5 inches - this is the distance from the center of the purge boxes windows to the surface of the optical table. The reference aperture for inside the purge box should then be set for 4.5 inches.

## *Aligning the probe beam*

The alignment of probe beam should be the first thing that is done. Either the probe pulse or the THz pulse will have to be moved so they will spatially overlap one and other inside the ZnTe crystal. The probe beam will also have to be aligned for the optical bridge after it traverses the ZnTe crystal. For this reason the probe beam should first be aligned for the optical bridge. Afterwards the probe beam should never be moved again. Later the position of the THz spot in the ZnTe is moved to overlap the probe beam. The probe beam should be aligned with the holes on the

floor of the probe box. The laser should run through the center of the hole drilled in the 2nd parabolic mirror. If it is not, the parabolic mirror should be moved. Often the probe will clip the drilled hole in the parabolic mirror which will lead to a reduction in the signal. The user should also make sure the ZnTe crystal is centered on the probe beam. The user must then make sure the probe beam runs is running through the quarter waveplate and the polarizing beamsplitter. When the ZnTe crystal is rotated the position of the probe will often change. The user should make sure that the laser beam is centered on the fiber optic lens couplers in both arms of the optical bridge. A beam block should be placed in one arm of the photodiode bridge. The output of the detector will then be the signal in the other arm of the photodiode instead of the difference between the signals in each arm. The coupling of the probe beam into the optical fiber is very sensitive to any changes in the laser beam, and the tilt of the lens couplers. The knobs on the mirror mounts that control the tilt of the fiber optic lens couplers will have to be readjusted often. The 'sweet spot' of the tilt alignment is very sharp. The user should make sure they are not stuck on a local maximum of alignment. Once the signal from one arm of the photodiode is peaked up, the procedure should be repeated with the other arm.

### *Balancing the optical bridge*

During the alignment of the quarter waveplate should be normal to the probe beam. The optical bridge is balanced by rotating the quarter waveplate. The waveplate is a zero order quarter waveplate for 770nm light. Both arms of the optical

beam should be unblocked. The output of the detector is then the difference in signal between the two arms. The quarter waveplate should then be titled about the axis of the probe beam until the signal is nulled. Often it will not be possible to null the signal in the two arms. This may be because the waveplate is a zero order quarter waveplate for 780nm light and the center wavelength of the laser pulse is 790nm. To null the signal and for finer adjustments the quarter waveplate can be rotated about the axis of the post.

## *Aligning the parabolic mirrors*

The two parabolic mirrors collect the THz radiation from the emitter, collimate and focus it onto the ZnTe crystal. The position of the parabolic mirror is important, if the emitter is not at the focus of the first parabolic mirror, the THz beam will not be properly collimated. This will lead to astigmatisms and a larger spot size when the 2nd parabolic mirror focuses the THz radiation onto the emitter. The parabolic mirrors are electroplated Ni on a paraboloidal surface. Each mirror is attached to mirror mount with vertical and horizontal tilt control. The mirror mounts are attached to a xyz stage with micrometers. Each parabolic mirror has 5 degrees of freedom. Some advocate a THz optical system with solid parabolic mirrors on set height mounts. It reduces the degrees of freedom in the system. I have not used such a setup for electro-optic detection. However it appears to me that peaking up a signal once it is found would be difficult. It is my belief that parabolic mirrors with a

limited number of degrees of freedom controlled by micrometers are necessary obtaining the best alignment.

The first parabolic mirror adjust to be made is to position the posts that hold each parabolic mirror over the same line form by the holes in the optical table. The alignment will have to be eyeballed. A straight ruler held vertically can aid in the alignment. The parabolic mirrors will be move with what I will refer to as the x micrometer. Once the x micrometer adjustment is made, the x-micrometer will not be moved again.

There is a drilled hole in each parabolic mirror. The diameter of the hole is 1/8 inch. The mirror holes allow a laser beam to go through the parabolic mirror and travel collinear with THz radiation. The mirror holes are drilled at the place where a ray from the mirror's focus makes a right angle when it is reflected. Both mirror holes are used for the initial placement of the parabolic mirrors. The y and z micrometer should be adjusted so an aligned laser passes through the center of the mirror hole. For the 2nd parabolic mirror the probe beam can be used. For the 1st parabolic mirror an external alignment laser, or the pump beam can be used.

THz radiation is invisible and the pump laser beam can be used as a crude substitute for the THz radiation. The power of the pump beam should be turned down and the user should use safety goggles. A beam block should be placed in front of the optical bridge so pump beam does not damage the photodiodes. The pump beam must be level, at the correct height, and aligned with the optical table's holes. If the pump beam is not focused down on the emitter with a lens, a short focal length lens should

be place in the beam path so the focus is approximately where the THz will beam will created. The dispersed optical beam can be seen with an IR card. The IR card should never be tilted upwards. Its' laminated coating specularly reflects the laser. If the IR card is put in the beam path after the collecting parabolic mirror, the image of the mirror hole should be visible. The knobs which control the mirror's tilt can be used to adjust the beam at farther downstream from the mirrors. The IR card should be placed directly after the focusing parabolic mirror. The mirror hole from the focusing parabolic mirror should be visible. If it is not, the beam is not hitting the center of the focusing parabolic mirror. The tilt of the collecting parabolic should then be adjusted with the IR card placed after the focusing mirror. The IR card should then be placed in front of the ZnTe receiver. The probe beam and pump beam should overlap one and other. The focus of the pump will not be sharp. To distinguish between the two beams the user can block and unblock the pump beam. If the two beams do not overlap, the tilt of the focusing mirror can be adjusted to bring the two beams together. After this step the probe beam should be checked to make sure it runs through the center of the focusing mirror's hole. If it does not, the y z micrometers of the focusing mirror will have to be readjusted. The pump beam spot will have to be placed over the probe beam spot again using the tilt controls of the focusing mirror. Once alignment of the parabolic mirrors is complete, the emitter is placed in the setup.

### *Peaking up the signal*

The path length of the pump and probe must be made equal to find a signal. A retro reflector placed on a delay line changes the time delay of the probe beam. The delay line consists of two translation stages on top of one and other. The lower stage has a motorized screw with a travel range of 25mm. The upper stage has manual micrometer with a range of 50mm. The retro reflector must be scanned until a signal is found at the zero delay point. An optical component placed in the beam path changes the path length and the time delay. The zero delay point of the retro reflector will change when different emitters are used. The probe beam travels to and from the retro reflector. If the position of the retro reflector is moved by a given amount the path length will increase be twice that amount. If the retro reflector is scanned over a large distance the optical bridge become unbalanced. The fiber coupled lens should then be readjusted and the optical bridge should be rebalanced.

Once the signal is found, it can be peaked up by changing the positions of parabolic mirrors. However the path length of the THz beam will change as the parabolic mirrors are moved. The electric field in the ZnTe will be increased from improved alignment, but the signal will decrease if the time delay changes. This problem can be circumvented by moving the motorized screw with the back and forward buttons on the Newport motion controller while looking at the signal. The velocity of the stage must be set slow enough so the lock-in has time to respond to changes in the signal. Otherwise the lock-in will average over the signal, and the maximum signal will be reduced. The x micrometer position of the parabolic mirrors

will not have to be adjusted. Unless the initial alignment is poor the time delay will not change by much when the parabolic mirrors are adjusted in the z position. However moving the parabolic mirror with the y-micrometer will significantly change the time delay. After the y-micrometer is moved the user will have to find the new zero point again where the signal is a maximum. A rule of thumb for aligning the parabolic mirrors is to move the micrometers in increments of 150 $\mu$m, and look to see if the signal has decreased, or increased. The use should keep moving the micrometer until the signal has decreased and then go back to the maximum position. The ZnTe receiver is on a translation stage that moves towards and away from the focusing parabolic mirror. As the micrometer on this translation stage is move the time delay of the signal will not change by much. A rule of thumb is to move this micrometer in increments of 1mm. The optimal position of the ZnTe receiver with respect to the focusing mirror will be dependent on the THz emitter position with respect to the collimating parabolic mirror. The user may the optimum position of the ZnTe receiver out of the range of the stage's micrometer. The base plate of the ZnTe receiver on the translation stage will then have to be moved. The simplest alignment procedure would be to adjust the y and z micrometers on the collecting parabolic mirror and then adjust the micrometer of the ZnTe receiver.

## *Adjusting the position of the chopper*

It was found that a 25/30 slot chopper blade running at 2 KHz would produce a significant amount of sound and strong accompanying air current. Limited space on

the optical table made it necessary to place the chopper near the optics. The vibrations and air current from the chopper would sometimes lead to spurious signals. This was especially true for a pellicle beam splitter that was used initially to make the probe and THz beams collinear. For this reason the pellicle beam splitter was abandoned and small holes were drilled into the parabolic mirror. It was found the air currents and vibrations would be eliminated if the blade was run at a lower angular velocity with a 100 slot blade. However the beam size was on the same order of the holes in the chopper blade. The thickness of the chopper blade was not negligible. If the blade was slightly tilted the lock-in would be reduced as a smaller amount of the pump beam would be modulated. The position of the chopper blade had to be optimized for the maximum pump modulation and greatest lock-in signal. First the retro reflector would be moved to the position of highest signal. The screws attaching the chopper to the optical table would then be slightly unfastened while the chopper was moved and rotated to maximize the signal on the lock-in. Sometimes this would have a dramatic increasing the maximum signal by almost a factor of two.

# Appendix B THz generation from <111> zinc blende crystals.

For optical rectification, the THz polarization dependence on the optical pump laser polarization and the crystals orientation will be derived. The Kleinman symmetry can be stated as

$$\chi^2_{ijk}(\omega_3 = \omega_2 + \omega_1) = \chi^2_{kji}(\omega_3 = \omega_2 + \omega_1) \tag{B.1}$$

The Kleinman symmetry condition will be assumed to be valid. Technically this is not true, since the crystal is not lossless. But it will make the problem more manageable and gives the right answer. The frequency dependence of the susceptibility tensors will be ignored for this derivation.

With the Kleinman symmetry condition (B.1), contracted notation can be employed to simply the calculations. Defining $d_{ijk} \equiv (1/2)\chi_{ijk}$ one can write the 2nd order polarization term as

$$P_i^2(\omega_{THz} = \omega_n + \omega_m) = \sum_{jk}\sum_{mn} 2d_{ijk}E_j(\omega_n)E_k(\omega_m) \tag{B.2}$$

where the sum $\omega_n + \omega_m$ is fixed though out the *mn* summation. If *j* and *k* are interchanged $d_{ijk}$ is invariant from (B.1). A new notation can then be introduced

where $j$ and $k$ are replaced by a single index $l$ with 6 independent values. The corresponding $l$ index for each pair of $j, k$ indices is shown in the table below.

| $j, k$ | 1,1 | 2,2 | 3,3 | 2,3  3,2 | 3,1  3,1 | 1,2  2,1 |
|---|---|---|---|---|---|---|
| $l$ | 1 | 2 | 3 | 4 | 5 | 6 |

With the contracted notation $l$, equation (B.2) may be written in a matrix form as

$$\begin{pmatrix} P_x \\ P_y \\ P_z \end{pmatrix} = 2 \begin{pmatrix} d_{11} & d_{12} & d_{13} & d_{14} & d_{15} & d_{16} \\ d_{21} & d_{22} & d_{23} & d_{24} & d_{25} & d_{26} \\ d_{31} & d_{32} & d_{33} & d_{34} & d_{35} & d_{36} \end{pmatrix} \begin{pmatrix} 2\,E_x(\omega_1)E_x(\omega_2) \\ 2\,E_y(\omega_1)E_y(\omega_2) \\ 2\,E_z(\omega_1)E_z(\omega_2) \\ E_y(\omega_1)E_z(\omega_2)+E_z(\omega_1)E_y(\omega_2) \\ E_x(\omega_1)E_z(\omega_2)+E_z(\omega_1)E_x(\omega_2) \\ E_x(\omega_1)E_y(\omega_2)+E_y(\omega_1)E_x(\omega_2) \end{pmatrix} \qquad \text{(B.3)}$$

The sum $\sum_{nm}$ has been neglected. Only the nonlinear polarization from two frequency components will be calculated.

The coordinates of (B.3) are in the basis of the crystal's coordinate system ($x, y, z$). A more convenient basis is the lab coordinates $x_{lab}, y_{lab}, z_{lab}$ shown in Figure 5.1. Let $\mathbf{x}_{lab}, \mathbf{y}_{lab}, \mathbf{z}_{lab}$ be the unit vectors of the lab coordinates. The unit vector $\mathbf{z}_{lab}$ is normal of the plane of the GaAs wafer while the unit vectors ($\mathbf{x}_{lab}$ and $\mathbf{y}_{lab}$) lie in the plane of the GaAs wafer. Let $\mathbf{x}_{lab}$ be parallel to a <110> in-plane direction and $\mathbf{y}_{lab}$ be parallel to a <112> in-plane direction such that $\mathbf{x}_{lab} \cdot \mathbf{y}_{lab} = 0$ and

$\mathbf{x}_{lab} \times \mathbf{y}_{lab} = \mathbf{z}_{lab}$. In the crystal coordinate system $x, y, z$ the lab unit vectors $\mathbf{x}_{lab}, \mathbf{y}_{lab}, \mathbf{z}_{lab}$ can be written as

$$\begin{aligned} \mathbf{x}_{lab} &\equiv \left( \frac{-1}{\sqrt{2}} \quad \frac{1}{\sqrt{2}} \quad 0 \right)_{crystal\ cordinates} \\ \mathbf{y}_{lab} &\equiv \left( \frac{-1}{\sqrt{6}} \quad \frac{-1}{\sqrt{6}} \quad \frac{2}{\sqrt{3}} \right)_{crystal\ cordinates} \\ \mathbf{z}_{lab} &\equiv \left( \frac{1}{\sqrt{3}} \quad \frac{1}{\sqrt{3}} \quad \frac{1}{\sqrt{3}} \right)_{crystal\ cordinates} \end{aligned} \tag{B.4}$$

If the same point has coordinates $\left(x_1 \quad y_2 \quad z_3\right)$, and $\left(x_{1lab} \quad y_{2lab} \quad z_{3lab}\right)$ in the crystal and lab bases respectively, then the coordinates are related by the following unitary matrices

$$\begin{aligned} \begin{pmatrix} x_1 \\ y_2 \\ z_3 \end{pmatrix} &= \begin{pmatrix} \mathbf{x}_{lab}^T & \mathbf{y}_{lab}^T & \mathbf{z}_{lab}^T \end{pmatrix} \begin{pmatrix} x_{1lab} \\ y_{2lab} \\ z_{3lab} \end{pmatrix} \\ \begin{pmatrix} x_{1lab} \\ y_{2lab} \\ z_{3lab} \end{pmatrix} &= \begin{pmatrix} \mathbf{x}_{lab} & \mathbf{y}_{lab} & \mathbf{z}_{lab} \end{pmatrix} \begin{pmatrix} x_1 \\ y_2 \\ z_3 \end{pmatrix} \end{aligned} \tag{B.5}$$

The femtosecond laser beam's wave vector is parallel to $z_{lab}$. The electric field of the near infrared (NIR) femtosecond laser beam $\mathbf{E}_{NIR}$ will be in the plane of the GaAs wafer and can be expressed in terms of $\mathbf{x}_{lab}$ and $\mathbf{y}_{lab}$ as

$$E_{NIR}(\theta) = E_{NIR}\left(\cos\theta\, \mathbf{x}_{lab} + \sin\theta\, \mathbf{y}_{lab}\right) \tag{B.6}$$

We would like to find the dependence of the THz polarization in the $x_{lab}$, $y_{lab}$, $z_{lab}$ basis on the angle $\theta$. This will involve a coordinate transformation between the $x_{lab}$, $y_{lab}$, $z_{lab}$ basis and the crystal basis.

To find the THz polarization $E(\theta)$ in the crystal basis equation (B.5) is used with (B.6)

$$\begin{pmatrix} \frac{1}{6}\left(2+\cos 2\theta+\sqrt{3}\sin 2\theta\right)E_{NIR} \\ \frac{1}{6}\left(2+\cos 2\theta-\sqrt{3}\sin 2\theta\right)E_{NIR} \\ \frac{2\sin^2\theta}{3}E_{NIR}E^2 \\ \frac{2}{3}\sin\theta\left(\sqrt{3}\cos\theta-\sin\theta\right)E_{NIR} \\ \frac{-2}{3}\sin\theta\left(\sqrt{3}\cos\theta+\sin\theta\right)E_{NIR} \\ \frac{-1}{3}\left(1+2\cos 2\theta\right)E_{NIR} \end{pmatrix} = \begin{pmatrix} \frac{-1}{\sqrt{2}} & \frac{-1}{\sqrt{6}} & \frac{1}{\sqrt{3}} \\ \frac{1}{\sqrt{2}} & \frac{-1}{\sqrt{6}} & \frac{1}{\sqrt{3}} \\ 0 & \frac{2}{\sqrt{3}} & \frac{1}{\sqrt{3}} \end{pmatrix} \begin{pmatrix} E_{NIR}\cos\theta \\ E_{NIR}\sin\theta \\ 0 \end{pmatrix} \qquad \text{(B.7)}$$

For the zinc blende class of crystals the only nonzero components of the tensor $d_{ij}$ are $d_{14}$, $d_{25}$, and $d_{36}$. All three components $d_{14}$, $d_{25}$ and $d_{36}$ can be shown to have the same value for the zinc blende class. The values of the 2nd order nonlinear polarizations which produce the THz radiation can be found by substituting the optical electric field (B.7) in the crystal basis into the expression for the 2nd order nonlinear term (B.3).

$$\begin{pmatrix} P_{xTHz} \\ P_{yTHz} \\ P_{zTHz} \end{pmatrix}_{crystal\ axis} = \begin{pmatrix} d_{14}\frac{2}{3}\left(\sqrt{3}\cos\theta - \sin\theta\right)\sin\theta \\ d_{14}\frac{-2}{3}\left(\sqrt{3}\cos\theta + \sin\theta\right)\sin\theta \\ d_{14}\frac{-1}{3}\left(1 + 2\cos 2\theta\right) \end{pmatrix} =$$

$$\begin{pmatrix} 0 & 0 & 0 & d_{14} & 0 & 0 \\ 0 & 0 & 0 & 0 & d_{14} & 0 \\ 0 & 0 & 0 & 0 & 0 & d_{14} \end{pmatrix} \begin{pmatrix} \frac{1}{6}\left(2 + \cos 2\theta + \sqrt{3}\sin 2\theta\right)E_{NIR}^2 \\ \frac{1}{6}\left(2 + \cos 2\theta - \sqrt{3}\sin 2\theta\right)E_{NIR}^2 \\ \frac{2\sin^2\theta}{3}E_{NIR}^2 \\ \frac{2}{3}\sin\theta\left(\sqrt{3}\cos\theta - \sin\theta\right)E_{NIR}^2 \\ \frac{-2}{3}\sin\theta\left(\sqrt{3}\cos\theta + \sin\theta\right)E_{NIR}^2 \\ \frac{-1}{3}\left(1 + 2\cos 2\theta\right)E_{NIR}^2 \end{pmatrix} \tag{B.8}$$

The components of the polarization will then be in the crystals axis and must be multiplied by $\begin{pmatrix} \mathbf{x}_{lab}^T & \mathbf{y}_{lab}^T & \mathbf{z}_{lab}^T \end{pmatrix}^{-1}$ to transform the polarization coordinates into the lab coordinate system

$$\begin{pmatrix} P_{x_{lab}THz} \\ P_{y_{lab}THz} \\ P_{z_{lab}THz} \end{pmatrix} = \begin{pmatrix} \frac{-1}{\sqrt{2}} & \frac{1}{\sqrt{2}} & 0 \\ \frac{-1}{\sqrt{6}} & \frac{-1}{\sqrt{6}} & \frac{2}{\sqrt{3}} \\ \frac{1}{\sqrt{3}} & \frac{1}{\sqrt{3}} & \frac{1}{\sqrt{3}} \end{pmatrix} \begin{pmatrix} d_{14}\frac{2}{3}E_{NIR}^2\left(\sqrt{3}\cos\theta - \sin\theta\right)\sin\theta \\ d_{14}\frac{-2}{3}E_{NIR}^2\left(\sqrt{3}\cos\theta + \sin\theta\right)\sin\theta \\ d_{14}\frac{-1}{3}E_{NIR}^2\left(1 + 2\cos 2\theta\right) \end{pmatrix} \tag{B.9}$$

$$\begin{pmatrix} P_{x_{lab}THz} \\ P_{y_{lab}THz} \\ P_{z_{lab}THz} \end{pmatrix} = d_{14} \begin{pmatrix} -\sqrt{\frac{2}{3}}\ E_{NIR}^2 \sin 2\theta \\ -\sqrt{\frac{2}{3}} E_{NIR}^2 \cos 2\theta \\ -\sqrt{\frac{1}{3}} E_{NIR}^2 \end{pmatrix} \tag{B.10}$$

The THz polarization is proportional to the square of femtosecond lasers electric field. The output power of the THz is therefore proportional to the square of input pump beam power. The magnitude of the THz polarization is constant, does not depend on the direction of the polarization of the femtosecond laser's electric field. However, the direction of the THz polarization depends on the direction of laser's field in a nontrivial manner. The THz polarization in the $z_{lab}$ direction will not radiate THz in the forward direction. The radiation from $P_{zlab}$ will be emitted into dielectric slab modes. In electro-optic sampling measures only the THz electric field component along the <110> edge of the ZnTe sensor. If the lasers beam's polarization is rotated 180° the signal will vary sinusoidal with a period of 90°.

Figure 6.5 shows the THz electric field along the <110> edge of the ZnTe as the pump beam polarization is rotated by a half wave plate.

If the pump beam's polarization is held constant and the <111> GaAs wafer is rotated about the $\mathbf{z}_{lab}$ axis a different angular dependence will result. Rotating the GaAs wafer is equivalent to rotating both the pump beam's polarization and the Zinc Telluride detector with the GaAs wafer fixed. The THz electric field is measured in the frame of the ZnTe which will be denoted as $x_{\mathrm{ZnTe}}$, $y_{\mathrm{ZnTe}}$, $z_{\mathrm{ZnTe}}$. The THz electric

field must be expressed in the ZnTe frame to find the signal's rotational dependence. The coordinates in the ZnTe frame can be transformed into coordinates in the lab frame using a unitary rotation matrix.

$$\mathbf{U}(\theta) = \begin{pmatrix} \cos\theta & \sin\theta & 0 \\ \sin\theta & \cos\theta & 0 \\ 0 & 0 & 1 \end{pmatrix} \tag{B.11}$$

Then in the $x_{\mathrm{ZnTe}}$, $y_{\mathrm{ZnTe}}$, $z_{\mathrm{ZnTe}}$ basis the THz polarization is found to be

$$\begin{pmatrix} -\sqrt{\frac{2}{3}}\, d_{14} E_{NIR}^2 \sin 3\theta \\ -\sqrt{\frac{2}{3}} d_{14} E_{NIR}^2 \cos 3\theta \\ -\sqrt{\frac{1}{3}} d_{14} E_{NIR}^2 \end{pmatrix} = \mathbf{U}(\theta) \begin{pmatrix} -\sqrt{\frac{2}{3}}\, d_{14} E_{NIR}^2 \sin 2\theta \\ -\sqrt{\frac{2}{3}} d_{14} E_{NIR}^2 \cos 2\theta \\ -\sqrt{\frac{1}{3}} d_{14} E_{NIR}^2 \end{pmatrix} \tag{B.12}$$

In Figure 6.6 the THz electric field dependence on the crystal orientation is shown. When the <111> GaAs crystal is rotated about $\mathbf{z}_{lab}$ axis the peak THz electric field undergoes a sinusoidal oscillation with a period of 120° which is consistent with (B.12)

# Appendix C 3D THz photonic crystals.

The coupling of light into 2D photonic crystals can be difficult. A plane wave will not couple into a 2D photonic crystal's guided modes unless it is incident on the edge. For efficient edge coupling, light must be brought to a line focus across the edge. If the transmitted light is to be collected, it must be collimated after it exits the slab's opposite edge. A plane wave when incident on the surface of a photonic crystal slab can couple into leaky modes above the light-line. However photonic bandgaps are located below the light-line.

Coupling into a 3D photonic crystal is more straightforward. Plane waves that probe the entire band structure can be coupled into it from any angle. 3D photonic crystals have been fabricated for the THz range. Si woodpile structures have been fabricated out of high resistivity Si and etched with a crystalline isotropic etch to create wood pile structures[50]. The bandgap of these structures was near .5 THz. The woodpile structure has also been used to fabricate 3D photonic crystals at near-infrared frequencies[51].

We attempted to make a 3D photonic crystal invented by Johnson[52, 53]. This photonic crystal was made of 2D photonic crystal elements. The 3D photonic crystal is shown in Figure C.1. The waveguide and defect modes of the 3D photonic crystal

are similar to the waveguide and defect modes of the 2D photonic crystals elements it is made of[54]. In this regard the 3D photonic crystal is unique.

The two 2D photonic crystal elements were a triangular lattice of air holes in a dielectric slab and a triangular lattice of dielectric cylinders. The two elements were combined to form a single layer. The dielectric cylinders were placed on top of the

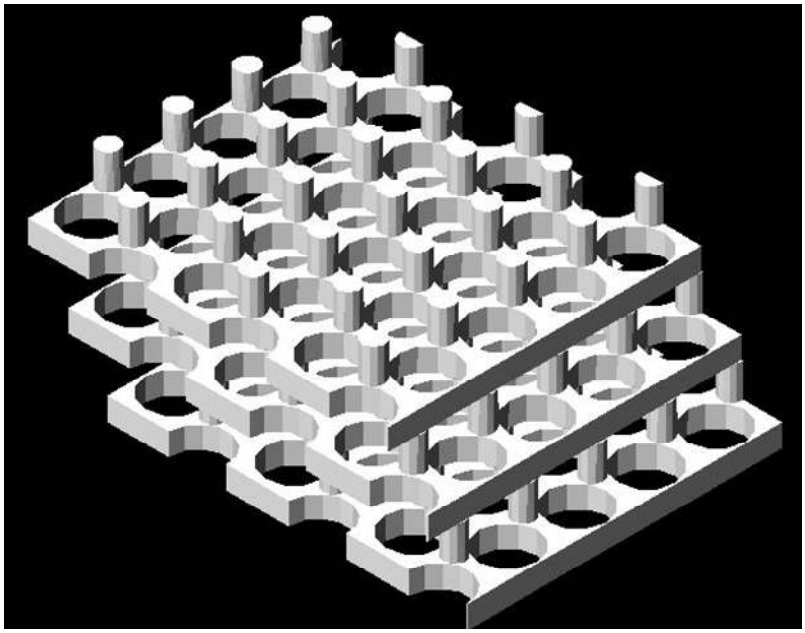

**Figure C.1** 3D photonic crystal constructed from 2D photonic crystal elements

dielectric region between the air holes. As for the woodpile photonic crystal, this 3D photonic crystal was made by stacking layers on top of identical previous layers. The position of each layer was shifted with respect to the position of the previous layer.

Each layer was made using two masks and two etches as illustrated in Figure C.2. A $SiO_2$ hardmask defined the dielectric cylinders during the second mask. A

resist mask defined the air holes during the first etch. The resist layer was over laid on top of the $SiO_2$ mask. The wafer was initially etched with both masks to a predetermined depth. This transferred the air holes into the wafer. The wafer was then taken out of the reactive ion etcher, and the resist mask was then removed. The wafer was then etched again with only the $SiO_2$ mask which defined the cylindrical columns.

Each layer was made out of high resistivity Si wafers with a thickness of approximately 45$\mu$m. The Si wafers were coated with 200 nm of PECVD grown $SiO_2$. The thinness of the wafers made them flexible and easy to bend. To handle the

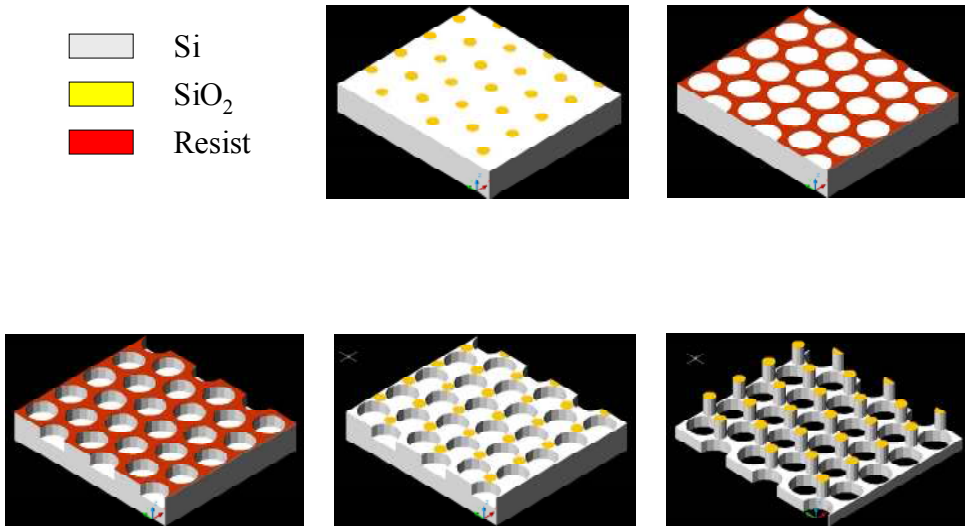


**Figure C.2** Schematic of the fabrication of a single layer element of the 3D photonic crystal.

wafers it was necessary to attach them to 500$\mu$m thick support wafers using resist as a bonding layer.

The support wafers were coated with a layer of PECVD grown $SiO_2$ to prevent the being etched during the DRIE etches. AZ4110 photoresist was spun at a high speed (>5000 RPMs) onto the support wafers. The thin Si wafers were then dropped onto the support wafers. A smooth machined cube of Al was then placed on top of the thin Si wafer and a slight amount of pressure was applied with a thumb. The support wafers and the thin Si wafers were then placed on a hotplate to cure the resist. Once the thin Si wafers were bonded to the support wafers they could be handled without breaking. The thin Si wafers could be removed by from the support wafers by soaking the wafers in acetone overnight. Cleaning the wafers with solvents for several minutes did not separate them. The solvent must diffuse several centimeters into a layer with a thickness less then 1$\mu$m which takes a long time.

The $SiO_2$ hard mask was patterned using AZ4110 resist and a hydrofluoric (HF) wet etch. It was necessary to apply Hexamethyldisilizane (HMDS) before applying resist to the wafer as a primer to promote resist adhesion. Otherwise the resist would be removed when it was developed. After the HF wet etch the remaining resist was removed and the wafer was cleaned. AZ4110 resist was spun on the wafer at 5000 RPMs. The second mask was aligned on top of the $SiO_2$ mask. Placing colored filters before the contact aligner's microscope light source aided the alignment by enhancing the color contrast between resist and $SiO_2$. During both lithography steps it was critical to remove the edge bead to ensure close contact.

After the masks were formed, the support wafers were bonded to 4 inch carrier wafers. The DRIE machine only handles 4 inch wafers. During the etch the back

side of the carrier wafer is cooled with He gas. If a sample is not thermally connected to the cooled carrier wafer, the plasma will heat the sample and increase its temperature. This leads to deleterious effects. Either the mask will be removed or the quality of the etch will be poor. To prevent this, the support wafers was bonded to the carrier wafers in similar manner to the bonding of the 45$\mu$m thick wafers to the

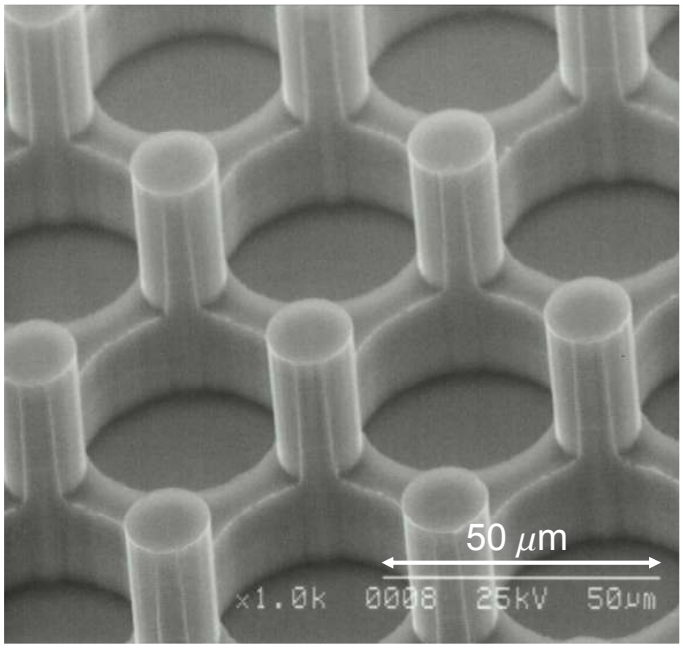


**Figure C.3** Fabricated single layer element of the 3D photonic crystal.

support wafers. The support wafer was turned over. The spinner was place on a region of the support wafer where there was no sample. AZ4110 photoresist was spun on the back side of the support wafer. The support wafers had to be double side polished so resist could be spun on the back and front sides. The support wafers were then placed on the 4 inch carrier wafer. Pressure was applied with tweezers and the wafers were baked on the hotplate.

The ideal method to stack the wafers would be to bond the Si layers together using an aligned wafer bonder. However, no such machine was available at UCSB. Instead we tried to bond the wafers with a flip-chip bonder. The highest available temperature of the flip-chip bonder was 300°C. This is below the eutectic temperature of Au-Si, and an Au-Si bond could not be used. Instead AZ4110 resist was used as an intermediate bonding layer. The resist bond is not as permanent as a Si-Au or Si-Si bond. The layers can be unstacked using acetone.

A 500$\mu$m thick float zone Si wafer was used as a substrate to support the thin wafers. Resist was spun at high speed on the support wafer and the stack of thin

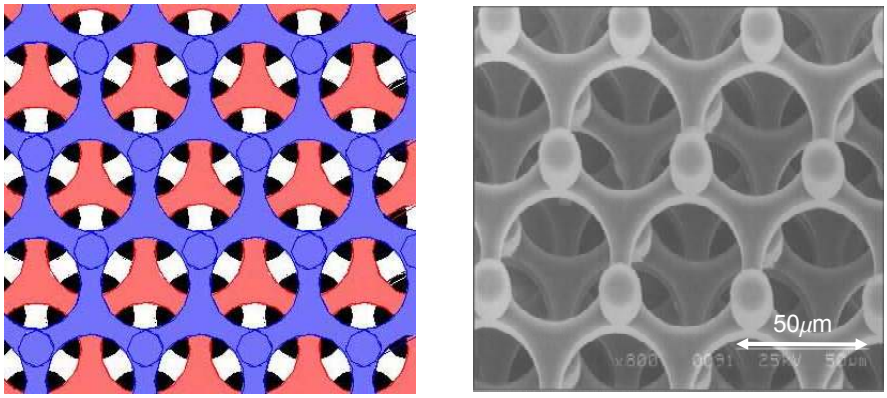


**Figure C.4** Left: schematic of stacked 3D photonic crystal (different colors are different layers) Right: SEM picture of stacked test structure with low resistivity test wafers.

wafers on top of it. A thin wafer was bonded to this stack of thin wafers (or the support wafer) with the flip chip bonder at a pressure of 1,000 grams and at a temperature of 110°C. Initial results with low resistivity 60$\mu$m thick Si wafers were

promising as shown in Figure C.4. However after much effort, they could never be repeated for the higher resistivity samples.

Wafers to be bonded in the flip-chip bonder are attached by a vacuum to upper and lower plates. The lower plate moves toward the upper plate to commence bonding. The distance between the upper and lower plate is on the order of an inch. When the riser moves the lower plate up it must not deviate from the vertical direction - otherwise the bond will be misaligned. Before bonding a probe with cameras is inserted between the lower and upper plates. The images of the lower and upper plates are seen on a screen. This allows the flip chip bonder to align the two wafers.

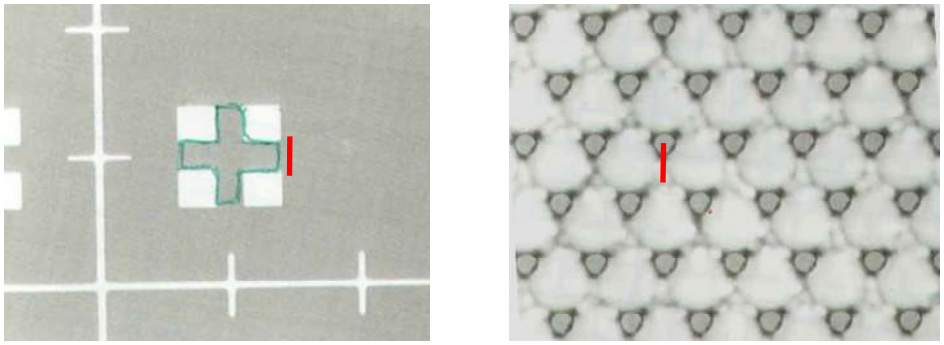

**Figure C.5** Alignment marks of flip chip bonder compared to microscope image of a single layer on the same scale. The red marks are for comparing sizes.

The probe must be calibrated with two glass reticules before it is used. The left hand side of Figure C.5 shows an image of the lower glass reticule. The upper glass reticule is not shown. It consists of crosses which must be placed in between the squares on the lower glass reticules. The right hand side of Figure C.5 shows a

microscope picture of one layer of the photonic crystal. As can be seen the alignment marks on the flip chip bonder are bigger then the smallest feature on the layer of the photonic crystal. It can bee seen that the distance needed to displace the layer from one and other is less then the distance of the alignment marks.

Another possible way to bond the layers together would be to etch a corner in a piece of Si. The thin wafers or layers of the photonic crystal could then be pushed up against the corner. This would entail creating three separate layers whose photonic crystal pattern would be shifted from the edge. Of course, an aligned wafer bonder that accepts pieces would be the most straightforward way to bond the layers together.

Interestingly although 3D photonic crystals solve some coupling problems, their fabrication is more difficult then 2D photonic crystals. This is the reason why so few groups are working on 3D photonic crystals, and more research is focused on 2D photonic crystals.

# Appendix D Reactive ion etching

Reactive Ion etching is used to etch anisotropic features in semiconductor wafers. The standard RIE can be thought of as a capacitor in a vacuum chamber. The wafer to be etched is placed on the end of the capacitor. Various chemical species in the wafer gas phase are allowed to flow into the chamber and pumped out. The pressure inside the chamber is kept constant on the order of few milliTorrs. An AC voltage applied to the capacitor ionizes a small number of the chemical species. Typically less then 1 in $10^5$ molecules are ionized. The ionized species accelerate toward the semiconductor surface where complex chemical and physical processes take place. Volatile species will be formed out of ions semiconductor atoms. These species evaporate and are pumped out of the chamber. The low pressure increases the mean free path of the molecules. This ensures that collisions with other atoms which will randomize the ion's directions are avoided. Ionized species strike the surface vertically. This directionality of ions is responsible for the anisotropy of the process. Reactive ion etching is a complex process. Parameters that can be varied include the composition of the gases, flow rate of the gases, the pressure, and the voltage or power applied to the capacitor. In addition etches will often be affected by prior etches, since chemicals from prior etches will coat the sidewalls of the chamber. A cleaning etch run before the real etch will alleviate this problem.

Reactive ion etching is both a physical and chemical process. Two different processes are responsible for the etch's anisotropy. One is when chemical reactions do not occur spontaneously and must be initiated by the kinetic energy of sputtering ions. The low pressures ensure that the flux of the ions is normal to the surface and no etching of the sidewalls will take place.

The other process occurs when passivating chemicals which would otherwise arrest the etch are sputtered off the surface. The flux of ions is greater on the surface then on the sidewalls. The removal of the passivating chemicals is the limiting process of the etch. The passivating chemicals will be removed faster on the surface then on the sidewalls.

In practice all reactive ion etching proceeds by a combination of both processes. Most etches are performed with a variety of gases. Often the different gases and different elements have a specific role in the etch. Some of the gases form volatile species with the material to be etched. Other elements are passivating agents that stop chemical reactions. They must be removed if the etch is to continue. Argon is often employed to sputtering of passivating layers. Some authors also claim that Argon improves the reproducibility of etches. It is believed that Argon somehow improves the uniformity of the plasma. Molecules may contain elements that perform different functions during the etch.

Most chemistry for etching Si includes Fluoride and Carbon containing compounds such as $SF_6$ or $CF_4$. Fluoride radicals are highly reactive and form $SiF_4$. The $SiF_4$ is volatile and removes Si when it evaporates. Carbon has a tendency to

form polymers which inhibit etching and serve as a passivating layer. In general the type of etch can is strongly affected by the F/C ratio. If the F/C is high the etch will faster, less selective, and more isotropic. If the F/C ratio is lower the etch will be slower more selective and more anisotropic. Often the addition of other elements will change the F/C ratio. For example hydrogen will scavenge Fluoride ions to from HF lowering the F/C ratio, while oxygen added to the chamber will form $CO_2$ and CO increasing the F/C ratio.

For GaAs etching chloride chemistry is often employed. The $Cl_2$ and $BCl_3$ are often used. The chlorine ions form volatile compounds with the GaAs, while boron serves to passivate the etch.

In addition to all previous mentioned effects, the samples themselves will often influence the etch. In general a trench with a larger aspect ratio will etch faster then trench with a smaller aspect ratio. Loading effects may occur when the etch rate will decrease as more as the area to be etched increases. I have also seen the geometry of the surface effect etches. Areas next to features such as wafer discontinuities often have different etch characteristics.

# Appendix E Processing notes

## *(a) Mask preparation*

Clean new photoresist bottles. Fill and shake inside with acetone, isoproponal, and methanol. Fill and shake several times with D.I. water. Place bottle in 120°C convection oven. If photoresist bottle is cold let warm up for 24 hours. Do not put photoresist in a hot or warm bottle. To prevent dry resist from contaminate bottle never use a bottle with pipette attached to cap or dropper.

Clean wafers before lithography. Rinse or immerse in acetone, isoproponal, methanol, and rinse in D.I. wafer. Before spinning wafer and HMDS vapor treatment at least a 2 minute dehydration bake on hotplate at 110°C. Adjust acceleration of the spinner to highest level.

Photoresist or $SiO_2$ can by used as a mask. $SiO_2$ has a higher selectivity, but a photoresist mask has less steps. Thin (<500nm) $SiO_2$ hardmasks can be etched with Hydrofluoric acid. Etch rate of PECVD deposited SiO2 approximately 500nm per minute. Thick (>500nm) $SiO_2$ hardmasks should be etched in the Panasonic ICP using the SiO2Vert recipe. $SiO_2$ hardmasks should never be etched in RIE#3. The processing in Chapter 7 was performed before the arrival of the Panasonic ICP.

AZ4110 (1 $\mu$m at 5,000 RPM), AZ4210 (2$\mu$m at 5,000 RPM), AZ4330 (3,000 $\mu$m at 5,000 RPM) photoresists - Spin at speed for desired thickness. Softbake 1 minute 95°C on hotplate. Hardbake (optional) 1 minute 110°C on hotplate. Develop in 1:4:AZ400K: $H_2O$. Contact aligner intensity 7.5 W/cm2. For vertical sidewalls the exposure time should be approximately equal to develop time. Exposure and developer times will vary and depend on the age of resist. If resist residue remains that will not develop do an $O_2$ descum. $O_2$ descum 300mTorr, 100 Watts, power resist removal rate 100nm per minute.

AZ9260 (6.5$\mu$m at 5,000 RPM) softbake 110°C for 90 seconds on hotplate. Develop 1:4:AZ400K: $H_2O$. Exposure time should be on the order of the developer time. If resist residue remains that will not develop do an $O_2$ descum.

For Si and $SiO_2$ resist with unconnected features may need HMDS treatment - to promote resist adhesion. Place a few drops of HMDS in a Petri dish. Turn Petri dish over on wafer to be spun. Wait 2 minutes. HMDS vapor will be coated on surface of wafer proceed to apply resist and spin wafer.

### *(b) Bonding of samples to carrier wafers for DRIE etches*

Carrier wafers should be coated with $SiO_2$. Carrier wafers must be 4 inch Si wafers with a flat. Exposed Si will lead to loading effects and decrease the etch rate.

The sample must be thermally connected to the carrier wafer for good etch results. A thin coating of cured photoresist (1 micron thick) between the sample and carrier wafer results in the best thermal bond

Spin AZ4110 on backside of sample (or only for $SiO_2$ hardmasks carrier wafer) at > 5,000 RPMs. Put sample on carrier wafer. Cure photoresist at 95°C for several minutes. Apply pressure on corners of sample with tweezers. Sample should not be removed when soaked in acetone for several minutes. (Optional) Cure photoresist at 110°C for several more minutes. If resist was spun on a carrier wafer (only for a SiO2 hardmask) soak in acetone to remove all resist.

To remove sample from carrier wafers soak in acetone overnight. Cover glassware with Al foil to prevent evaporation.

### *(c) Deep Reactive Ion etching (DRIE)of Si*

Use standard Bosch recipe. Before each etch run a season process - bare Si wafer 20 minute etch - to condition chamber. Computer time does correspond to actual time. Each loop of Bosch process takes 16.7 seconds not 13 seconds. Verify the plasma starts. Verify there is no reflected RF bias power during Etch B. Any reflected power during etch B will result in a poor etch. There will be reflected RF bias power during etch A. Nominal etch rate .8$\mu$m per loops. Etch rate is aspect ratio dependent, and will dependent on amount of exposed Si. Etching should always be done for a given amount of loops, never for a given amount of time. Otherwise etch could end on polymer deposition step. For long etches or for thermal problems - program machine to etch increments of 50 loops. The cool down time between 50 loops will decrease the likelihood of elevated temperatures. Nominal selectivity (mask: Si etched) photoresist masks 70:1, $SiO_2$ masks 200:1

**Standard bosch DRIE etch**

DEP - Deposition Step. Polymer deposited to passivate sidewall.

| | |
|---|---|
| $C_4F_8$ | 70 sccm |
| $SF_6$ | 1.5 sccm |
| Ar | 40 sccm |
| $O_2$ | 0 sccm |
| RF1 Bias | 1 Watt |
| RF2 ICP | 825 Watt |
| Pressure | 22mTorrs |
| Time | 5.0 seconds (computer) |

Etch A - Transition step between deposition and etching step.

| | |
|---|---|
| $C_4F_8$ | 1.5 sccm |
| $SF_6$ | 50 sccm |
| Ar | 40 sccm |
| $O_2$ | 0 sccm |
| RF1 Bias | 9.0 Watt |
| RF2 ICP | 825 Watt |
| Pressure | 23mTorr |
| Time | 2.0 seconds (computer) |

Etch B - Etching step - Si etched with Fluorine radicals.

| | |
|---|---|
| $C_4F_8$ | 1.5 sccm |
| $SF_6$ | 100 sccm |
| AR | 40 sccm |
| $O_2$ | 0 sccm |
| RF1 Bias | 9.0 Watt |
| RF2 ICP | 825 Watt |
| Pressure | 23mTorrs |
| Time | 6.0 seconds (computer) |

### *(d) GaAs etches in the Panasonic ICP*

Check to make sure $CHF_3$/Ar gas line is switched to Ar. If not run Arlinprg. Always double check that "machine parameters" and the flow rate for the gases are set correctly. Double check even if gas line is already switched to Ar.

Always use 6 inch Si carrier wafers whose top surface is coated with SiO2. Si should never be exposed during the etch. Before a series of etches run GaAsClnCoat recipe consisting of 10 minute $CF_4/O_2$ clean and 5 minute $BCl_3/Cl_2$/Ar coating step. During cleaning steps the bias is set to zero.

Attached sample to carrier wafer with cleanroom provided diffusion pump oil. Place drop of diffusion pump oil on back of sample. Place sample in center of carrier wafer. Press sample down on wafer with tweezers. Diffusion pump oil should ooze out sides. For air holes etches use AZ9260 resist as mask and add AZ4330 in

chamber to increase sidewall passivation. Spin several layers of AZ4330 resist on two 1-2 square inch $SiO_2$ coated Si wafers. Place several drops of diffusion pump oil on back side of AZ4330 coated wafer. Place wafer on opposite sides of samples. Press down with tweezers.

**Standard GaAs Via and air hole etch recipe**

| | |
|---|---|
| $BCl_3$ | 40 sccm |
| $Cl_2$ | 100 sccm |
| $CF_4$ | 0 sccm |
| Ar | 20 sccm |
| $O_2$ | 0 sccm |
| RF Bias | 100 Watts |
| RF ICP | 900 Watts |
| Pressure | 7 Pascals |

Always check GaAsVia etch recipe to make sure no one has changed it.

### *(e) Developing masks for optical setup and cleanroom*

Look in logbook to set current Defoc and Energy value.

Do not expose mask to light - wrap in tin foil

Develop in 1:4 AZ400K:$H_20$ for 10 to 20 seconds.

Inspect under microscope.

If resist residue cannot be developed do an $O_2$ descum.

Etch Chrome in commercial Cr etch.

Leave in Cr etch for at least 4 minutes. Mask will appear to be clear after 2 minutes. Complete transparency will occur later.

Inspect mask under microscope with front illumination and then with bottom illumination.

Always error on the side of overdeveloping and overexposing.

### *(f) Ni metal wet etch*

$HNO_3$:$CH_3COOH$:$H_2SO_4$:$H_2O$ 5:5:2:28

Ni wet etch - rate 100nm per second

# Appendix F FDTD calculations of photonic crystal modes

In this appendix the finite-difference time domain (FDTD) method is briefly introduced, and FDTD simulations applied to photonic crystals are discussed. A heavily commented FDTD code that calculates photonic crystal slab frequencies at the Γ-point is included at the end of this appendix. The code is written in Matlab, but it should also run on non-propriety Matlab-like software such as Scilab. The attached photonic crystal FDTD code may be used as an initial template to write FDTD programs.

Many results necessary to completely understand the FDTD method are not explained in this appendix and simply stated. The intent is to give an introduction to the FDTD method and how it can be applied photonic crystal slabs. A full treatment of the FDTD method is beyond the scope of this work and can be found in Taflove[55]. With this reference a full understanding of the FDTD method and the attached FDTD codes can be used as templates with confidence.

## *FDTD method*

The FDTD method directly simulates electromagnetic fields in time on a computer. An initial field in a given structure is input into the FDTD program at the

start of the algorithm. Using Maxwell's equation the FDTD program calculates the propagation of the initial field in time. Both space and time and are discretized in the computer program. The FDTD program advances a given electromagnetic field at time $t$ to the electromagnetic field specified by Maxwell's equations at time $t + \Delta t$ .

Maxwell's equations are written in a discretized algebraic form by substituting derivatives with finite differences. In order for the algebraic equations to accurately approximate Maxwell's equations the temporal and spatial distance between points must be small.

The discretized algebraic equations of Maxwell's equations are solved for the fields at future times [**E**($t$+$\Delta t$), **H**($t$+$\Delta t$)] in terms of the fields at present times **[E**($t$), **H**(t)] and prior times **[E**($t$-$\Delta t$), and **H**($t$-$\Delta t$)]. Fields at prior times ($t$-$\Delta t$) are then discarded and the unknown fields at the new future time ($t$+$2\Delta t$ ) are found in terms of the new present time $t$+$\Delta t$ and prior time $t$. In this way the algorithm of the FDTD method advances the electromagnetic fields in time in a giant *for loop*.

The region of any FDTD simulation will be bounded. However, for many problems the electromagnetic fields need to be simulated on an unbounded region. Nonphysical boundary regions for FDTD simulations have been developed that strongly absorb incident radiation without any reflections. This allows a bounded region with absorbing boundary conditions to model an unbounded region.

FDTD calculations are preformed in the time domain - not frequency domain. They are more suited for studying field dynamics and less suited to finding

eigenfrequencies and eigenmode. However eigenmodes will often be sought in unbounded regions. Frequency-domain methods which require bounded regions will be inadequate. For unbounded regions the well developed FDTD absorbing conditions can be taken advantage of to find the eigenmodes. This can be done in the time-domain by introducing a current point source with short time duration and broad frequency spectrum.

The eigenmodes are the resonances of the problem. Resonant frequencies will constructively interfere while non-resonant frequency will experience destructive interference. At the end of the simulation only the resonant eigenmodes will remain. If the fields are stored at each time step, a Fourier transform can be performed to find the eigenmodes of the resonances. This time-domain FDTD method was used to find the frequencies and field profiles of photonic crystal slab modes at the Γ-point. However, one must be careful, if the current point source is placed on a node or its polarization is orthogonal to the mode's polarization - no coupling into the mode will occur. With the FDTD method one can never be sure if all the modes have been found.

## *Finite-difference derivatives*

The FDTD domain method numerically solves Maxwell's equations by representing time and spatial derivatives as finite differences. Any function can be expanded about a point in terms of a Taylor series. If the value of a function $f$ is known at time $t$ then the value of $f(t+\Delta t)$ is

$$f(t+\Delta t) = f(t) + \Delta t f'(t) + \left(\Delta t^2 / 2!\right) f''(t) + \left(\Delta t^3 / 3!\right) f'''(t) + \ldots \qquad \text{(F.1)}$$

If $\Delta t$ is small, higher order terms in the expansion can be neglected. The value of $f(t+\Delta t)$ can then be approximated using only the first few terms of equation (F.1) Conversely if the value of the $f$ is known in a small region around $t$ the derivatives of $f$ at $t$ may be found from (F.1). The first derivative $f'(t)$ can be written as

$$f'(t) = \frac{f(t+\Delta t) - f(t)}{\Delta t} - \left(\Delta t^1 / 2\right) f''(t) + \ldots \qquad \text{(F.2)}$$

or

$$f'(t) = \frac{f(t+\Delta t) - f(t-\Delta t)}{2\Delta t} - \left(\Delta t^2 / 6\right) f'''(t) + \ldots \qquad \text{(F.3)}$$

The approximations become exact as $\Delta t \to 0$. The order of the finite difference expression is the lowest power of the error term in $\Delta t$. (F.2) is a 1st order expression for $f'(t)$ in $\Delta t$ while (F.3) is a 2nd order expression for $f'(t)$ in $\Delta t$. As the order of the of the finite difference expression for $f'(t)$ increases the function $f$ must be known farther away from $t$. The 3rd order expression for $f'(t)$ will contain terms of the form $f(t+\Delta 2t)$, and $f(t+\Delta 2t)$. If the order of $f'(t)$ is low the temporal spacing $\Delta t$ will have to be very small to minimize numerical errors. The simulation will require a large number of points which will slow down the computation. If the order of $f'(t)$ is high then $\Delta t$ can be large. This will allow simulations with fewer points and result in faster computations. However the number of terms in the finite difference expressions will be greater and the algorithms will become more complicated.

## *Finite-difference differential equations*

A differential equations can be transformed into an algebraic expressions by substitution of the equation's derivative's with finite difference expressions such as (F.2) and (F.4). The differential equation's corresponding algebraic expression can then be solved for field at the farthest time in the future (usually $t+\Delta t$). Often the differential equation to be solved is separable. For example consider the one dimensional diffusion equation

$$\frac{\partial u(x,t)}{\partial t} = D\frac{\partial^2 u(x,t)}{\partial^2 x} \tag{F.5}$$

The function to be solved (the concentration $u(x,t)$) is specified at one instance in time $u(x,t)$ at all spatial points. When the finite difference expressions for the derivatives are substituted into equation (F.5), the resulting algebraic expression can be solved for $u(x,t+\Delta t)$

$$u(x,t+\Delta t) = u(x,t) + \left(D\Delta t/2\Delta x\right)\left(u(x+\Delta x,t) - 2u(x,t) + u(x-\Delta x,t)\right) \tag{F.6}$$

If the concentration $u(x,t)$ is known at time $\Delta t$ the concentration $u(x,t)$ can be found at time $\Delta t$. For the finite difference expressions to approximate the derivatives in equation (F.6), $\Delta t$ and $\Delta x$ approach must approach zero. The change from $u(x,t)$ to $u(x,t+\Delta t)$ must also be small if equation (F.6) is to be valid. It is not sufficient for both $\Delta t$ and $\Delta x$ to be small. The ratio $D\Delta t/\Delta x$ must also be small if equation (F.6) is to be valid.

For a given $\Delta x$ the accuracy of equation (F.6) will improve as $\Delta t$ goes to zero, but the number of time steps will increase making the computation much longer. As $\Delta t$ increases the number of time steps decreases however $D\Delta t/\Delta x$ becomes larger making equation (F.6) less accurate. In general there will often be an optimal time step $\Delta t$ for a given grid spacing $\Delta x$. For FDTD simulations the optimal time step $\Delta t_{optimal}$ is

$$\Delta t_{optimal} = \frac{c}{\sqrt{\Delta x^2 + \Delta y^2 + \Delta z^2}} \tag{F.7}$$

## *Coupled electro-magnetic equations*

In the FDTD method invented by Yee[56] the electric and magnetic fields are advanced in time using two coupled first order Maxwell equations

$$\frac{\partial \mathbf{E}}{\partial t} = \frac{(\nabla \mathrm{x} \mathbf{H}) - \mathbf{J}}{\varepsilon} \tag{F.8}$$

and

$$\frac{\partial \mathbf{H}}{\partial t} = (\nabla \mathrm{x} \mathbf{E}) \tag{F.9}$$

The units of both the free space permittivity $\epsilon_o$ and permeability $\mu_o$ have been set to 1. Instead of one time step for both fields, there are two separate time steps for the magnetic and electric fields. At time $t$=0 the initial magnetic field $\mathbf{H}(t=0)$ is specified. The electric field $\mathbf{E}(\Delta t/2)$ is then calculated at time $\Delta t/2$ using the finite-difference form of equation (F.8). The magnetic field $\mathbf{H}(t=0)$ is discarded and the magnetic field $\mathbf{H}(\Delta t)$ at time $t=\Delta t$ is calculated from the electric field $\mathbf{E}(\Delta t/2)$ using equation (F.9) The magnetic field $\mathbf{H}(\Delta t)$ is then used to find the electric field

$\mathbf{E}(\Delta 3t/2)$ at time $t=\Delta 3t/2$. Thus the magnetic field is specified at times $t = 0, \Delta t, 2\Delta t, 3\Delta t,\ldots$ while the electric field is specified at $t = \Delta t/2, 3\Delta t/2, 5\Delta t/2, 7\Delta t/2,\ldots$

The magnetic and electric fields are never known at the same time. In order to calculate the power density $\epsilon\mathbf{E}^2(t) + \mu\mathbf{H}^2(t)$ or the Poynting vector $(\epsilon\mathbf{E}^2(t) \times \mu\mathbf{H}^2(t))$, one of the fields must be interpolated in time. This can create computational artifacts. There is often a small spurious sinusoidal variation on top of the true value of the power density or Poynting vector. The spurious variations can be reduced be decreasing the grid spacing $\Delta x$. This will decreased the time step $\Delta t$ according to equation (F.7) which improves the interpolation of the fields.

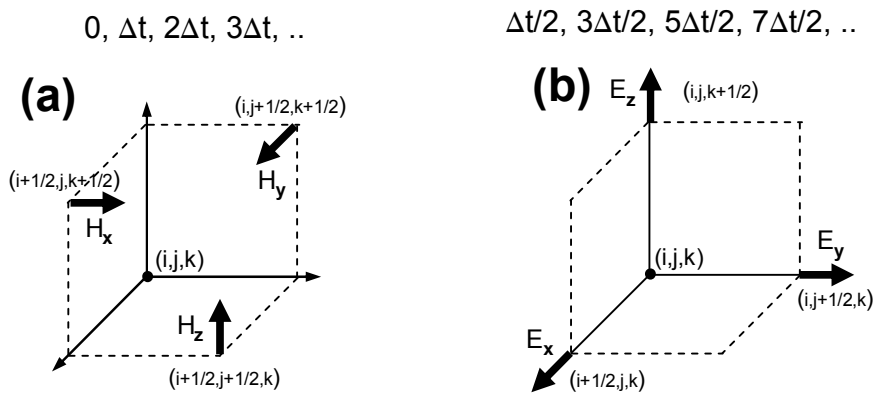


**Figure F.1** Placement of the field components for a grid point (i,j,k) in the Yee FDTD lattice. (a) Magnetic field components (b) Electric field components

Instead of coupled 1st order differential equations between two fields, equations (F.8) and (F.9) may be recast as a single 2nd order differential equation involving only one field. (This can be done be differentiating equation (F.8) ((F.9)) and then

eliminating the magnetic (electric) field using equation (F.9) ((F.8)).) The 2nd order differential equation could be recast in terms of finite differences, to numerically simulate the time evolution of the field. However, one would effectively be calculating only the electric (or magnetic) field at $t = 0, \Delta t, 2\Delta t, 3\Delta t, \ldots$. The FDTD method calculates both the electric and magnetic field in interleaved time steps of $\Delta t/2$. This makes the FDTD method of solving two coupled 1st order equations more robust then solving a single 2nd order differential equation.

## *Yee-grid - Ampere's and Faraday's laws*

The finite difference equations of (F.8) and (F.9) satisfy the differential forms of Maxwell's curl equations. The finite difference equations must also satisfy the integral forms of the Maxwell's curl equations

$$\int_{Area} \frac{\partial \mathbf{E}}{\partial t} \bullet \mathbf{dA} = \int_{Contour} \frac{\mathbf{H}}{\varepsilon} dl - \int_{Area} \frac{\mathbf{J}}{\varepsilon} \bullet \mathbf{dA} \qquad \text{(F.10)}$$

$$\int_{Area} \frac{\partial \mathbf{H}}{\partial t} \bullet \mathbf{dA} = \int_{contour} E\, dl \qquad \text{(F.11)}$$

In order to satisfy the integral equations (F.10) and (F.11) with the least number of points for a given grid spacing $\Delta x$, the electric and magnetic field a grid point $(i, j, k)$ are placed in different regions of space. The placement of the field components is shown in Figure F.1.

In Figure F.2 the Yee grid can be seen to satisfies equations (F.10) and (F.11). The magnetic field component $\mathbf{H}_x$ is determined from the line integral of the

surrounding electric field components $\mathbf{E}_z$ and $\mathbf{E}_y$. The components of the electric fields are determined by the surrounding line integrals of the magnetic fields components (not shown).

In Figure F.2 it is assumed that $\Delta x=\Delta y=\Delta z$. The distance between the grid point

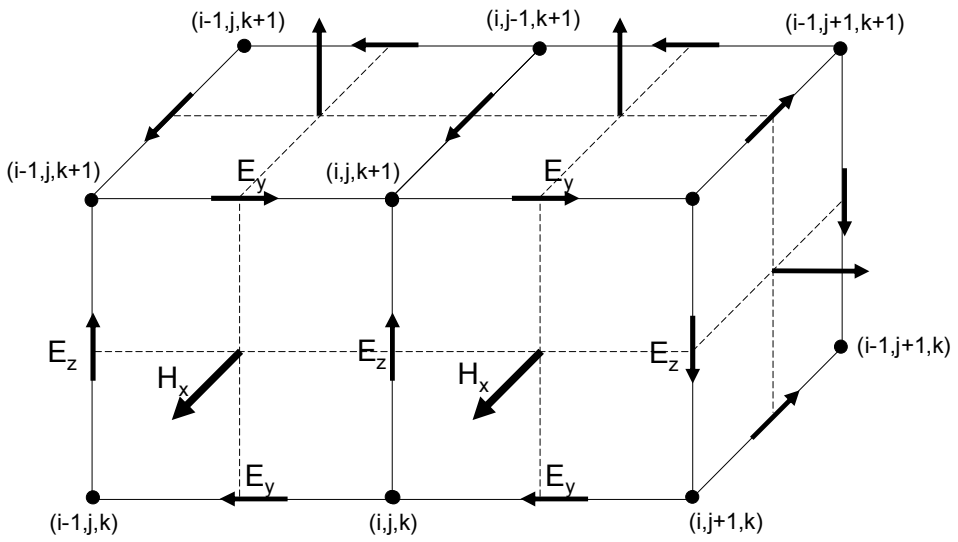


**Figure F.2** Yee FDTD lattice drawn for multiple grid points. Each magnetic (electric) field component is surrounded by 4 electric (magnetic) field components such that Faraday's law (Ampere's law) is satisfied. The electric and magnetic fields are present at different times.

$(i, j, k)$ and its electric (magnetic) field components is $\Delta x/2$ ( $\Delta x/\sqrt{2}$ ). The distance between the $\mathbf{E}_y$ component at $(i+1/2, j, k)$ and the $\mathbf{E}_y$ component at $(i-1/2, j, k)$ is $\Delta x$.

If $\Delta x/2$ is substituted for $\Delta t$ in equation (F.3), then a 2nd order finite difference expression can be used for $\frac{\partial \mathbf{E}_y}{\partial x}$. A second order expression for the time derivatives

with $\Delta t/2$ time can also be employed. With the Yee grid the finite difference equations of the FDTD method are accurate to 2nd order. Errors will scale as $(\Delta t/2)^2$ and $(\Delta x/2)^2$.

Now suppose that all 6 field components are specified at each grid point $(i/2, j/2, k/2)$ and the distance between grid points is $\Delta x/2$. The error of the 1st order finite different expression for the spatial derivatives will scale as $(\Delta x/2)^1$. The Yee FDTD method in addition to being 2nd order also has less field components then a 1st order method with a grid spacing of $\Delta x/2$ and fields at each grid point. Using the Yee FDTD method gives better accuracy with fewer points!

If a 2nd order expressions are used for the time and spatial derivatives when all 6 field components are specified at every $(i/2, j/2, k/2)$ point, then accuracy will be the same as Yee FDTD method. However, the Yee FDTD method has a factor of 1/6 less points then a grid with all its field components specified at every $(i/2, j/2, k/2)$ point. It is this combination of accuracy and economy which makes the Yee FDTD method so robust. In practice the Yee FDTD grid is almost always used and the Yee FDTD method is commonly referred to as the FDTD method.

## *Boundary conditions*

The computational grid must terminate. For a region bounded by a perfect magnetic conductor (PMC) or a perfect electric conductor (PEC), the appropriate tangential and normal fields may be set to zero. Bloch periodic boundary conditions are also straightforward to apply to the simulation.

It is more difficult to model problems with no boundaries, or boundary conditions at infinity. For these problems absorbing boundary conditions have been invented that will strongly absorb incident plane waves with no reflections. There are two types of absorbing boundary conditions perfectly matched layer (PML) boundaries, and analytic boundary conditions.

The program in this appendix uses CPML boundary conditions (a variant of the PML boundaries found in Taflove). The CPML boundary employs an artificial medium (which typically consists of 5-10 grid points) that surrounds the boundary of the simulation. In the artificial medium the fields obey a more general set of equations of which Maxwell's equations are a subset. The PML medium contains an artificial material with matched electric and magnetic conductivities. Any incident plane waves will be strongly absorbed in the PML medium without experiencing any reflections.

For a triangular photonic crystal slab, PML boundary conditions can be employed above and below the slab. In the direction along the slab the photonic crystal is Bloch periodic and Bloch periodic boundary conditions can be employed.

In contrast to a rectangular lattice, implementation of periodic boundary conditions on a triangular lattice using a Cartesian grid is not straightforward. A hexagonal grid could be employed instead of a Cartesian grid - however this would make the FDTD program very complicated. Another solution could be to work with a larger rectangular cell that contains the unit cell of the lattice and also tessellates the plane. For example the rectangular region shown in Figure F.3(b) will tessellate the

plane and has periodic boundary on all four of its sides. However many points in the rectangular region of Figure F.3(b) are redundant. Also any source term will have to be placed in multiple areas of the rectangular region of Figure F.3(b).

One method that allows the calculation to be performed on a rectangular grid without redundancy is show in Figure F.3(c). The computational grid to be modeled is half of the rectangular region shown in Figure F.3(b). The region in Figure F.3(c) has no redundant points, and has the same area has the unit cell. However the region in Figure F.3 (c) has quasi-periodic boundary conditions on the top and bottom sides.

However the red and blue colored portions are periodic regions of the top and bottom sides of Figure F.3 (c). If the red and blue sides are interchanged, then normal

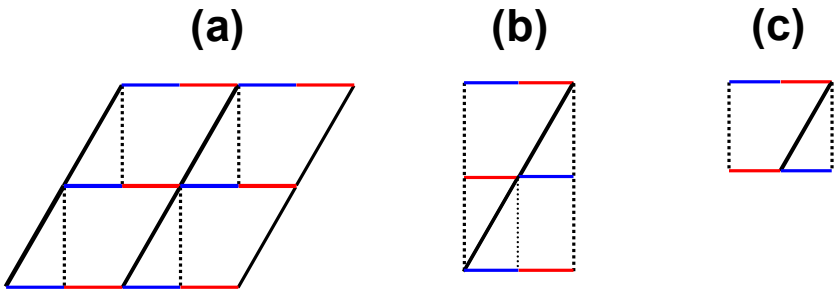


**Figure F. 1** (a) 4 unit cell's of a triangular lattice (b) Cell with period boundary conditions that can be used to construct the lattice in part a (c) Cell with quasi-perodic boundary conditions that has the same area as the unit cell

periodic boundary conditions can be applied to the region of Figure F.3(c).

In order to reconstruct the field from Figure F.3(c) over several lattice constants the field must be flipped to generate an equivalent region to Figure F.3(b). If the

dielectric function is symmetric under mirror reflections about the bottom line. The other half of the field in Figure F.3 (b) can be found using symmetry operations.

## *Example FDTD program*

The FDTD program attached below finds the eigenfrequencies of a triangular photonic crystal slab at the Γ-point. If the plane in the center of the slab is at z = 0, the program only calculates the fields in the top half ( z > 0) of the computational space. A perfect magnetic conductor (PMC) is placed at z = 0. This problem can be shown to be equivalent to finding the TM modes in both halves of the computational space. The program is carefully annotated and the reader should be able to modify it and use it as a template.

The program was written in Matlab and should also work in Scilab, the non-propriety version of Matlab. It is much easier to write and debug code in Matlab then C or FORTRAN. In general Matlab code will run much slower then C code. However Matlab code is much easier to write since it is a higher level language - one does not have to worry about of allocating memory and other low level tasks.

## *Matlab syntax*

The syntax of Matlab is similar to C. However, Matlab is designed to work with matrices and has some unique syntax associated with them. In the attached FDTD program each field component is represented by an individual matrix. For example the matrix EX contains the x components of the electric field. The syntax * is used for matrix multiplication. To multiply the matrices element by element the syntax

(.*) is used. The same syntax holds for dividing matrices / (./) and taking powers ^ (.^). In the FDTD program multiplication and division of matrices is always done element by element and the period (.) must always be used. The only exception is multiplication or division by scalars. The indices of all matrices are integers which begin with 1 - not 0. Thus EX(1,1,1) would be the x electric field component in a corner of the computational grid. The colon : is used to create list of integers for example [1:3] is the list (or one dimensional matrix) 1,2,3. Matlab executes for loops slowly. Whenever possible, for loops should be replaced with syntax using the colon operator. This is referred to as vectorizing the code. For example if the size of computation grid is 10x10x10 points then EX([1:10],[1:10],[1:10]) = 0; sets all of the values of EX to zero. (The semicolon after the statement prevents the output from appearing on the screen.) This could also be written as 3 *for loops* in Matlab or C. The vectorized code can be written in a cleaner form by using indices. The previous example can be written as i=[1:10]; j=[1:10]; k=[1:10]; EX(i,j,k)=0; which is much easier to read.

```
% 3-D FDTD program with CPML layer on top and PEC layer on bottom
% PEC - use symmetry of TM-like modes to only calculate field in half the region

% ie, je, and ke the number of grid points in the X, Y, and Z directions
% c=1    (speed of light - not explicitly used in code)
% eps = 1 (electric permitivity of vacuum - not explicityly used in code)
% dielectric (permitivity of the dielectric)
% eps(i,j,k)    (dielectric permititity of material - matrix)
% mu = 1   (magnetic permability)

% a=1  (lattice constant of photonic crystal - not explicitly used in code)
% radius   (air hole radius units of a)
% thickness (dielectric slab thickness units of a)

% dX dY dZ  (distance increments) dT (time step) (This code dX=dY=dZ)

% Period (number of periods of fo to run - controls N)
% N (number of times steps to take)
% sampling_rate (nyquist frequency of sampling - controls Sample)
% Sample (record the field at every Sample=integer time step)
% sN (number of sampled frequency points)
% dF (frequency increment)

% a_ratio (amax/sigmax  to absorb only plane waves set a_ratio~0. )
% m (the order of the geometerically graded PML - must be between 3 and 4 )
% ma (order of graded pole offset - usually linear set to 1)

% fo  (the centered frequency of the gaussian source current pulse)
% widthfreq   (frequency width of guassian source current)
% aguass     parameter the specifies the width of the guassian Exp(-a t^2))
% to      (the time between the maximum of the guassian pulse and t=0)

%Vectors
% Monitor_E_1(t)  (monitor electric field vs time at one spatial point)
% Source(t)       (current source as function of time)
% filter(t)       (multiply Monitor_E_1 by filter to get rid of transients)
% filterSource(t) (filter*Source)
% freqpoints(f)   (vector of frequency points)

% Matrices
% sigEX, sigEY, sigEZ   (the electric conductiviy - matrices)
% sigHX, sigHY, sigHZ   (the ficticious magnetic conductivity - matrices)
% EX, EY, EZ, HX, HY, HZ  ( The electric and magnetic fields)
% CAEX, CAEY, CAEZ, CBEX, CBEY, CBEZ (CAEX and CBEX are the coieffiecients to find
the EX field component)
% DAHX, DAHY, DAHZ, DBHX, DBHY, DBHZ  (coieffiecients to find the magnetic field
componets)
% psi_EX_Z, psi_EY_Z, psi_HX_Z, psi_HY_Z funtions to implement the CPML
%*************************************************************************

%*************************************************************************
```

```
%Boundary conditions for electric Fields apply to i-1,j-1,k-1

%i=1 (Perodic B.C.) if(i=-1)then(i=ie)
%i=[1:10]                        = 1    2    3    4    5    6    7    8    9   10;
%ie=10; 1+mod(i+ie-2,ie)     = 10    1    2    3    4    5    6    7    8    9

%j=1 (Folded B.C.)   if(i=i,j=-1)then(i=(1+mod(i+(ie/2)-1,ie ),j=je)
%j=[1:10]                       =   1    2    3    4    5    6    7    8    9   10;
%je=10; 1+mod(j+je-2,je)     = 10    1    2    3    4    5    6    7    8    9
%and
%i=[1:10]                        =   1    2    3    4    5    6    7    8    9   10;
%ie=10  1+mod(i+(ie/2)-1,ie)  =  6    7    8    9   10    1    2    3    4    5;

%k=1 (PEC)  if(k=-1)then(set field to zero)

%*************************************************************************
%Boundary conditions for magnetic fields apply to i+1,j+1,k+1

%i=ie (Perodic B.C.)  if(i=ie)then(ie+1=1)
%i=[1:10];                      =  1    2    3    4    5    6    7    8    9   10;
%ie=10 1+mod(i+ie,ie)       =  2    3    4    5    6    7    8    9   10    1;

%j=je (Folded B.C.)  if(i=i,j=je+1)then(i=(1+mod(i+(ie/2)-1,ie ),j=1)
%j=[1:10]                       =  1    2    3    4    5    6    7    8    9   10;
%je=10 1+mod(j+je,je)       =  6    7    8    9   10    1    2    3    4    5;
%and
%i=[1:10]                         =  1    2    3    4    5    6    7    8    9   10;
%ie=10  1+mod(i+(ie/2)-1,ie)  =  6    7    8    9   10    1    2    3    4    5;

%k=ke (PEC) if(k=ke+1)then(set field to zero)
%*************************************************************************

%%%% End Comments Begin Program %%%%%

%Clear all of the variables in workspace and set timer (tic)
%*************************************************************************
clear('all');    tic

%Set grid point dimensions in i,j,k directions (e stand for end)
%*************************************************************************
ie =20; je = round(sqrt(3)*(ie)/2);      ke = 3*ie;      center=1;

if (mod(ie,2)~=0)            %The bounday conditions only work
   error('ie is not even')   %if ie is even
end

%Set physical parameters
%*************************************************************************
dielectric =12.96;  mu =1;
```

```
%Set air hole radius and slab thickness (lattice constant units)
%*************************************************************************
r = .26;   d = .4;

%Set the grid spacing and time step, for this program dX=dY=dZ
%*************************************************************************
dX =1/(ie);   dY=dX;      dZ=dX;    dT =1/(sqrt( dX^-2 + dY^-2 + dZ^-2 ));

% Set paramters for point guassian current source (located at is,js,ks)
%*************************************************************************
% Gaussian dipole source Jz=exp(-aguass((t-to)^2)* cos(2Pi*fo*t)

is=10; js=7; ks=1;  fo=.4;  widthfreq=.1;

aguass=(widthfreq^2)*2*pi*pi;    to=3/sqrt(aguass);

% Set the paremeters for the time step loop and set the sampling rate
%*************************************************************************
period=100;       sampling_rate=2;

N=round(period/(fo*dT)); Sample = round(1/(2*sampling_rate*dT));

sN=fix(N./Sample);  dF=1/(N*dT);    freqpoints=dF.*([1:sN]-1);

%Paramters for the PML (PMLd grid size units)
%*************************************************************************
PMLd=10;    m=3.5;    ma=1;   a_ratio=.001;

%Allocate memory for all matrices (set values to zero)
%*************************************************************************
i=[1:ie]; j=[1:je]; k=[1:ke]; t=[1:sN]; f=[1:sN];

EX(i,j,k)=0;    EY(i,j,k)=0;    EZ(i,j,k)=0;
HX(i,j,k)=0;    HY(i,j,k)=0;    HZ(i,j,k)=0;

Monitor_E_1(t,1:3)=0;  Monitor_E_2(t,1:3)=0;  Monitor_E_3(t,1:3)=0;

filter(t)=0;  Source(t)=0;

psi_EX_Z(i,j,k)=0; psi_EY_Z(i,j,k)=0; psi_HX_Z(i,j,k)=0; psi_HY_Z(i,j,k)=0;

sigEX(i,j,k)=0;     sigHX(i,j,k)=0;     sigEY(i,j,k)=0;     sigHY(i,j,k)=0;

%*************************************************************************
% Create and set the dielectric field by calling function Create_epsilon...

[eps, epsX, epsY, epsZ] = Create_epsilon3D_one_cpml(ie, je, ke, dielectric, d, r);
%*************************************************************************
% Set the values for the PML layer
```

```
[sigEZ, sigHZ, bE_Z, bH_Z, cE_Z, cH_Z, stopPML, startPML] =
Create_sigmaZ_one_cpml(ie,je,ke,dZ,dT,PMLd,m,ma,a_ratio);
%************************************************************************
% Set update coiefficents DA and DB for updating the magnetic fields

[DAHX,DAHY,DAHZ,DBHX,DBHY,DBHZ] =
Create_DA_DB_one_cpml(ie,je,ke,dT,dX,dY,dZ,mu,sigHX,sigHY,sigHZ);
%************************************************************************
% Set update coiefficents CA and CB for the electric fields

[CAEX,CAEY,CAEZ,CBEX,CBEY,CBEZ] =
Create_CA_CB_one_cpml(ie,je,ke,dT,dX,dY,dZ,epsX,epsY,epsZ,sigEX,sigEY,sigEZ);
%************************************************************************
% Implement PEC (TM symmetery) boundary at k=1 and PMC boundary at k=ke;
i=[1:ie]; j=[1:je];

%PEC boundary at k=1;                %PMC boundary at k=ke;
CAEX(i,j,1)=0; CBEX(i,j,1)=0;        DAHX(i,j,ke)=0; DBHX(i,j,ke)=0;
CAEY(i,j,1)=0; CBEY(i,j,1)=0;        DAHY(i,j,ke)=0; DBHY(i,j,ke)=0;
DAHZ(i,j,ke)=0; DBHZ(i,i,ke)=0;       CAEZ(i,j,ke)=0; CBEZ(i,i,ke)=0;

%For loop for time stepping ***********************************************
for n=1:N
%************************************************************************

%Time step the E fields*****************************************************

%update E fields in the body
i=[2:ie]; j=[2:je]; k=[2:ke];
   EX(i,j,k)=CAEX(i,j,k).*EX(i,j,k) + CBEX(i,j,k).*( HZ(i,j,k) - HZ(i,j-1,k)+ HY(i,j,k-1) - HY(i,j,k) );
   EY(i,j,k)=CAEY(i,j,k).*EY(i,j,k) + CBEY(i,j,k).*( HX(i,j,k) -  HX(i,j,k-1)+ HZ(i-1,j,k) - HZ(i,j,k) );
   EZ(i,j,k)=CAEZ(i,j,k).*EZ(i,j,k) + CBEZ(i,j,k).*( HY(i,j,k) - HY(i-1,j,k)+ HX(i,j-1,k) - HX(i,j,k) );

%update E fields on surfaces i=1, j=1, k=1;
j=[2:je]; k=[2:ke];
   % E fields at i=1 surface Perodic B.C.
   EX(1,j,k)=CAEX(1,j,k).*EX(1,j,k) + CBEX(1,j,k).*( HZ(1,j,k) - HZ(1,j-1,k) + HY(1,j,k-1) -
HY(1,j,k) );
   EY(1,j,k)=CAEY(1,j,k).*EY(1,j,k) + CBEY(1,j,k).*( HX(1,j,k) - HX(1,j,k-1) + HZ(ie,j,k)  -
HZ(1,j,k) );
   EZ(1,j,k)=CAEZ(1,j,k).*EZ(1,j,k) + CBEZ(1,j,k).*( HY(1,j,k) - HY(ie,j,k)  + HX(1,j-1,k) -
HX(1,j,k) );

i=[2:ie]; k=[2:ke]; iG=1+mod([2:ie]+(ie/2)-1,ie);
   % E fields at j=1 surface "Folded" periodic B.C. condition
   EX(i,1,k)=CAEX(i,1,k).*EX(i,1,k) + CBEX(i,1,k).*( HZ(i,1,k) - HZ(iG,je,k) + HY(i,1,k-1) -
HY(i,1,k) );
   EY(i,1,k)=CAEY(i,1,k).*EY(i,1,k) + CBEY(i,1,k).*( HX(i,1,k) - HX(i,1,k-1) + HZ(i-1,1,k) -
HZ(i,1,k) );
```

```
   EZ(i,1,k)=CAEZ(i,1,k).*EZ(i,1,k) + CBEZ(i,1,k).*( HY(i,1,k) - HY(i-1,1,k) + HX(iG,je,k) -
HX(i,1,k) );

 i=[2:ie]; j=[2:je];
   % E fields at k=1 surface PEC B.C.i=[2:ie]; j=[2:je]; k=[2:ke]
   EX(i,j,1)=CAEX(i,j,1).*EX(i,j,1) + CBEX(i,j,1).*( HZ(i,j,1) - HZ(i,j-1,1) + 0          - HY(i,j,1) );
   EY(i,j,1)=CAEY(i,j,1).*EY(i,j,1) + CBEY(i,j,1).*( HX(i,j,1) - 0          + HZ(i-1,j,1) - HZ(i,j,1) );
   EZ(i,j,1)=CAEZ(i,j,1).*EZ(i,j,1) + CBEZ(i,j,1).*( HY(i,j,1) - HY(i-1,j,1) + HX(i,j-1,1) - HX(i,j,1)
);

%update E fields on lines (i=1, j=1), (i=1, k=1), and (j=1, k=1)
k=[2:ke];  iG1=1+mod(1+(ie/2)-1,ie);
   % E fields at the i=1 and j=1 ("Folded" perodic)line
   EX(1,1,k)=CAEX(1,1,k).*EX(1,1,k) + CBEX(1,1,k).*( HZ(1,1,k) - HZ(iG1,je,k) + HY(1,1,k-1)
- HY(1,1,k) );
   EY(1,1,k)=CAEY(1,1,k).*EY(1,1,k) + CBEY(1,1,k).*( HX(1,1,k) - HX(1,1,k-1)  + HZ(ie,1,k)
- HZ(1,1,k) );
   EZ(1,1,k)=CAEZ(1,1,k).*EZ(1,1,k) + CBEZ(1,1,k).*( HY(1,1,k) - HY(ie,1,k)   + HX(iG1,je,k) -
HX(1,1,k) );

j=[2:je];
   %E Fields at the i=1 (Perodic) and k=1 (PEC) line
   EX(1,j,1)=CAEX(1,j,1).*EX(1,j,1) + CBEX(1,j,1).*( HZ(1,j,1) - HZ(1,j-1,1) + 0          -
HY(1,j,1) );
   EY(1,j,1)=CAEY(1,j,1).*EY(1,j,1) + CBEY(1,j,1).*( HX(1,j,1) - 0          + HZ(ie,j,1)  -
HZ(1,j,1) );
   EZ(1,j,1)=CAEZ(1,j,1).*EZ(1,j,1) + CBEZ(1,j,1).*( HY(1,j,1) - HY(ie,j,1)  + HX(1,j-1,1) -
HX(1,j,1) );

i=[2:ie];
  % E fields at the j=1 ("Folded" perodic) and (k=1 PEC) line
   EX(i,1,1)=CAEX(i,1,1).*EX(i,1,1) + CBEX(i,1,1).*( HZ(i,1,1) -HZ(iG,je,1)  + 0          -
HY(i,1,1) );
   EY(i,1,1)=CAEY(i,1,1).*EY(i,1,1) + CBEY(i,1,1).*( HX(i,1,1) - 0          + HZ(i-1,1,1) -
HZ(i,1,1) );
   EZ(i,1,1)=CAEZ(i,1,1).*EZ(i,1,1) + CBEZ(i,1,1).*( HY(i,1,1) - HY(i-1,1,1) + HX(iG,je,1) -
HX(i,1,1) );

%Update E field at the point (1,1,1)
   iG1=1+mod(1+(ie/2)-1,ie);
   % Field at the i=1 (Perodic), j=1 ("Folded" Perodic), k=1 (PEC) point
   EX(1,1,1)=CAEX(1,1,1).*EX(1,1,1)+CBEX(1,1,1).*( HZ(1,1,1) - HZ(iG1,je,1) + 0          -
HY(1,1,1) );
   EY(1,1,1)=CAEY(1,1,1).*EY(1,1,1)+CBEY(1,1,1).*( HX(1,1,1) - 0          + HZ(ie,1,1)   -
HZ(1,1,1) );
   EZ(1,1,1)=CAEZ(1,1,1).*EZ(1,1,1)+CBEZ(1,1,1).*( HY(1,1,1) - HY(ie,1,1)   + HX(iG1,je,1) -
HX(1,1,1) );

%End FDTD time step of E fields*******************************************

%Add psi sources to the E fields in the CPML region**********************
```

```
i=[1:ie]; j=[1:je]; k=[startPML:stopPML];

psi_EX_Z(i,j,k) = bE_Z(i,j,k).*psi_EX_Z(i,j,k) + cE_Z(i,j,k).*(HY(i,j,k)-HY(i,j,k-1))./dZ;
psi_EY_Z(i,j,k) = bE_Z(i,j,k).*psi_EY_Z(i,j,k) + cE_Z(i,j,k).*(HX(i,j,k)-HX(i,j,k-1))./dZ;

EX(i,j,k)= EX(i,j,k) - CBEX(i,j,k).*dX.*psi_EX_Z(i,j,k);
EY(i,j,k)= EY(i,j,k) + CBEY(i,j,k).*dX.*psi_EY_Z(i,j,k);
%*************************************************************************

%Add current source Jz to EZ at is,js,ks*I*******************************

EZ(is,js,ks)=EZ(is,js,ks) + 1*CBEZ(is,js,ks).*exp(-aguass.*((n.*dT)-to).^2) .*
cos(2.*pi.*fo.*(n.*dT)-to);

%*************************************************************************

%Time step H fields*********************************************************

i=[1:ie-1]; j=[1:je-1]; k=[1:ke-1];
   % H fields in the body
   HX(i,j,k)=DAHX(i,j,k).*HX(i,j,k) + DBHX(i,j,k).*( EZ(i,j,k) - EZ(i,j+1,k) + EY(i,j,k+1) - EY(i,j,k)
);
   HY(i,j,k)=DAHY(i,j,k).*HY(i,j,k) + DBHY(i,j,k).*( EX(i,j,k) - EX(i,j,k+1) + EZ(i+1,j,k) - EZ(i,j,k)
);
   HZ(i,j,k)=DAHZ(i,j,k).*HZ(i,j,k) + DBHZ(i,j,k).*( EY(i,j,k) - EY(i+1,j,k) + EX(i,j+1,k) - EX(i,j,k)
);

% update H fields on surfaces i=ie, j=je, and k=ke;

j=[1:je-1]; k=[1:ke-1];
   %H fields at i=ie Perodic B.C.
   HX(ie,j,k)=DAHX(ie,j,k).*HX(ie,j,k) + DBHX(ie,j,k).*( EZ(ie,j,k)  - EZ(ie,j+1,k)  + EY(ie,j,k+1)
- EY(ie,j,k)   );
   HY(ie,j,k)=DAHY(ie,j,k).*HY(ie,j,k) + DBHY(ie,j,k).*( EX(ie,j,k)  - EX(ie,j,k+1)  + EZ(1,j,k)
- EZ(ie,j,k)   );
   HZ(ie,j,k)=DAHZ(ie,j,k).*HZ(ie,j,k) + DBHZ(ie,j,k).*( EY(ie,j,k)  - EY(1,j,k)     + EX(ie,j+1,k)
- EX(ie,j,k)   );

i=[1:ie-1]; k=[1:ke-1]; iG=1+mod([1:ie-1]+(ie/2)-1,ie);
   % H fields at j=je "Folded" Perodic B.C.
   HX(i,je,k)=DAHX(i,je,k).*HX(i,je,k)+DBHX(i,je,k).*( EZ(i,je,k)  - EZ(iG,1,k)    + EY(i,je,k+1)  -
EY(i,je,k) );
   HY(i,je,k)=DAHY(i,je,k).*HY(i,je,k)+DBHY(i,je,k).*( EX(i,je,k)  - EX(i,je,k+1)  + EZ(i+1,je,k)  -
EZ(i,je,k) );
   HZ(i,je,k)=DAHZ(i,je,k).*HZ(i,je,k)+DBHZ(i,je,k).*( EY(i,je,k)  - EY(i+1,je,k)  + EX(iG,1,k)    -
EX(i,je,k) );

i=[1:ie-1];, j=[1:je-1];
   % H field at k=ke surface PEC B.C.
   HX(i,j,ke)=DAHX(i,j,ke).*HX(i,j,ke) + DBHX(i,j,ke).*( EZ(i,j,ke)    - EZ(i,j+1,ke) + 0           -
EY(i,j,ke) );
```

```
   HY(i,j,ke)=DAHY(i,j,ke).*HY(i,j,ke) + DBHY(i,j,ke).*( EX(i,j,ke)    - 0            + EZ(i+1,j,ke) -
EZ(i,j,ke) );
   HZ(i,j,ke)=DAHZ(i,j,ke).*HZ(i,j,ke) + DBHZ(i,j,ke).*( EY(i,j,ke)    - EY(i+1,j,ke) + EX(i,j+1,ke)
- EX(i,j,ke) );

% update H fields on (i=1,j=1), (i=1,k=1), and (j=1,k=1) lines

j=[1:je-1];
   % H fields at the i=ie(Perodic) and k=ke (PEC) line
   HX(ie,j,ke)=DAHX(ie,j,ke).*HX(ie,j,ke)+DBHX(ie,j,ke).*( EZ(ie,j,ke) - EZ(ie,j+1,ke) + 0
- EY(ie,j,ke) );
   HY(ie,j,ke)=DAHY(ie,j,ke).*HY(ie,j,ke)+DBHY(ie,j,ke).*( EX(ie,j,ke) - 0            + EZ(1,j,ke)
- EZ(ie,j,ke) );
   HZ(ie,j,ke)=DAHZ(ie,j,ke).*HZ(ie,j,ke)+DBHZ(ie,j,ke).*( EY(ie,j,ke) - EY(1,j,ke)    +
EX(ie,j+1,ke) - EX(ie,j,ke) );

i=[1:ie-1]; k=[1:ke-1]; iG1=1+mod(ie+(ie/2)-1,ie);
   % H fields at j=je ("Folded" Perodic)
   HX(ie,je,k)=DAHX(ie,je,k).*HX(ie,je,k)+DBHX(ie,je,k).*( EZ(ie,je,k)  - EZ(iG1,1,k)   +
EY(ie,je,k+1) - EY(ie,je,k) );
   HY(ie,je,k)=DAHY(ie,je,k).*HY(ie,je,k)+DBHY(ie,je,k).*( EX(ie,je,k)  - EX(ie,je,k+1) +
EZ(1,je,k)    - EZ(ie,je,k) );
   HZ(ie,je,k)=DAHZ(ie,je,k).*HZ(ie,je,k)+DBHZ(ie,je,k).*( EY(ie,je,k)  - EY(1,je,k)    +
EX(iG1,1,k)   - EX(ie,je,k) );

i=[1:ie-1];
   % H fields at the j=je ("Folded" Perodic) and k=ke (PEC)
   HX(i,je,ke)=DAHX(i,je,ke).*HX(i,je,ke)+DBHX(i,je,ke).*( EZ(i,je,ke)  - EZ(iG,1,ke)    + 0
- EY(i,je,ke) );
   HY(i,je,ke)=DAHY(i,je,ke).*HY(i,je,ke)+DBHY(i,je,ke).*( EX(i,je,ke)  - 0             +
EZ(i+1,je,ke) - EZ(i,je,ke) );
   HZ(i,je,ke)=DAHZ(i,je,ke).*HZ(i,je,ke)+DBHZ(i,je,ke).*( EY(i,je,ke)  - EY(i+1,je,ke)  +
EX(iG,1,ke)   - EX(i,je,ke) );

 % update H field at the (1,1,1) point
iG1=1+mod(ie+(ie/2)-1,ie);
   % H field at the point i=ie (Perodic), j=je ("Folded" Perodic), k=ke (PEC),
   HX(ie,je,ke)=DAHX(ie,je,ke).*HX(ie,je,ke)+DBHX(ie,je,ke).*(EZ(ie,je,ke) - EZ(iG1,1,ke) + 0
- EY(ie,je,ke) );
   HY(ie,je,ke)=DAHY(ie,je,ke).*HY(ie,je,ke)+DBHY(ie,je,ke).*(EX(ie,je,ke) - 0            +
EZ(1,je,ke)  - EZ(ie,je,ke) );
   HZ(ie,je,ke)=DAHZ(ie,je,ke).*HZ(ie,je,ke)+DBHZ(ie,je,ke).*(EY(ie,je,ke) - EY(1,je,ke)  +
EX(iG1,1,ke) - EX(ie,je,ke) );

%End FDTD Time step for H fields****************************************

%Add psi sources to the H fields in the CPML region**********************
i=[1:ie]; j=[1:je]; k=[startPML:stopPML];

psi_HX_Z(i,j,k) = bH_Z(i,j,k).*psi_HX_Z(i,j,k) + cH_Z(i,j,k).*(EY(i,j,k+1)-EY(i,j,k))./dZ;
psi_HY_Z(i,j,k) = bH_Z(i,j,k).*psi_HY_Z(i,j,k) + cH_Z(i,j,k).*(EX(i,j,k+1)-EX(i,j,k))./dZ;
```

```
HX(i,j,k)= HX(i,j,k) + DBHX(i,j,k).*dX.*psi_HX_Z(i,j,k);
HY(i,j,k)= HY(i,j,k) - DBHY(i,j,k).*dX.*psi_HY_Z(i,j,k);
%************************************************************************

%Record fields if the time step N is divisible by the integer Sample
%************************************************************************
if mod(n,Sample)==0

 t=n/Sample;

 filter(t) = (1  - exp(-(n*dT/(2*to)).^8 ));

 TestE(t,3)  = EZ(13,9,1).*filter(t);
 TestE2(t,3) = EZ(5,7,1).*filter(t);
 TestE3(t,3) = EZ(10,7,1).*filter(t);

 Source(t)=exp(-aguass.*((n.*dT)-to).^2) .* cos(2.*pi.*fo.*((n.*dT)-to)) ;

 filtersource(t)=Source(t).*filter(t);

end
%************************************************************************

% End of Time steping for loop*********************************************
end
%************************************************************************
toc %end timer (tic)

%Plot the spectra
plot(freqpoints, abs(fft(TestE)));
```

## Subfunction Create_CA_CB_one_cpml

```
function [CAEX,CAEY,CAEZ,CBEX,CBEY,CBEZ] =
Create_CA_CB_one_cpml(ie,je,ke,dT,dX, dY, dZ, epsX,epsY,epsZ,sigEX,sigEY,sigEZ)

i=[1:ie]; j=[1:je]; k=[1:ke];

      CAEX(i,j,k)=( 1-sigEX(i,j,k).*dT./2./epsX(i,j,k) )./( 1+sigEX(i,j,k).*dT./2./epsX(i,j,k) );
      CAEY(i,j,k)=( 1-sigEY(i,j,k).*dT./2./epsY(i,j,k) )./( 1+sigEY(i,j,k).*dT./2./epsY(i,j,k) );
      CAEZ(i,j,k)=( 1-sigEZ(i,j,k).*dT./2./epsZ(i,j,k) )./( 1+sigEZ(i,j,k).*dT./2./epsZ(i,j,k) );

      CBEX(i,j,k)=( dT./dX./epsX(i,j,k) )./( 1+sigEX(i,j,k).*dT./2./epsX(i,j,k) );
      CBEY(i,j,k)=( dT./dY./epsY(i,j,k) )./( 1+sigEY(i,j,k).*dT./2./epsY(i,j,k) );
      CBEZ(i,j,k)=( dT./dZ./epsZ(i,j,k) )./( 1+sigEZ(i,j,k).*dT./2./epsZ(i,j,k) );
```

### Subfunction Create_DA_DB_one_cpml

```
function [DAHX,DAHY,DAHZ,DBHX,DBHY,DBHZ] =
Create_DA_DB_one_cpml(ie,je,ke,dT,dX,dY,dZ,mu,sigHX,sigHY,sigHZ)

i=[1:ie]; j=[1:je]; k=[1:ke];

      DAHX(i,j,k)=( 1-sigHX(i,j,k).*dT/2/mu )./( 1+sigHX(i,j,k).*dT./2./mu );
      DAHY(i,j,k)=( 1-sigHY(i,j,k).*dT/2/mu )./( 1+sigHY(i,j,k).*dT./2./mu );
      DAHZ(i,j,k)=( 1-sigHZ(i,j,k).*dT/2/mu )./( 1+sigHZ(i,j,k).*dT./2./mu );

      DBHX(i,j,k)=( dT/dX/mu )./( 1+sigHX(i,j,k).*dT./2./mu );
      DBHY(i,j,k)=( dT/dY/mu )./( 1+sigHY(i,j,k).*dT./2./mu );
      DBHZ(i,j,k)=( dT/dZ/mu )./( 1+sigHZ(i,j,k).*dT./2./mu );
```

### Subfunction Create_sigmaZ_one_cpml

```
function [sigEZ, sigHZ, bE_Z, bH_Z, cE_Z, cH_Z, stopPML, startPML] =
Create_sigmaZ_one_cpml(ie,je,ke,dZ,dT,PMLd,m,ma,a_ratio)

% sigmaxE  (max value of the electric conductivity)
% sigmaxH=sigmaxE (the maximum value of the magnetic conductivity)
% PMLd     (thickness of PML layer)
% INR      (desired value for the reflectivity (nat log) of the PML layer)
% stopPML  index at which the PML stops
% startPML index at wich the PML begins
%m order of graded PML
%order of graded pole offset

%*******************************
stopPML = ke-1;
startPML = stopPML-PMLd+1;
INR=-1.6*PMLd;
sigmax = -(m+1)*INR/2/(PMLd*dZ);
amax =a_ratio*sigmax;

%*******************************
i=[1:ie]; j=[1:je]; k=[1:ke];

sigEZ(i,j,k)=0; sigHZ(i,j,k)=0;

bE_Z(i,j,k)=0;   cE_Z(i,j,k)=0;
bH_Z(i,j,k)=0;   cH_Z(i,j,k)=0;

AH_Z(i,j,k)=0;   AE_Z(i,j,k)=0;
 %*******************************
f
or i=[1:ie]
   for j=[1:je]
```

```
 k=[startPML:stopPML];

      sigEZ(i,j,k) = sigmax.*(((k-startPML)/(PMLd-1)).^m);
      sigHZ(i,j,k) = sigmax.*(((k-startPML+.5)/(PMLd-1)).^m);

      AE_Z(i,j,k) = amax.*(((stopPML-k+.5)/(PMLd-1)).^ma);
      AH_Z(i,j,k) = amax.*(((stopPML-k-.5+.5)/(PMLd-1)).^ma);
   end
end
for i=[1:ie]
   for j=[1:je]
      k=[startPML:stopPML];

      bE_Z(i,j,k) = exp( -( sigEZ(i,j,k)+AE_Z(i,j,k) ) .*dT );
      bH_Z(i,j,k) = exp( -( sigHZ(i,j,k)+AH_Z(i,j,k) ) .*dT );
   end
end

for i=[1:ie]
   for j=[1:je]
      k=[startPML:stopPML];

      cE_Z(i,j,k) = sigEZ(i,j,k).*(bE_Z(i,j,k)-1)./(sigEZ(i,j,k)+AE_Z(i,j,k));
      cH_Z(i,j,k) = sigHZ(i,j,k).*(bH_Z(i,j,k)-1)./(sigHZ(i,j,k)+AH_Z(i,j,k));
   end
end
```

## Subfunction Create_epsilon3D_one_cpml

```
function [epsr, epsXr, epsYr, epsZr]  = Create_epsilon3D_one_cpml(ie,je,ke,dielectric,d,r )

%*************************************************************************
% % Set the value of the eps for the dielectric slab region
% % the dielectric slab consists region consists of 3 air holes
% % the air holes are centered at (ic_1,jc_1),(ic_2,jc_2),(ic_3,jc_3)

ic_1 = .5      ;      jc_1 = (je+.5) ;
ic_2 = (ie+1)/2 ;      jc_2 = .5     ;
ic_3 = ie+.5    ;      jc_3 = je+.5  ;

radius=r*ie;          %radius of hole units of grid points
thickness=d*ie;       %thickness of slab units of grid points

top_slab= 1+ thickness/2;   % indices start at 1 not 0 for matlab

k_top=floor(top_slab);
```

```
eps = Create_eps_one_cpml(ie, je, ke, k_top, dielectric, radius, ic_1, jc_1, ic_2, jc_2, ic_3,
jc_3);

epsX = Create_eps_X_one_cpml(ie,je,ke, radius, eps, ic_1, jc_1, ic_2, jc_2, ic_3, jc_3);
epsY = Create_eps_Y_one_cpml(ie,je,ke, radius, eps, ic_1, jc_1, ic_2, jc_2, ic_3, jc_3);

epsShift = Create_eps_Z_one_cpml(ie, je, ke, top_slab, radius, eps, ic_1+.5, jc_1+.5,
ic_2+.5, jc_2+.5, ic_3+.5, jc_3+.5);

epsShiftX = Create_eps_X_one_cpml(ie,je,ke, radius, epsShift, ic_1, jc_1, ic_2, jc_2, ic_3,
jc_3);
epsShiftY = Create_eps_Y_one_cpml(ie,je,ke, radius, epsShift, ic_1, jc_1, ic_2, jc_2, ic_3,
jc_3);

epsZ = (epsShiftX + epsShiftY)./2;

if  (  imag(max(max(max(eps))))  ~=0   )
   error('eps has imaginary component')
end

if  (  imag(max(max(max(epsX))))~=0   )
   error('epsX has imaginary component')
end

if  (  imag(max(max(max(epsY))))~=0   )
   error('epsY has imaginary component')
end

if  (  imag(max(max(max(epsZ))))~=0   )
   error('epsZ has imaginary component')
end
epsr=eps;
epsXr=epsX;
epsYr=epsY;
epsZr=epsZ;
%*************************************************************************
```

## Subfunction Create_eps_one_cpml

```
function [eps] = Create_eps_one_cpml(ie, je, ke, k_top, dielectric, radius, ic_1, jc_1, ic_2,
jc_2, ic_3, jc_3);

i=[1:ie]; j=[1:je]; k=[1:ke];

eps(i,j,k)=1;

for k= [ 1 :  k_top  ]
    for i=[1:ie]
```

```
        for j=[1:je]
        if    ( (i-ic_1)^2+ (j-jc_1)^2 ) <= (radius^2)
           eps(i,j,k)=1;
        elseif( (i-ic_2)^2  + (j-jc_2)^2 ) <= (radius^2)
           eps(i,j,k)=1;
        elseif( (i-ic_3)^2 + (j-jc_3)^2 ) <= (radius^2)
           eps(i,j,k)=1;
        else
           eps(i,j,k)  = dielectric;
        end
      end
   end
end
```

## Subfunction Create_eps_X_one_cpml

```
function [epsX] = Create_eps_X_one_cpml(ie, je, ke, radius, eps, ic_1, jc_1, ic_2, jc_2, ic_3,
jc_3)

i=[1:ie]; j=[1:je]; k=[1:ke];

epsX(i,j,k)=eps(i,j,k);

% Set epsX*****************************************************************
for j=[1:je]
   for k=[1:ke]
      for i=[1:ie-1]
         if eps(i,j,k)==eps(i+1,j,k)
            epsX(i,j,k)=eps(i,j,k);
         else

            ipos = ic_2 + sqrt( radius^2 - (j-jc_2)^2  );
            ineg = ic_2 - sqrt( radius^2 - (j-jc_2)^2  );

               if(  ((i<=ineg)&&(ineg<=i+1))&&((i<=ipos)&&(ipos<=i+1))&&
(imag(ipos)==0&&imag(ipos)==0)     )
                    epsX(i,j,k)=  (ineg-i)*eps(i,j,k) + (ipos-ineg)*1 + (1+i-ipos)*eps(i+1,j,k);
               elseif ((i<=ineg)&&(ineg<=i+1))&&(imag(ineg)==0)
                  epsX(i,j,k) = ( (ineg-i)*eps(i,j,k) + (1+i-ineg)*eps(i+1,j,k) );
               elseif ((i<=ipos)&&(ipos<=i+1))&&(imag(ipos)==0)
                  epsX(i,j,k) = ( (ipos-i)*eps(i,j,k) + (1+i-ipos)*eps(i+1,j,k) );
               end

            ipos = ic_1 + sqrt( radius^2 - (j-jc_1)^2  );

               if (   (i<=ipos)&&(ipos<=i+1) && (imag(ipos)==0)    )
                  epsX(i,j,k) = ( (ipos-i)*eps(i,j,k) + (1+i-ipos)*eps(i+1,j,k) );
               end
```

```
            ineg = ic_3 - sqrt( radius^2 - (j-jc_3)^2  );

               if (   (i<=ineg)&&(ineg<=i+1) && (imag(ipos)==0)     )
                  epsX(i,j,k) = ( (ineg-i)*eps(i,j,k) + (1+i-ineg)*eps(i+1,j,k) );
               end
         end
      end
   end
end

% % Set i=ie remember perodic boundary condition
for j=[1:je]
   for k=[1:ke]
      if eps(ie,j,k)==eps(1,j,k)
            epsX(ie,j,k)=eps(ie,j,k);
         else

            ipos = ic_2 + sqrt( radius^2 - (j-jc_2)^2  );

               if ((ie<=ipos)&&(ipos<=ie+1) && (imag(ipos)==0) )
                  epsX(ie,j,k) = ( (ipos-ie)*eps(ie,j,k) + (1+ie-ipos)*eps(1,j,k) );
               end

             ineg = ic_3 - sqrt( radius^2 - (j-jc_3)^2  );

               if ((ie<=ineg)&&(ineg<=ie+1) && (imag(ineg)==0) )
                  epsX(ie,j,k) = ( (ineg-ie)*eps(ie,j,k) + (1+ie-ineg)*eps(1,j,k) );
               end
         end
   end
end
%  end setting of epsX ***************************************************
```

### Subfunction Create_eps_Y_one_cpml

```
function [epsY] = Create_eps_Y_one_cpml(ie, je, ke, radius, eps, ic_1, jc_1, ic_2, jc_2, ic_3,
jc_3)

i=[1:ie]; j=[1:je]; k=[1:ke];

epsY(i,j,k)=eps(i,j,k);

% set epsY  ***************************************************************
for i=[1:ie]
   for j=[1:je-1]
      for k=[1:ke]
         if eps(i,j,k)==eps(i,j+1,k)
            epsY(i,j,k)=eps(i,j,k);
```

```
            else
              jpos =  jc_2 + sqrt( radius^2 - (i-ic_2)^2  );

                if (  ((j<=jpos)&&(jpos<=j+1))  && (imag(jpos)==0)  )
                    epsY(i,j,k) = ( (jpos-j)*eps(i,j,k) + (1+j-jpos)*eps(i,j+1,k) );

                end

              jneg = jc_1 - sqrt( radius^2 - (i-ic_1)^2  );

                 if (  ((j<=jneg)&&(jneg<=j+1)) && (imag(jneg)==0)   )
                    epsY(i,j,k) = ( (jneg-j)*eps(i,j,k) + (1+j-jneg)*eps(i,j+1,k) );
                 end

              jneg = jc_3 - sqrt( radius^2 - (i-ic_3)^2  );

                 if (    ((j<=jneg)&&(jneg<=j+1)) && (imag(jneg)==0)      )
                    epsY(i,j,k) = ( (jneg-j)*eps(i,j,k) + (1+j-jneg)*eps(i,j+1,k) );
                 end
            end
          end
    end
end

% % Set j=je remember perodic boundary condition
for i=[1:ie]
    for k=[1:ke]
    iG=1+mod(i+(ie/2)-1,ie);
         if eps(i,je,k)==eps(iG,1,k)
              epsY(i,je,k)=eps(i,je,k);
         else
              jpos = jc_3 + sqrt( radius^2 - (i-ic_3)^2  );

              if(  (je<=jpos)   && (imag(jpos)==0)   )
                epsY(i,je,k) = .5*eps(i,je,k) + .5*eps(iG,1,k);
              end

              jpos = jc_1 + sqrt( radius^2 - (i-ic_1)^2  );

              if(  (je<=jpos)&&  (imag(jpos)==0) )
                epsY(i,je,k) = .5*eps(i,je,k) + .5*eps(iG,1,k);
              end
          end
    end
end
% % End setting epsY ******************************************************
```

## References

[1] Han. H. et al. Terahertz pulse propagation in a plastic photonic crystal fiber. *Appl. Phys. Lett.* **80**, 2634 (2002).

[2] Palik, Edward D. *Handbook of Optical Constants of Solids II*, Academic Press, Inc. Harcourt Brace Jovanovich, Publishers, (1991).

[3] Ghandi, Sorab K. *VLSI Fabrication Principles*., John Wiley & Sons, Inc. Second Edition, (1994).

[4] Jianming D. et al. Terahertz time-domain spectroscopy characterization of the far-infrared absorption and index of refraction of high-resistivity, float-zone silicon. *J. Opt. Soc. Am. B* **21,** 1379 (2004).

[5] Grischwksy, D. et al. Far-infrared spectroscopy with terahertz beams in dielectrics and semiconductors. *J. Opt. Soc. Am. B*. **7**, 2006 (1990).

[6] Stolen R.H. Far-infrared Absorption in high resistivity GaAs. *Appl. Phys. Lett.* **15**, 74 (1969).

[7] Stolen R.H. Temperature Dependence of far-infrared absorption in GaAs. *Phys. Rev. B* **11,** 767 (1975).

[8] Vuckovic J. et al. Optimization of the Q factor in photonic crystal microcavities. *IEEE J. of Quantum Electronics*, **38**, 850 (2002). Akahane Y. et al. High-Q photonic nanocavity in a two-dimensional photonic crstyal. *Nature* **425,** 944 (2003).

[9] Virginia Semiconductor, 1501 Powhatan Street,Fredericksburg, VA 22401

[10] Joannopoulos John, Meade Robert, and Winn Joshau, *Photonic Crystals - Molding the Flow of Light*, Princeton University Press, (1995).

[11] Coldren, Larry A. Corzine, Scott W. Diode lasers and photonic integrated circuits. John Wiley & Sons, Inc. (1995).

[12] Johnson S. G. et al. Block-iterative frequency-domain methods for Maxwell's equations in a planewave basis. *Optics Express* **8**, 173 (2001).

[13] http://ab-initio.mit.edu/wiki/index.php/MIT_Photonic_Bands

[14] Wu Q. et al. Ultrafast electro-optic field sensors. *App. Phys. Lett*. **68**, 1604 (1996). Nahata A. et al. Coherent detection of freely propagating terahertz radiation by electro-optic sampling. *App. Phys. Lett.* **68**, 150 (1996).

[15] Yariv, Amnon Optical *Electronics in Modern Communications*, Oxford University Press, 1997.

[16] Gallot G. et al. Measurement of THz absorption and dispersion of ZnTe and the relevance to electro-optic detection of THz radiation. *Appl. Phys. Lett.* **74**, 3450 (1999).

[17] Zhang X.C. et al. Resoance nonlinear susepptiblity near the bandgap of GaAs. *Phys. Rev. Lett.* **69**, 2303 (1992).

[18] Hu B.B et al. Terahertz radiation induced by subband-gap fremtosecond optical excitation of GaAs. *Phys. Rev. Lett*. **67**, 2709 (1991).

[19] Gallot G. et al. Measurement of THz absorption and dispersion of ZnTe and the relevance to electro-optic detection of THz radiation. *Appl. Phys. Lett.* **74**, 3450 (1999).

[20] Kersting, R. et al. Few-Cycle THz Emission from Cold Plasma Oscillations. *Phys. Rev. Lett.* **79**, 3038 (1997). Kersting, R. et al. Coherent plasmons in n-doped GaAs *Phys. Rev. B* **58**, 4553 (1998).

[21] Palik Edward D. *Handbook of Optical Constants of Solids*, Academic Press, Harcourt Brace Jovanovich Publishers, 1985.

[22] Li M. et al. Measurement and anaylsis of terahertz radiation from bulk semiconductors. *Appl. Phys. Lett.* **67**, 25 (1995).

[23] Johnston, M.B. et al. Simulation of terahertz generation at semiconductor surfaces. *Phys. Rev. B.* **65**, 165301 (2002).

[24] Palik Edward D. Handbook of Optical Constants of Solids, Academic Press, Harcourt Brace Jovanovich Publishers, 1985.

[25] Jepsen, P.U. et al. Generation and detection of terahertz pulses from biased semiconductor antennas. *J. Opt. Soc. Am. B*. **12**, 2424 (1996).

[26] Zhao G. et al. Design and Performance of a THz emission setup based on semi insulating GaAs. *Rev. Sci. Instr.* **73**, 1715 (2002).

[27] Dreyhaupt A. et al. High Intensity terahertz radiation from a microstructured large area photoconductor. *Appl. Phys. Lett.* **86**, 121114 (2005).

[28] Kohler R. et al. Terahertz semiconductor heterostructure laser. *Nature* **417**, 156 (2002).

[29] Cole B.E. et al. Coherent manipulation of semiconductor quantum bits with terahertz radiation. *Nature* **410**, 60 (2001).

[30] Allen D.G. et al. Optically detected measurement of the ground-state population of an ensemble of neutral donors in GaAs. *Phys. Rev. B* **72**, 035302 (2005).

[31] Cirac J. I. et al. Quantum computation with cold trapped ions. *Phys. Rev. Lett.* **74**, 4091 (1995).

[32] Yoshie Y. et al. Vacuum Rabi splitting with a single quantum dot in a photonic crystal nanocavity. *Nature* **432**, 200 (2004).

[33] Sherwin, M. S. et al. Quantum computation with quantum dots and terahertz cavity quantum electrodynamics. *Phys Rev. A*. **60**, 3508 (1999).

[34] Kohler et al. Terahertz Semiconductor heterostructure laser. *Nature* **417**, 156 (2002).

[35] Williams B.S. et al. Terahertz quantum-cascade laser operating up to 137K. *App. Phys. Lett.* **83**, 5142 (2003).

[36] Kohler et al. Terahertz Semiconductor heterostructure laser. *Nature* **417**, 156 (2002).

[37] Loncar M. et al. Low-threshold photonic crystal laser. *Appl. Phys. Lett.* **81**, 2680 (2002).

[38] Gerard J.M. et al. Strong purcell effect for InAs quantum boxes in three-dimensional solid state microcavities. *J. Lightwave Tech.* **17**, 2089 (1999).

[39] Dowling J.P., et al. The photonic band edge laser: A new approach to gain enhancement. *J. Appl. Phys.* **75**, 1896 (1994).

[40] Meier et al. Laser action from two-dimensional distributed feedback in photonic crystals. *Appl. Phys. Lett.* **74**, 7 (1999).

[41] Coldren and Corzine Diode Lasers and Photonic Integrated Circuits John Wiley & Sons, 1995.

[42] Agarwal et al. Review back-side via hole etching process for grounding GaAs based monolithic microwave integrated circuits. *J. Electrochemical Soc.* **152**, G567 (2005).

[43] Nordheden N.J. et al. Reactive ion etching of via holes for GaAs high electron mobility transistors and monolithic microwave integrated circuits using Cl2/BCl3/Ar gas mixtures. *J. Vac. Sci Technol.l* **B11**, 1879 (1993).

[44] Fujita M. et al. Simultaneous inhibition and redistribution of spontaneous light emission in photonic crystals. *Science* **308**, 1296 (2005).

[45] Khurgin B. et al. Optical rectification and terahertz emission in semiconductors. *J. Opt. Soc. Am. B* **11**, 2492 (1994).

[46] Boroditsky, M. Light extraction from optically pumped light emitting diode by thin-slab photonic crystals. *Appl. Phys. Lett*. **75**, 1036 (1999).

[47] Imada M. et al. Multidirectional distributed feedback photonic crystal laser. *Phys. Rev. B* **65**, 195306 (2002).

[48] http://ab-initio.mit.edu/wiki/index.php/MIT_Photonic_Bands

[49] Vuckovic J. et al. Optimization of the Q factor in photonic crystal microcavities. *IEEE J. Quant. Elect*. **38**, 850 (2002).

[50] Ozbay E. Layer by layer photonic crystals from microwave to far-infrared frequencies. *J. Opt. Soc. Am. B* **13**, 1945 (1996).

[51] Noda S. Full three-dimensional photonic bandgap crystals at near infrared wavelengths. *Science* **289**, 604 (2000).

[52] Johnson, Steven D. et al. Three dimensionally periodic dielectric layer structure with omindirectional photonic bandgap. *Appl. Phys. Lett*. **77**, 3490 (2000).

[53] Minghao Q. et al. A three-dimensional optical photonic crystal with designed point defects. *Nature* **429**, 538 (2004).

[54] Povinelli, M. L. et. al. Emulation of two-dimensional photonic crystal defect modes in a photonic crystal with a three dimensional photonic band gap. Phys. Rev. B. **64**, 075313 (2001).

[55] Taflove A., and Hagness S. *Computational electrodynamics The Finite-Difference Time-Domain Method 3rd edition,* Artech House, 2005.

[56] Yee, K.S. Numerical solution of initial boundary value problems involving Maxwell's equations in isotropic media. *IEEE Trans. Antennas Progagat.* **14**, 302 (1966).